RESISTANCE FLUCTUATION SPECTROSCOPY AND OTHER TRANSPORT BEHAVIOR IN LANTHANUM BARIUM COPPER OXIDE

BY

ADAM COLE WEIS

DISSERTATION

Submitted in partial fulfillment of the requirements
for the degree of Doctor of Philosophy in Physics
in the Graduate College of the
University of Illinois at Urbana-Champaign, 2017

Urbana, Illinois

Doctoral Committee:

Assistant Professor Gregory MacDougall, Chair
Professor Dale J. Van Harlingen, Director of Research
Professor Philip W. Phillips
Assistant Professor Virginia O. Lorenz

Abstract

In phase diagrams of cuprate high-temperature superconductors, superconductivity often occurs close to other phases of strongly correlated electron matter. In $La_{2-x}Ba_xCuO_4$ (LBCO), the critical temperature for superconductivity is anomalously suppressed at $x = 1/8$, and at the same doping, a "striped" ordering of spin and charge emerges. Although the charge striped phase is expected to include local resistance anisotropy, this has not been observed, and LBCO's stripe behavior has only been studied by scattering experiments at beamline facilities.

In this work, pulsed-laser deposition and microfabrication were used to create small-volume LBCO wires at dopings near $x = 1/8$. In such wires, low-frequency resistance-fluctuation spectra were measured at various dopings, temperatures, and bias currents. Material characterization studies by x-ray diffraction, atomic force microscopy, magnetometry, and resistance measurements were used to determine an optimized laser deposition recipe for superconducting LBCO films.

The observed low-frequency resistance fluctuations in LBCO wires had behavior consistent with an ordered charge-stripe state in small, fluctuating domains. In most samples, the power spectral density of resistance noise increases as temperature is lowered below the charge-ordering temperatures expected for LBCO. The power spectral density of resistance fluctuations is found to scale with inverse frequency, consistent with the "$1/f$" noise that the Dutta-Horn model predicts for an ensemble of two-level systems. Additional observations — suppressed power spectral density at high currents and variation of noise with in-plane current direction — suggest that the resistance fluctuations have a

stripe-like character.

In summary, a process has been developed for consistent superconducting thin-film LBCO, and in these films, low-frequency resistance fluctuation spectroscopy has been demonstrated as a tool to study stripe-like charge ordering.

Acknowledgments

Graduate school is hard, as is research in general. No sequence of words on a page can express the extent to which I relied on others to complete this research, this dissertation, and this degree. I truthfully could not have done this on my own. I make a paltry attempt to give credit and thanks below, but on some level, I also need to thank humanity in general for allowing me to mess around in a lab for 8.5 years until a PhD thesis emerged. Thank you, humans.

First and foremost, I'm now and forever grateful to my family. My parents, Sherri and Burt, as well as "Nana" and my sister, Ashley, have all been incredibly supportive on my journey from a nerdy kid who wanted to be a scientist, to a nerdy kid who *is* a scientist. Thanks for listening on all of the phone calls and impromptu rants about physics and lab work. Thanks to Me-Ma, Pa, Uncle Mike, Steve, Melanie, Dustin, Dylan, and the rest of the extended family for being fun, loving, and proud.

I'm also extremely blessed to have made so many friends through the Illinois physics graduate program. While graduate school met my expectations as an academic experience, it *far* exceeded my expectations as a social experience, and I feel lucky to have met so many awesome people. I cherish the shared laughs, misery, and beer more than you know.

My thesis advisor, Dale Van Harlingen, was a rock in an often chaotic research environment and made the entirety of this work possible. Thanks Dale, for introducing me to superconductors and showing me how they work (or sometimes don't work). The other members of the Van Harlingen group were an incredible resource and shaped me

as a scientist as much as my advisor. In particular, I'm indebted to Vladimir Orlyanchik and Martin Stehno for sharing their expertise in noise, electronics, and low-temperature research, and for generally being role models as wizards of experimental physics. Dan Bahr, Joel Strand, Micah Stoutimore, David Caplan, Cihan Kurter, and Aaron Finck were all useful voices of experience when I needed it. Thanks to Juan Atkinson, Chris Nugroho, Chris English, Erik Huemiller, David Hamilton, Kenneth Schlax, and Can Zhang for sharing ideas, equipment, and lunch over the time I was in grad school; you guys were the best coworkers I could have asked for. The newest members of Dale's group, Lu Tan and Gilbert Arias, have already made an impression, and I have no doubt they'll live up to the Van Harlingen pedigree.

The highlight of my graduate research was probably the opportunity to mentor a long list of undergraduate students: Michael Witek, Mark Murawski, Ashley Hicks, Yizhou Xin, Ethel Perez, Marek Mroczek, So-Ra Chung, Justin Lane, Azton Wells, Mounir Fizari, Melissa Bosch, and Kevin Ryan. The development of a pulsed-laser deposition recipe for $La_{2-x}Ba_xCuO_4$, and the extensive film characterization studies presented in this dissertation would not have been possible without their hard work and ingenuity. I learned a lot, about myself and about life, working with all of you.

The steric-entrapment process, used to synthesize the high-quality laser-deposition sources in this work, was inspired by and developed in close collaboration with the research group of Waltraud Kriven in the materials science department of the University of Illinois. In particular, Dr. Pathikumar Sellappan was a dedicated and organized collaborator and I greatly benefited from working with him. Without his careful efforts, the high-quality samples used in this research would've remained inaccessible.

This research was funded by the Department of Energy Office of Basic Energy Sciences, first through grant DE-FG02-07ER46453 (The Quantum Materials at the Nanoscale cluster at Illinois), then later through DOE-BES grant DE-SC0012368. The research presented herein, especially the thin film characterization and microfabrication work, was

carried out in part in the Frederick Seitz Materials Research Laboratory Central Research Facilities, University of Illinois. Training and technical discussion with Mauro Sardela, Scott MacLaren, and Shivakumar Bhaskaran was especially useful. Thanks to Tony Banks for providing a sense of order to the PPMS/VSM lab, and for coaching me through a huge miscellany of vacuum science and fabrication questions.

Thanks to the coaches and athletes at Illini Crossfit for helping me push around weights when I needed to deal with the stress of finishing a PhD. Finally thank you to my thesis committee, Profs. Gregory MacDougall, Philip W. Phillips, and Virginia O. Lorenz for investing your time in my defense and dissertation.

Table of Contents

Chapter 1

Properties and Phase Diagrams of Cuprate Superconductors

1.1 Basic properties of superconductors

The full theoretical description of why superconductivity occurs in some materials is beyond the scope of this writing. However, some of the fundamentals of superconductivity will be reviewed for the sake of completeness and to aid later discussion of LBCO. Superconductivity is observed in some solid materials below a critical temperature T_c, and is best summarized as the combination of three observed behaviors:

1. Zero DC electrical resistance. A superconductor below T_c can transmit a sufficiently small electrical current without loss. It is worth emphasizing that the resistance is literally zero, not just arbitrarily small. Some measurements of persistent currents in superconducting solenoids find a characteristic decay time greater than 10^5 years [1].

2. Perfect diamagnetism. In what is known as the Meissner effect, a superconductor will expel a small externally applied magnetic field, such that the internal field is zero [2]. Equivalently, a superconductor has a negative magnetic susceptibility $\chi_V = -1$, causing its diamagnetic internal field to exactly cancel any external field. This effect is distinct from perfect conductivity. In a perfect conductor, Lenz's law causes the time derivative of the magnetic B-field to vanish, $dB/dt = 0$. Whereas the Meissner effect in a superconductor imposes the stronger condition $B = 0$. Note that even the strongest non-superconducting diamagnets have $-10^{-4} < \chi_V < 0$,

the diamagnetic response of superconductors is orders of magnitude stronger.

3. Vanishing density of states near the Fermi level. Also known as an energy gap. This was first directly observed via tunneling and infrared spectroscopies [3, 4]. The existence of a gap is also responsible for a superconductor's exponential decay of specific heat with temperature below T_c [5].

The superconducting state is observed to exist below a critical temperature T_c, below a critical magnetic field H_c, and with less than a critical current density J_c flowing through the superconducting sample, as illustrated in a general phase diagram in Fig. 1.1. These parameters are material-dependent and coupled, e.g. the critical temperature $T_c(H, J)$ will decrease (eventually to zero) if magnetic field or current is applied to a superconducting sample. As will be discussed in the next few sections, superconductivity is an emergent quantum phenomenon. It is emergent because its properties arise from the many-body interactions of particles, without being obvious consequences of the microscopic details of this interaction.

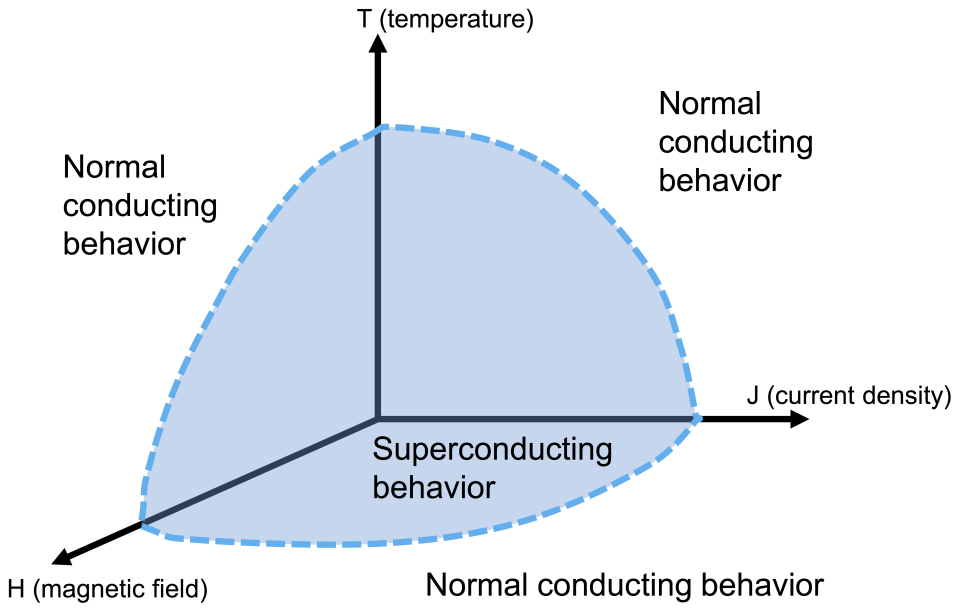

Figure 1.1: **General Superconducting Phase Diagram.**

1.2 BCS theory

The vanishing resistance of a superconductor was initially observed in 1911 by Kamerlingh Onnes in mercury cooled below 4.2 K [6], but the theoretical understanding of superconductivity was not completed until much later, when Bardeen, Cooper, and Schrieffer successfully described and solved an interacting-electron Hamiltonian that reproduced superconducting behavior [7]. In this BCS theory, two electrons bind together, in a state known as a Cooper pair, through a phonon-mediated interaction. A mobile electron distorts the nearby positively charged lattice ions, creating a trailing wake of positive charge to which the second electron is attracted.

As fermions, individual electrons are subject to the Pauli exclusion principle: they must be antisymmetric under exchange and cannot occupy the same quantum state. However, the wave function Ψ of an ensemble of $N/2$ pairs of electrons may be written as a product of identical states ϕ,

$$\Psi(\mathbf{r}_1 s_1, ..., \mathbf{r}_N s_N) = \phi(\mathbf{r}_1 s_1, \mathbf{r}_2 s_2)...\phi(\mathbf{r}_{N-1} s_{N-1}, \mathbf{r}_N s_N), \tag{1.1}$$

where $\mathbf{r}_i$ is electron position and s_i is spin. This wave function does not satisfy the Pauli principle, but can be antisymmetrized by adding positive or negative terms in which the positions and spins have different permutations. As an example, the wave function

$$\begin{aligned}\Psi(\mathbf{r}_1 s_1, ..., \mathbf{r}_N s_N) =& \phi(\mathbf{r}_1 s_1, \mathbf{r}_2 s_2)\phi(\mathbf{r}_3 s_3, \mathbf{r}_4 s_4)...\phi(\mathbf{r}_{N-1} s_{N-1}, \mathbf{r}_N s_N) \\ &- \phi(\mathbf{r}_3 s_3, \mathbf{r}_2 s_2)\phi(\mathbf{r}_1 s_1, \mathbf{r}_4 s_4)...\phi(\mathbf{r}_{N-1} s_{N-1}, \mathbf{r}_N s_N),\end{aligned} \tag{1.2}$$

is antisymmetric under exchange of the 1st and 3rd electron. A sufficient number of terms can antisymmetrize the entire N-electron state, while maintaining each pair in an identical two-electron wave function ϕ. The full solution of BCS theory demonstrates that the ground state of a superconductor is such a state composed of pairs of indistinguishable

electrons with equal and opposite momentum. Because the state of each pair is closely related to all other pairs through the exclusion principle, it is impossible to break one pair without disrupting all others. Therefore, the first excited state above the BCS ground state of coherent pairs is considerably different than the ground state and there is an energy gap, Δ, between the superconducting ground state and any excited states.

Note that the above description takes care to avoid describing Cooper pairs as bosons that condense into a shared ground state. It is convenient and intuitive to think of Cooper pairs as composite bosons, because they have several boson-like properties. Like bosons, Cooper pairs have integer spin (0 or 1), can share a wave function (for pairs, this is the two-particle wave function ϕ), and occupy low-energy states at low temperature. However, the identification of pairs as bosons is inaccurate for a couple of reasons. Firstly, the mean distance between electrons in a pair is typically much larger than the mean pair-to-pair separation, so it is misleading to think of pairs as point-like particles occupying the same spatial coordinate. Secondly, Cooper pairs have short lifetimes, with pairs of electrons continuously moving in and out of energetically favorable, paired states. As a result, Cooper pairs do not obey Bose-Einstein statistics. Equivalently, the pair operators constructed by BCS theory do not obey the bosonic commutation relations.

The energy gap, Δ, explains the observed vanishing density of states in some spectroscopic measurements on superconductors. However, it also explains the vanishing resistance of a superconductor. In normal metals, the primary source of electrical resistance is the scattering of electrons from thermal lattice vibrations, i.e. phonons with energies $k_B T$, where k_B is the Boltzmann constant. In a superconductor at low temperatures, $k_B T << \Delta$ and these thermal phonons are not energetic enough to scatter a Cooper pair to an excited state. The superconductor goes normal when the thermal energy, times a small numeric factor predicted by BCS, is equal to the gap, such that $\Delta = 1.76\, k_B T_c$. The size of the gap is mostly set by the strength of the attractive pairing interaction, which BCS requires to be much less than the Fermi energy. The typically weak pairing potential correlates with

a small gap ($<$ few meV) and low T_c ($<$ 10 K), for most of the standard superconductors described by BCS.

1.3 Ginzburg-Landau theory

Although fairly comprehensive, BCS theory is probably best used to explain the ground state of a superconductor, i.e. the homogeneous superconducting state far away from the boundary of a superconducting sample. In situations where superconductivity is weak or spatially varying, the phenomenological theory of Ginzburg and Landau is a more straightforward limiting case of BCS. In the Meissner state, the superconductivity varies spatially across the boundary between the superconductor and the finite magnetic field outside, so we will use GL theory to explain the perfect diamagnetism of a superconductor.

Ginzburg-Landau theory introduces a complex psuedo-wave-function ψ, known as superconducting *order parameter*. Its magnitude represents the spatially varying density of superconducting electrons, $|\psi|^2 = n_S(\mathbf{r})$ and is proportional to the energy gap. Its phase is intended to account for the macroscopic quantum behavior of the superconducting state. In the discussion of BCS theory (equation 1.1) the ground state was described as a product of identical two-electron wave functions ϕ. In most situations, the phase of this wave function ϕ may be thought of as roughly equivalent to the phase of the order parameter ψ, although they are not strictly equal.

If ψ is small, then the free energy density f governing a superconductor can be written as a power series [8],

$$f = f_{n0} + \alpha|\psi|^2 + \frac{\beta}{2}|\psi|^4 + \frac{1}{2m^*}\left|\left(\frac{\hbar}{i}\nabla - \frac{e^*}{c}\mathbf{A}\right)\psi\right|^2 + \frac{h^2}{8\pi}, \tag{1.3}$$

where f_{n0} is the normal state free energy, α and β are temperature-dependent coefficients,

$h = H/H_c$ is the reduced magnetic field, and $\hbar$ is the reduced Planck constant. For a typical Cooper pair, the effective mass m^* is twice the electron mass, and the effective charge, $e^* < 0$, is twice the electron charge $-e$. The term in parentheses is the canonical momentum operator with vector potential $\mathbf{A}$. In the homogeneous zero-field case, this becomes a standard description of a second-order phase transition, with a trivial solution of $|\psi|^2 = 0$ when $\alpha \geq 0$ and a non-trivial (superconducting) solution of $|\psi|^2 = -\alpha/\beta$ when $\alpha < 0$. If we maintain zero field, but now allow ψ to vary spatially across a single spatial dimension x, the energy minimization condition becomes

$$\frac{\hbar^2}{2m^*|\alpha|}\frac{d^2\widetilde{\psi}}{dx^2} + \widetilde{\psi} - \widetilde{\psi}^3 = 0, \tag{1.4}$$

where $\widetilde{\psi} = \psi/\sqrt{-\alpha/\beta}$. This clearly suggests a characteristic length scale for variations in the order parameter

$$\xi(T) = \sqrt{\frac{\hbar^2}{2m^*|\alpha(T)|}}, \tag{1.5}$$

which is known as the superconducting coherence length. Through careful comparison with BCS theory, this coherence length can also be shown to represent the expected spatial separation between the two electrons in a Cooper pair.

In finite field, we can consider order parameter solutions $\psi(\mathbf{r}) = |\psi(\mathbf{r})|e^{i\varphi(\mathbf{r})}$. Minimization of the GL free energy then leads to the differential equation for current

$$\mathbf{J} = \frac{c}{4\pi}\nabla \times \mathbf{h} = \frac{e^*}{m^*}|\psi|^2\left(\hbar\nabla\varphi - \frac{e^*}{c}\mathbf{A}\right). \tag{1.6}$$

This equation is gauge invariant. For convenience, we may choose the *London gauge* convention, which sets $\mathbf{J} \propto \mathbf{A}$, such that $\nabla\varphi = 0$. Then we may consider taking the curl of both sides of equation 1.6. On the left, Ampère's Law gives $\mathbf{J} = (c/4\pi)\nabla \times \mathbf{B} - \epsilon_0\partial\mathbf{E}/\partial\mathbf{t}$,

with $\partial\mathbf{E}/\partial\mathbf{t} = \mathbf{0}$ for a steady state solution. On the right use $\mathbf{B} = \nabla \times \mathbf{A}$. Then,

$$\frac{c}{4\pi}\nabla \times \nabla \times \mathbf{B} = -\frac{e^{*2}}{cm^*}|\psi|^2\mathbf{B} \implies \mathbf{B} - \lambda^2\left(\nabla^2\mathbf{B}\right) = 0, \tag{1.7}$$

$$\text{where } \lambda^2 = \frac{m^*c^2}{4\pi|\psi|^2e^{*2}}. \tag{1.8}$$

Now the Meissner state may be imagined as a field $\mathbf{B} = B_0\hat{z}$ in the region $x < 0$ with a superconductor in the region $x > 0$. Within the superconductor the solution to the differential equation 1.7 will be

$$\mathbf{B}(x) = B_0e^{-x/\lambda} \cdot \hat{z}, \tag{1.9}$$

which means the magnetic field is rapidly attenuated in the superconducting region. Deep in the interior of the superconducting samples, the field will be negligible as is characteristic of the Meissner effect. Note, that the field does not vanish instantly, however; it decays over a length scale λ which will diverge as $T \to T_c$ and $|\psi|^2 \to 0$. This material-dependent length λ is known as the *penetration depth* of a superconductor.

1.4 Type I and type II superconductors

The energetic considerations of Ginzburg-Landau theory also implies the existence of a critical magnetic field for superconductivity. The energetic cost of expelling magnetic field from the Meissner state is $H^2/8\pi$ per unit volume. If the energy of the superconducting state is not at least much lower than the energy of the normal metal state, then the material will cease to superconduct and magnetic field will begin to penetrate. The critical field of a superconductor is the field H_c at which

$$\frac{H_c(T)^2}{8\pi} = f_{\text{normal}}(T) - f_{\text{superconducting}}. \tag{1.10}$$

Field will penetrate a superconductor in one of two ways. This becomes apparent by considering a "domain wall" between a superconducting and a normal region within a material exposed to the critical field H_c. Depending on the ratio $\kappa = \lambda/\xi$ of the penetration depth to the coherence length, the domain wall will have one of the two appearances shown in Fig. 1.2. When $\kappa \ll 1$ there is a region of length $\xi - \lambda$ containing additional positive energy density $H_c^2/8\pi$ associated with the field. When $\kappa \gg 1$ there is a region of length $\lambda - \xi$ containing additional negative energy density $f_{\text{normal}}(T) - f_{\text{superconducting}}$ associated with condensation to the superconducting state. In summary, the energy associated with the superconductor-normal domain wall will be roughly proportional to $(\xi - \lambda)$. If this energy is positive ($\kappa \ll 1$), then as field penetrates the superconductor, the system will minimize the surface area of the boundary between superconductor and normal metal. In such *type I* superconductors, any field penetrating the sample will do so in large regions near the boundary of the sample. If the domain-wall energy is negative ($\kappa \gg 1$), as in a *type II* superconductor, the system will maximize the surface area between superconductor and normal metal, creating a small-scale texture of field penetration.

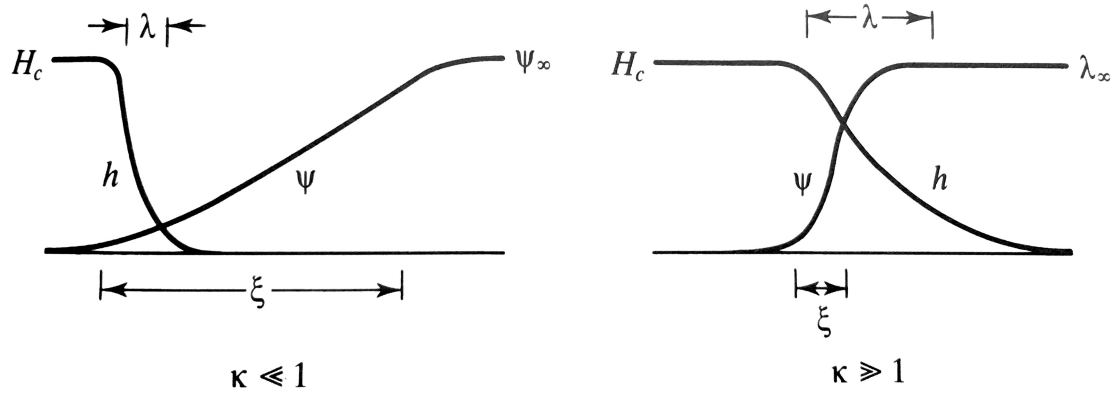

Figure 1.2: As the normal region ends and the superconducting region begins (moving rightwards in each diagram) the field decays over a length λ and the order parameter ψ turns on over a length ξ. From [9], p. 121.

In a type II superconductor, field enters the material in quantized amounts of flux through non-superconducting pinholes known as *vortices*. The quantization condition is

imposed by the fact that, around the perimeter of a vortex, the order parameter will have a winding phase due to the magnetic field and this phase must wind by a multiple of 2π to be single-valued. Note that quantization also implies a minimum amount of flux $\Phi_0 = hc/2e$ in each vortex, corresponding to a phase winding of exactly 2π. A type II superconductor will actually have two critical fields. At H_{c1}, vortices begin entering the sample, diamagnetism begins to weaken, and resistance begins to increase. At H_{c2} the vortices, which have normal cores of diameter ξ, begin to overlap and the sample is completely normal. More quantitative calculations can show that H_{c1} is typically much lower than the thermodynamic critical field of equation 1.10. Since any electrical current generates a magnetic field, the existence of a critical field in a superconductor also imposes a maximum current density J_c.

1.5 High-temperature superconductivity

Superconductors have held promise for a wide array of applications. The zero resistance state has the potential to provide lossless energy transmission. Their capacity to sustain high current densities is potentially useful for compact motors, generators, and electromagnets. Already, superconductors (typically NbTi or Nb_3Sn alloys) are used to create the powerful electromagnets required for magnetic resonance imaging. The macroscopic quantum behavior of superconductors has also made them a promising candidate for quantum computing architectures.

However, deployment of superconductors in any of these application scenarios is always complicated by the requirement of costly cryogenics to maintain the superconducting material at a temperature $T < T_c$. Therefore, there has been persistent interest in superconducting materials that perform at higher temperature, ideally room temperature and above. To data the superconductive materials with the highest transition temperatures are layered copper oxide or cuprate materials, also known as high-temperature su-

perconductors (HTSC). Cuprates were the first class of materials to have superconducting T_c's above the boiling point of liquid nitrogen at 77 K, thereby enabling superconducting electronics with lower-cost cryogenics. $YBa_2Cu_3O_{7-y}$ (YBCO) was the first known superconductor with a T_c above liquid nitrogen temperatures, with $T_c = 92$ K. The material $Hg_{0.8}Tl_{0.2}Ba_2Ca_2Cu_3O_{8+\delta}$ holds the current record for the highest ambient-pressure T_c, at 135-138 K [10]. Lanthanum barium copper oxide, the subject of the experiments presented in this thesis, has a maximum T_c of 30 K and was the first copper oxide superconductor to be discovered [11].

1.6 Comparison of cuprate and BCS superconductors

Many of the concepts used to describe the simple BCS superconductors above are also applicable to the high-T_c cuprate superconductors, although there are several key differences that will be summarized below. Copper oxide superconductors are usually described as "non-BCS" because it is believed that their pairing mechanism is not phonon-mediated, so the specific Hamiltonian proposed by BCS does not apply. For phonon-mediated superconductors, T_c is correlated to the Debye frequencies of the phonon modes responsible for the pairing interaction; in cuprates, the relationship between phonon frequencies and T_c is less clear [12, 13]. While the light oxygen atoms in the cuprates do lend themselves to high-frequency phonons, many also believe that these phonons don't sufficiently explain T_c. Experimentally speaking, phonons seem an unlikely pairing mechanism because the *isotope effect* — the observation in BCS superconductors that T_c varies with lattice ion mass — is weak or non-existent in cuprates [14]. It is believed that the pairing mechanism in cuprates is caused by electron-magnon interactions [15, 16], but a corresponding theory equivalent in detail and completeness to BCS is not yet established.

Despite the absence of phonon coupling, Cooper pairs still form in the cuprates, and the remainder of BCS applies on a somewhat qualitative level, e.g. the pairs are still

believed to share an identical quantum state. The magnitude of the energy gap in the cuprates is around 50 meV for many of the commonly studied materials, an order of magnitude higher than typical "low-T_c" gaps. The phenomenological Ginzburg-Landau theory essentially applies in full to the cuprates, and the GL coherence length ξ and penetration depth λ may be used to characterized HTSC materials, although they will be anisotropic (see [9], chapter 9 for a detailed discussion of this anisotropy). Compared to "simple" superconductors, the cuprates typically have coherence lengths that are an order of magnitude smaller, and penetration depths that are a small factor larger.

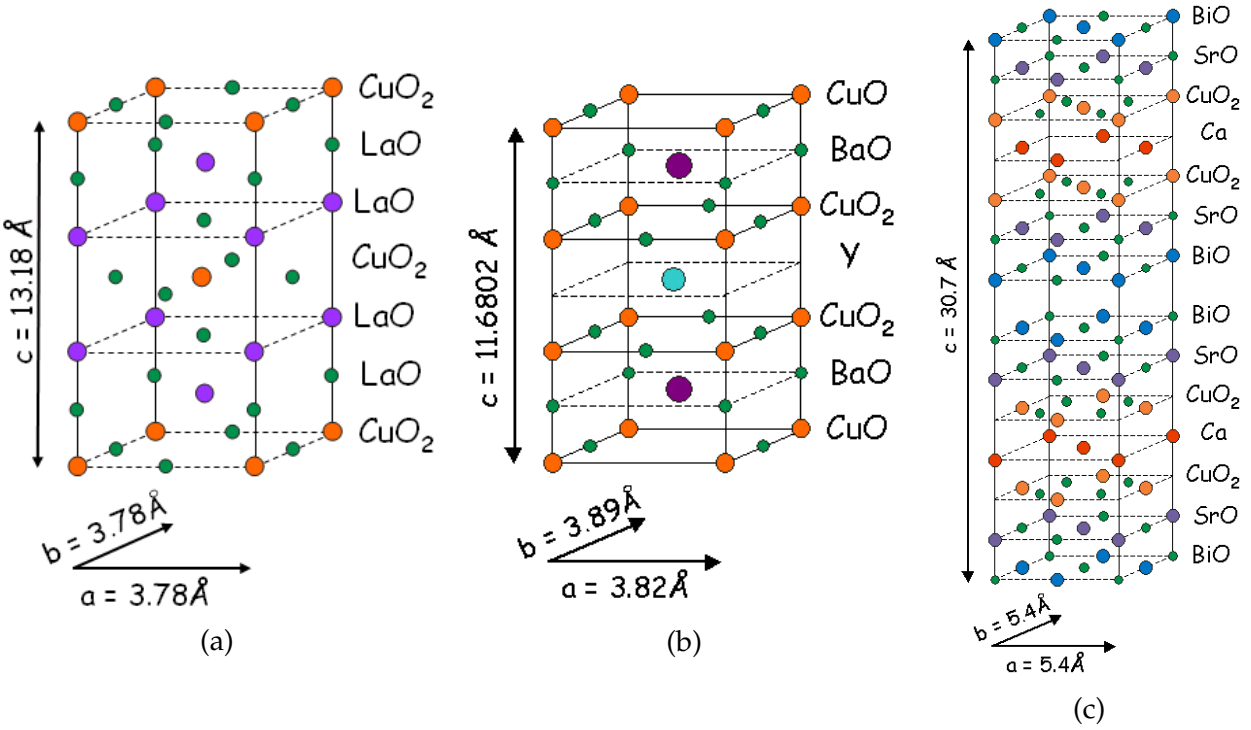

Figure 1.3: **Structures of some common cuprate superconductors** (a) $La_{2-x}Ba_xCuO_4$(subject of this dissertation) or $La_{2-x}Sr_xCuO_4$. (b) $YBa_2Cu_3O_{7-y}$. (c) $Bi_2Sr_2CaCu_2O_{8+y}$. Diagrams from [17].

The anisotropy of superconductivity in the cuprates is not surprising considering their composition and structure. Because BCS superconductors are usually single elements or binary alloys, they tend to have high-symmetry lattice structures. For example, niobium is body-centered cubic. In contrast, cuprates tend to have structures like those pic-

tured in Fig. 1.3 [17]. Superconducting cuprates are usually a specific type of oxide perovskite mineral in which metal oxide layers are stacked with an offset between adjacent layers. In the cuprates, one or more conducting copper oxygen planes are stacked between one or more other metal-oxide planes, often containing rare-earth elements. These rare-earth oxide layers are usually doped by cation substitution, oxygen vacancies, or interstitial oxygen and function as donor layers which change the charge carrier concentration within the copper oxygen planes. The stoichiometry and structure of some cuprates, such as $La_{2-x}Ba_xCuO_4$, can be classified as Ruddlesden-Popper phases of the form $A_{n-1}A'_2B_nX_{3n+1}$, in which $n = 1, 2 \ldots \infty$, A, A', and B are cations, and X is an anion [18]. A Ruddlesden-Popper structure will contain n layers of cation-centered octahedra per unit cell. Other cuprates, such as $YBa_2Cu_3O_{7-y}$, do not have the Ruddlesden-Popper stoichiometry, but still have structures consisting of full or half-octahedra and layered oxide planes. In a cuprate lattice, these octahedra are a useful way of grouping atoms and can facilitate description of certain structural transitions.

The quasi-two-dimensional superconductivity of cuprates can be thought of as being mostly confined to the copper-oxygen planes, with weak coupling between layers. The coherence length of cuprate superconductors will be greatest along the a and b lattice directions within the copper oxygen plane, and smallest along the c-axis normal to the planes. Similarly, the penetration depth λ_c, which describes the Meissner screening due to supercurrents flowing along the c-axis, is larger than λ_{ab} which describes the screening of magnetic fields perpendicular to the a-b plane. Intuitively, circulating screening currents are more easily established within the copper-oxygen planes, so field perpendicular to them will be more easily attenuated. All cuprates are "hard" type II superconductors with $\xi \ll \lambda$ and $H_{c1} \ll H_{c2}$. In YBCO, for example, $H_{c1} \sim 20$ mT while $H_{c2} \sim 22$ T for a sample with suppressed T_c [19]. Vortex dynamics are very important in the cuprates, especially in engineering applications, because of their extreme type II behavior, large separation between H_{c1} and H_{c2}, and the fact that the complex lattice structures of cuprates are more

prone to defects which aid vortex entry.

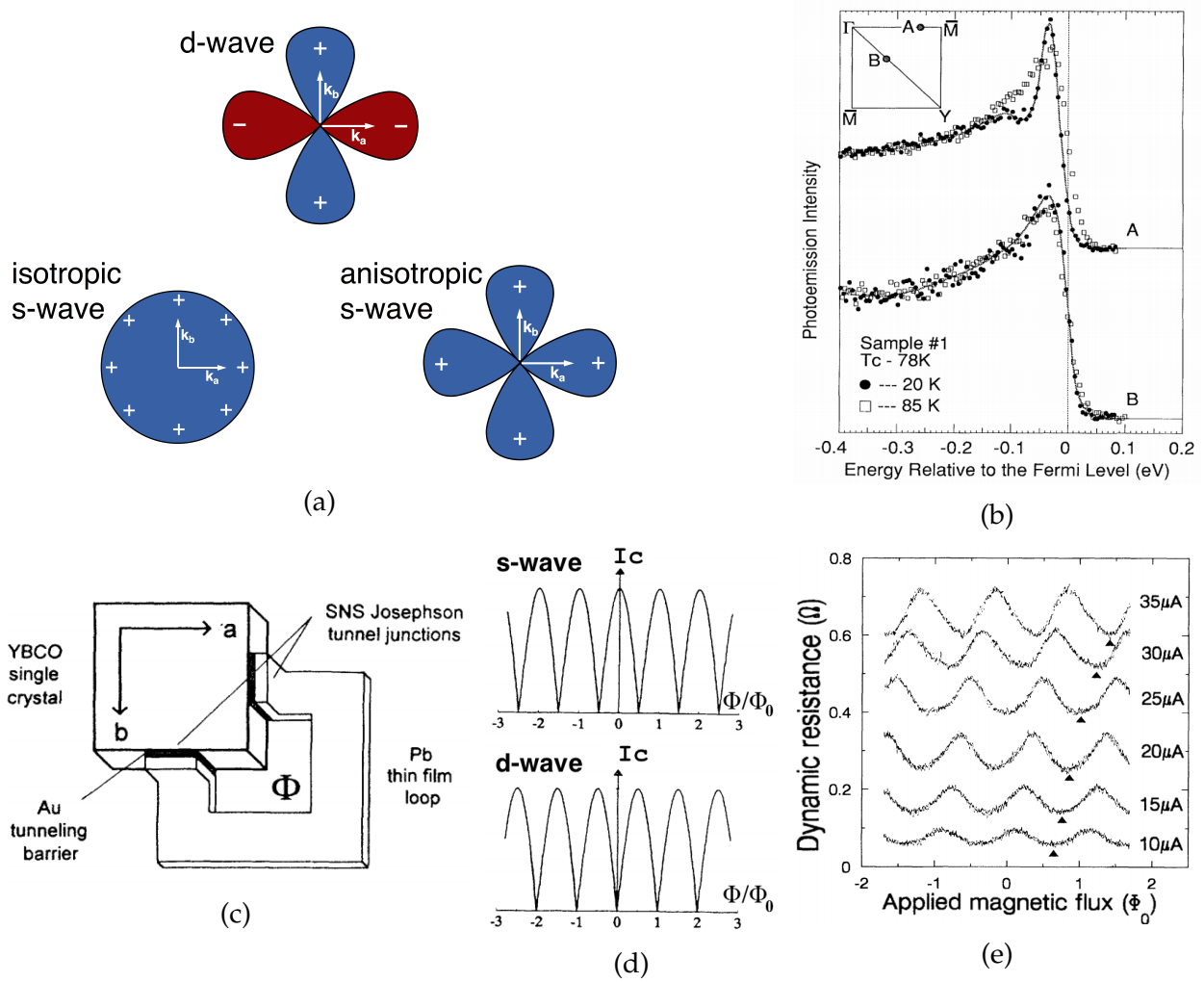

Figure 1.4: **Evidence for d-wave order parameter symmetry in the cuprates** (a) Possible symmetries of the superconducting order parameter in the k_a-k_b momentum plane. k_a and k_b indicate k-space *direction*; the radial coordinate displays gap energy. BCS superconductors are *s-wave* and cuprates are *d-wave*, as demonstrated through ARPES (gap magnitude) and SQUID experiments (phase shift). (b) ARPES line scans along the [100] direction (A) and [110] direction (B) in $Bi_2Sr_2CaCu_2O8 + y$. The [100] direction shows a significant change in the density of states below T_c =78 K, indicating the opening of a gap, while the [110] direction has no change in the density of states, suggesting a node where $|\psi|^2 = 0$ [20]. (c) Sketch of the $YBa_2Cu_3O_7 - y$ SQUID device in [21]. (d) A SQUID's critical current I_c modulates as a function of applied magnetic flux Φ, expressed relative to the flux quantum $\Phi_0 = hc/2e$. At zero flux, I_c will be a maximum for s-wave, or will vanish for d-wave. Instead of directly measuring I_c, the feedback electronics used in [21] measure dynamic resistance, which is higher when I_c is exceeded. (e) In the limit of low bias current, dynamic resistance is a maximum at $\Phi = 0$, implying that I_c is a minimum and the YBCO crystal has a d-wave symmetry.

One of the most striking features of the cuprates is that their Ginzburg-Landau superconducting order parameter has been observed to have $d_{x^2-y^2}$ symmetry, analogous to a d-orbital electronic state in an atom. As illustrated in Fig. 1.4(a), a d-wave superconductor has an order parameter whose magnitude, $|\psi(\mathbf{k})^2|$, defined over momentum space for Cooper pairs with momentum $\mathbf{k}$, has a maximum for pairs travelling in the $\pm$a or $\pm$b lattice directions, and has nodes where $|\psi|^2 = 0$ for the $\langle 110 \rangle$ directions. The order parameter is independent of k_c. For comparison, BCS superconductors have s-wave symmetry, where the order parameter is isotropic over k-space. Such a four-fold anisotropic gap was observed experimentally by angle-resolved photoemission spectroscopy (ARPES) [20], as shown in Fig. 1.4(b). The phase structure of the d-wave order parameter, which changes sign upon 90° rotation, was also confirmed experimentally by a tunneling experiment in which a DC-SQUID (superconducting quantum interference device) was fabricated with Josephson junctions on perpendicular faces of a YBCO crystal [21] as depicted in Fig. 1.4(c). Single-valuedness of the order parameter's phase enforces the condition

$$\phi_a - \phi_b + 2\pi\Phi/\Phi_0 + \delta_{ab} = 0, \tag{1.11}$$

where $\phi_{a,b}$ are the phase shifts across the junctions on the a and b face of the crystal, Φ is the applied magnetic flux, and δ_{ab} is the intrinsic phase shift as Cooper pairs scatter from the a to b direction within the cuprate. When $\Phi = 0$ and $\delta_{ab} = 0$, the supercurrent through the SQUID splits equally through the two junctions and is a maximum. In finite magnetic field, flux quantization will cause additional circulating supercurrent in order to lock to the nearest Φ_0, and in one of the two junctions this circulating current will add with the external current, effectively lowering the maximum applied external current I_c. The intrinsic phase shift δ_{ab} shifts this oscillatory critical current: $I_c \propto |\cos(\pi\Phi_{\text{ext}}/\Phi_0 + \delta_{ab})|$ (Fig. 1.4(d)). The interference-based experiment is directly equivalent to an optical 2-slit experiment with a phase shift at one of the slits. The experimentally observed SQUID

oscillations (Fig. 1.4(e)) show that, in the limit of low bias current, a maximum in differential resistance, i.e. a minimum in the critical current occurs at $\Phi = 0$, consistent with an intrinsic phase shift of $\delta_{ab} = 90^\circ$ between perpendicular lobes in the order parameter.

Unlike BCS superconductors, most cuprates are doped. In $La_{2-x}Ba_xCuO_4$, the doping x indicates the substitution of barium onto lanthanum sites in the lattice. Since Ba is one column to the right of La in the periodic table, increasing x adds holes (positive charge carriers) to the material. In $YBa_2Cu_3O_{7-y}$ the parameter y indicates doping via oxygen vacancies. As y is varied, the carrier density and disorder changes and T_c varies. For most cuprates, the undoped "parent" material is not superconducting, or even conducting. Typical undoped cuprates are antiferromagnetic insulators, with a Néel temperature close to room temperature. As doping is increased superconductivity will begin to occur with a low T_c; the T_c increases until it reaches a maximum at some optimal doping, and then further doping will lower T_c, eventually to 0 K.

1.7 Cuprate phase diagrams and the pseudogap

HTSC behavior versus doping can be summarized in a phase diagram, such as that of Fig. 1.5, with doping on a horizontal axis, temperature on the vertical axis, and shaded regions representing states of electronic matter such as the superconducting, normal metal, and antiferromagnetic insulating phases. The example in Fig. 1.5 is the phase diagram of YBCO [22], but almost every cuprate, electron- or hole-doped, has a similar diagram with different doping and temperature scales. The *pseudogap* phase shown is also universal in underdoped HTSC materials and occurs above T_c but below some temperature T^* that decreases with doping.

Some characteristics of the pseudogap resemble an extremely weak superconducting phase, but other pseudogap phenomena are distinct from superconductivity. The eponymous feature of the pseudogap is its suppressed density of states at the Fermi level, al-

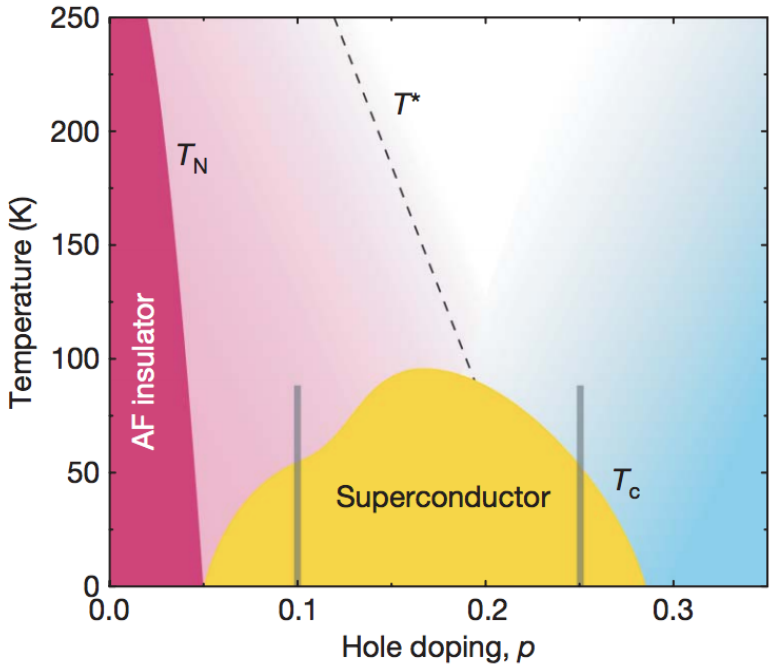

Figure 1.5: **The phase diagram of YBCO**, which may serve as a schematic phase diagram describing all high-T_c materials. Superconductivity occurs at low temperatures and moderate doping; the pseudogap occurs at low dopings and temperatures between T_c and T^*. From [22].

though the density of states does not completely vanish as in the superconducting state. The pseudogap has been confirmed experimentally by ARPES and shows the same d-wave symmetry seen in the superconducting state. The vanishing resistance and Meissner state of superconductivity do not occur in the pseudogap, because the gap is incomplete. A large number of additional experimental techniques have been applied to study the temperature and doping dependence of the pseudogap, including scanning tunneling microscopy (STM), nuclear magnetic resonance (NMR), DC resistance, optical conductivity, specific heat, Raman scattering, and neutron scattering. These diverse experiments are discussed in more detail in numerous review articles [23].

Different experiments are universally consistent with a suppressed density of states, but offer some discrepancy on the sharpness and location of the crossover or phase transition at T^*. In particular, it isn't clear whether the T^* line converges with the overdoped

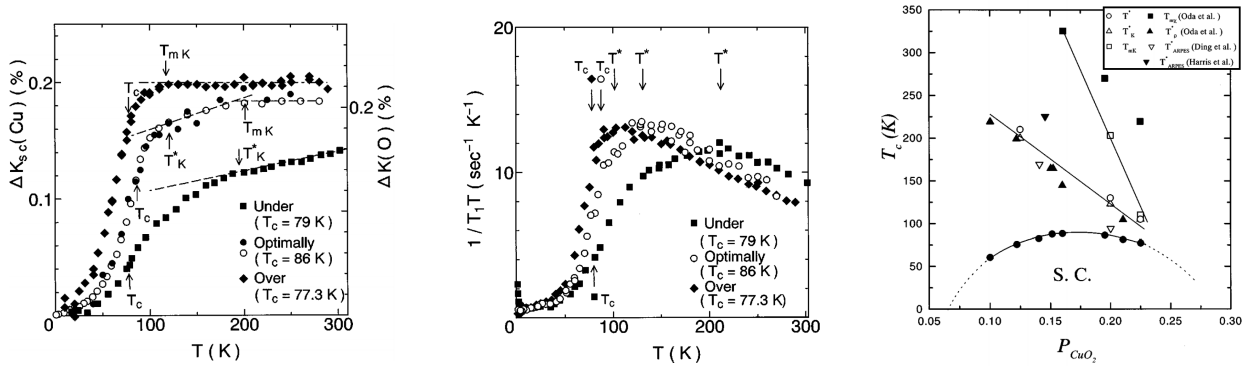

(a) (b) (c)

Figure 1.6: **Nuclear magnetic resonance (NMR) properties of the pseudogap, from [24].** (a) The Knight shift, a change in the characteristic frequencies of lattice ions due to paramagnetic coupling to electron spins, as a function of temperature for several $Bi_2Sr_2CaCu_2O_{8+\delta}$ crystals. Spin-singlet electron correlations below T_{mK} decrease spin susceptibility and creat a temperature-dependent shift. (b) Nuclear spin-lattice relaxation rate $1/T_1$, scaled by inverse temperature T, for the same samples. Temperatures T^* indicate each sample's respective maximum in $1/T_1T$, and are consistent with pseudogap onset temperatures measured by more direct density-of-states measurements. The decreasing relaxation rate below T^* is consistent with a spin gap believed to be associated with the underlying mechanism of HTSC. This spin gap varies continuously across T_c, suggesting that the spin-singlet pairing of high-temperature superconductivity may begin at T^*. (c) Phase diagram over temperature and hole doping. Based on NMR data, ARPES, and resistivity.

T_c line, or intersects with the $T = 0$ axis at optimal T_c, which might indicate a quantum critical point at the center of the superconducting dome. NMR measurements, such as those shown in Fig. 1.6, indicate that the spin-singlet pairing of superconductivity actually onsets at T^* and varies continuously through T_c [24]. These collected results are often interpreted as the existence of *pre-formed* Cooper pairs at temperatures below T^* that become more prevalent below T_c; it is believed that this high-T Cooper pairing is insufficient for superconductivity due to large fluctuations and disorder in the quantum-mechanical phase of the pair wave functions [25].

Several experiments have suggested the presence of additional types of electronic or magnetic matter in the pseudogap, in addition to pre-formed phase-incoherent Cooper pairs. The Nernst signal, a measured voltage perpendicular to both an applied magnetic

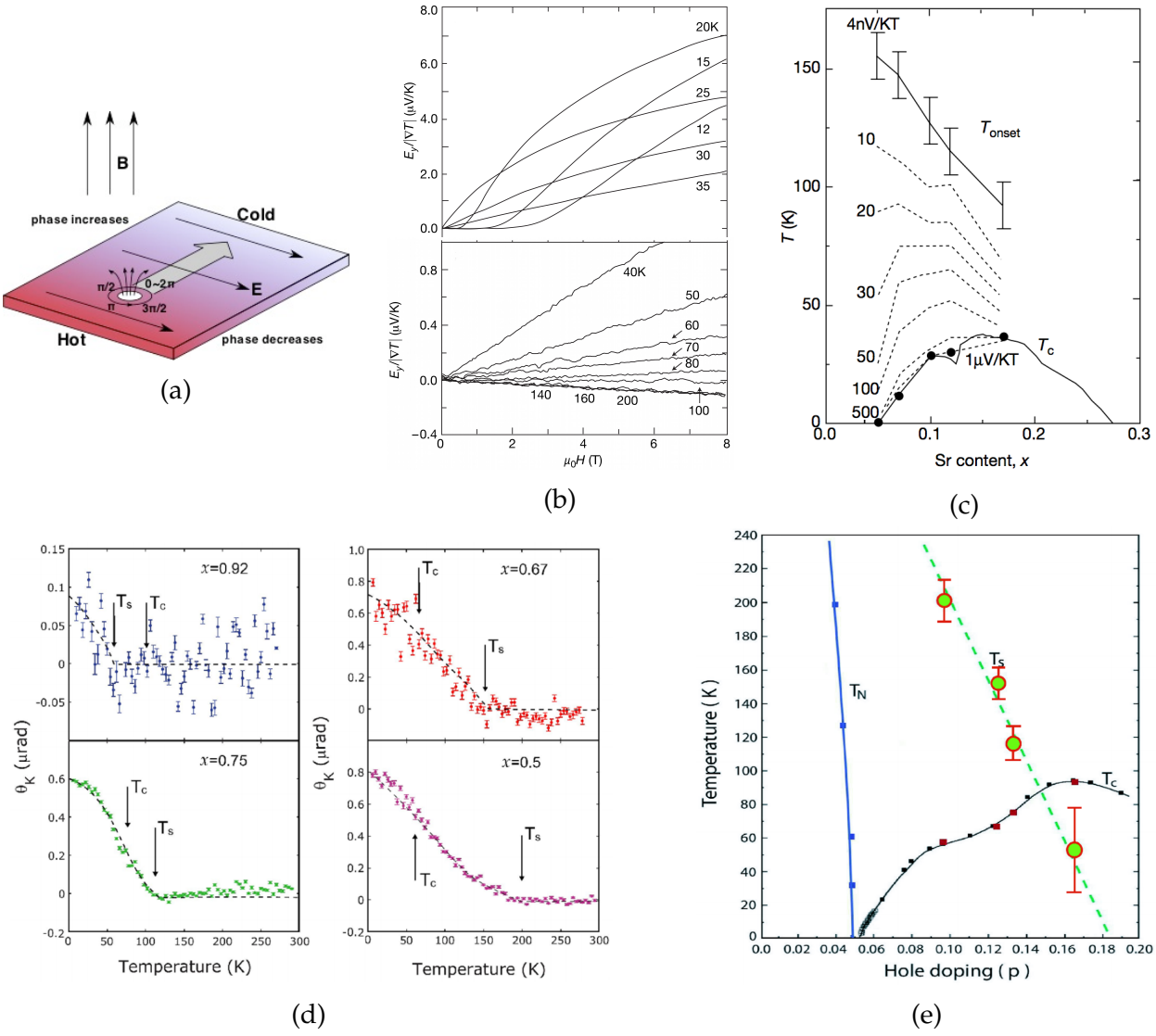

Figure 1.7: **Evidence for magnetic order in the pseudogap.** (a) Sketch of the Nernst field generated as a supercodnucting vortex moves along a thermal gradient (b) The normalized Nernst signal in $La_{1.9}Sr_{0.10}CuO_4$ persists above T_c = 28 K. (c) The phase diagram associated with anomalous Nernst behavior suggests a gradual onset of possible vortex-like matter at low doping [26]. (d) Magneto-optic Kerr rotation angle vs. temperature in $YBa_2Cu_3O_{6+x}$, for several x in zero field. Kerr signal begins at pseudogap temperature T_S and evolves continuously through T_c. [27]. (e) Phase diagram from Kerr effect.

field and temperature gradient, is high in the superconducting state due to vortex motion, as sketched in Fig. 1.7(a). However, as shown in Fig. 1.7(b) the Nernst coefficient has been observed in a variety of cuprates to vary continuously across T_c and remain finite in the absence of superconductivity, suggesting a weak type of vortex-like matter

in the pseudogap [26]. In the phase diagram (Fig. 1.7(c)), the crossover temperature for anomalous Nernst behavior seems to follow a dome-like line above T_c, rather than the T^* line typical of most other pseudogap phenomena. The magneto-optic Kerr effect, has been observed in the pseudogap with μrad-scale polar Kerr rotations in zero magnetic field, as shown in Fig. 1.7(d)-(e), suggesting the presence of magnetic order [27].

One of the most striking examples of new physics in the pseudogap is the breaking of rotational symmetry in the *electron nematic* phase. This charged phase borrows its name from the nematic phase of liquid crystals, in which long molecules have a preferred orientation but unordered positions, such that rotational symmetry is broken but translational symmetry remains; the *smectic* phase is similar but does break translational symmetry. The charged nematic phase present in the pseudogap has been most impressively observed in the wide field-of-view STM experiments of J.C. Davis [28, 29], and is pictured in Fig. 1.8. The Fourier transform of these STM images reveals two effects. Firstly, the Bragg peaks corresponding to a and b lattice directions are inequivalent — the density of states at $\mathbf{Q}_y$ is roughly 30% less than that at $\mathbf{Q}_x$ — which indicates the rotational asymetry characteristic of an electron nematic. This nematic order is long range. The domain size was estimated to be larger than the scan width. Secondly, Fourier peaks are observed at wavevectors shifted by 1/4 reciprocal lattice units, corresponding to charge modulations that are periodic every 4 unit cells within the copper oxygen planes. This smectic-like electronic order is fairly weak and short-ranged, with a correlation length that never exceeds a few nm in BSCCO. More recent resonant x-ray experiments have shown evidence for similar charge modulation in other cuprates (Fig. 1.8(c)), with a correlation length and incommensurate wavevector that vary somewhat with doping [30]. At least some of these STM and x-ray features appear most strongly in underdoped samples at low temperature, rather than following the T^* line. Both techniques observe at least some coexistence of nematic behavior with superconductivity at $T < T_c$ and low doping.

One view is that the participation of pseudogap charge carriers in these exotic elec-

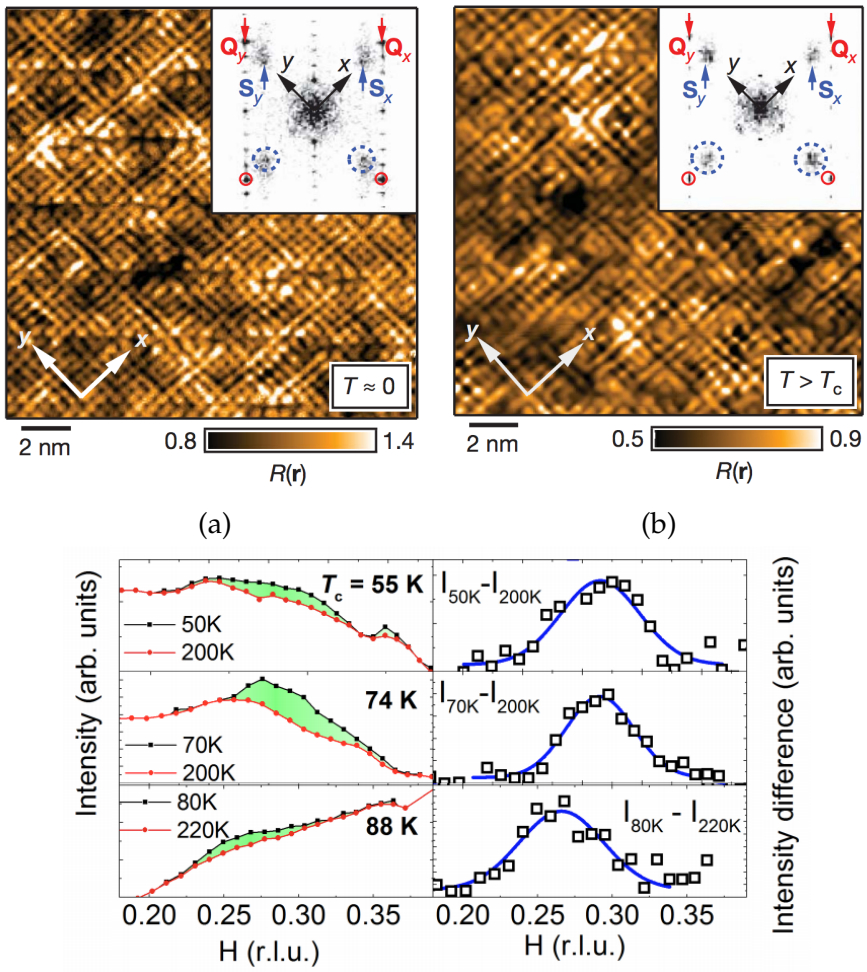

Figure 1.8: **Nematic and short-range charge order in pseudogap.** In a $Bi_2Sr_2CaCu_2O_{8+\delta}$ sample with T_c = 35 K, STM images show short-range charge order at both (a) 4.3 K, in the superconducting state and at (b) 55 K, in the pseudogap. Insets show unequal Bragg wavevectors (red arrows) associated with nematicity and superlattice peaks (blue arrows) associated with charge ordering. [28] (c) In $HgBa_2CuO_{4+\delta}$, for various dopings with the T_c's shown, x-ray peaks consistent with $4a_0$-periodic charge modulation can be extracted by subtracting a high-temperature background signal from the resonant spectra at $T \gtrsim T_c$ [30].

tronic phases excludes their participation in superconductivity, while another view is that states such as the electron nematic are natural precursors to the superconducting state that eventually occurs at lower temperatures. Whether states such as the electron nematic phase should be viewed as competitors of superconductivity remains an open question.

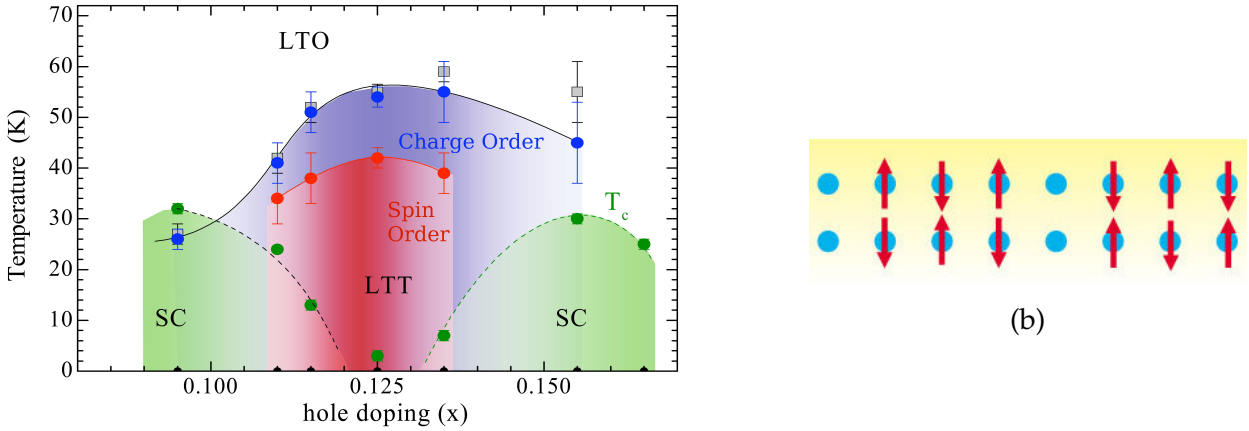

Figure 1.9: **The 1/8 anomaly and stripes in $La_{2-x}Ba_xCuO_4$** (a) Phase diagram of $La_{2-x}Ba_xCuO_4$showing anomalous suppression of T_c at $x = 1/8$ [31]. Phases include superconductivity (SC) charge- and spin-order, and low-temperature orthorhombic (LTO) and tetragonal (LTT) structural phases. The pseudogap should also be present, but isn't explicitly labelled here. (b) Depiction of simultaneous charge and spin order, looking down at a copper-oxygen plane, with blue dots indicating Cu sites. Striped charge accumulation (bare dots) occurs every four unit cells and spin order repeats every eight unit cells [32].

1.8 LBCO's unique stripe phase

As mentioned above, there is a strong desire for higher-T_c superconductors for engineering applications. The pseudogap has been an ongoing area of active research because it offers a phase qualitatively similar to superconductivity at temperatures close to, or even above, room temperature. The hope is that by understanding the almost superconducting phase of the pseudogap, and other above-T_c phases in the cuprates, researchers will better learn how to stabilize superconductivity at high temperatures in newly developed materials with strongly correlated electrons. In this sense LBCO has an even more exceptional phase diagram than most other cuprates. Rather than a single optimal superconducting T_c, LBCO has two equal optimal T_cs of 32 K at $x = 0.095$ and $x = 0.155$. As shown in Fig. 1.9(a), the intermediate *1/8 anomaly* near $x = 0.125$ is characterized by the near-complete suppression of T_c and simultaneous emergence of spin and charge orders, collectively known as the *striped* phase. As depicted in Fig. 1.9(b), at $x = 0.125$, the stripe pattern

consists of an accumulation of charge into 1D rows spaced every 4 unit cells in either the a or b lattice direction, with local antiferromagnetism between the charged rows. The antiferromagnetic regions on each side of a charge stripe have a relative sign flip, such that the magnetic structure of the stripe pattern repeats every 8 unit cells. The period of the stripe pattern also has a weak, monotonic doping dependence; for example, at $x = 0.095$, the charge-order period is slightly less than 5 unit cells.

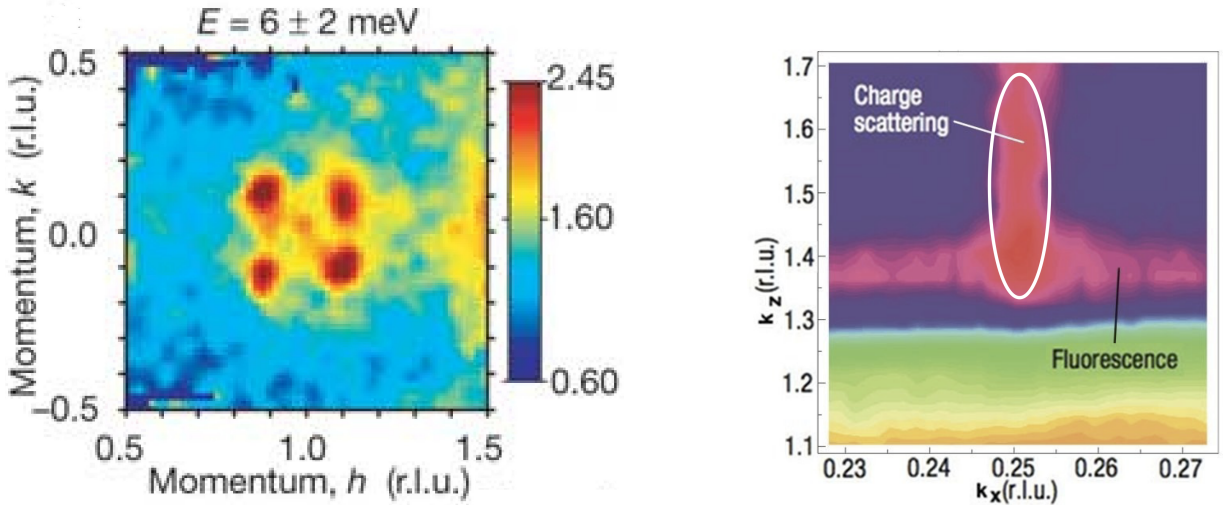

(a) (b)

Figure 1.10: **Scattering evidence for the spin- and charge-striped state** (a) Elastic neutron scattering peaks shifted from the usual antiferromagnetic peak by $1/8a_0$, suggesting 8-unit-cell spin periodicity [33]. (b) Elastic x-ray scattering peak, consistent with 4-unit-cell charge periodicity in-plane, and 2-unit cell periodicity along the c-axis [34]. Note that the peak (pink spot) is extremely elongated in the out-of-plane axis, suggesting a very low c-axis correlation length for stripe order.

The primary evidence for the existence of the stripe state comes from x-ray and neutrons scattering experiments. Neutron scattering detects both crystal structure and magnetic order, but is not directly sensitive to charge. In addition to the underlying tetragonal lattice, neutron scattering peaks (Fig. 1.10(a)) are observed at wavevectors consistent with the spin stripe order sketched in Fig. 1.9(b) [33].). As an antiferromagnet, La_2CuO_4 has a superlattice scattering peak at $\mathbf{k} = \frac{2\pi}{a}\left(\frac{1}{2}, \frac{1}{2}\right)$, which in the stripe state, splits into $\mathbf{k} = \frac{2\pi}{a}\left(\frac{1}{2} \pm \frac{1}{8}, \frac{1}{2} \pm \frac{1}{8}\right)$, suggesting spin order that is 8-unit-cell periodic, con-

sistent with Fig. 1.9(b) rotated by 90° every adjacent CuO_2 plane. Although neutrons aren't directly charge sensitive, their diffraction can be extremely sensitive to lattice distortions. In LBCO's striped state, charge order is indirectly detectable because positively charged stripes Coulomb repel the positive lattice ions, resulting in $4a_0$-periodic lattice distortion. This is observable as a shift in the usual in-plane Bragg peaks by 1/4 reciprocal lattice units.

Charge order has also been confirmed directly in $La_{2-x}Ba_xCuO_4$through soft x-ray scattering [34]. In the charge-ordered state, an additional elastic peak (Fig. 1.10(b)) is observed at $\mathbf{k} = 2\pi\left(\frac{1}{4a}, 0, \frac{3}{2c}\right)$, suggesting four-unit-cell periodicity in the ab-plane and two-unit-cell periodicity in the c-axis. X-ray peak widths suggest an in-plane stripe correlation length of $\xi_a b \approx 127a \approx 48$ nm, and an inter-plane correlation length of $\xi_c \approx 2c \approx 2.6$ nm. Similar determination of stripe domain size from neutron experiments indicates that the correlation lengths shrink as doping is changed away from $x = 1/8$ or as temperature is increased [31]. Because of the small size of stripe domains, searches for the stripe phase via electronic transport in macroscopic samples have been inconclusive [35].

1.9 Comparison of striped and pseudogap phases

At this point, the similarities between the stripe state of LBCO and the electron nematic in the cuprate pseudogap should be obvious. Both are characterized by the breaking of rotational and possibly translational symmetry, antiferromagnetic correlations, and $4a_0$-periodic charge modulations. However a few key differences should be emphasized.

Firstly and most importantly, the charge and spin order of the striped state is a ground state of the material, whereas the modulations observed in the pseudogap are primarily excited states. In STM experiments the energy of different states may be probed by varying the tip-sample bias. The Fourier peaks corresponding to nematicity are most intense at energies near the observed ~ 50 meV "gap" in the pseudogap density of states [28],

indicating that the nematic behavior is primarily a property of quasiparticle excitations. The more stripe-like smectic order parameter is mostly energy-independent, but is generally very weak and has very short correlation lengths. Recent x-ray experiments [36] comparing elastic and inelastic signals in the pseudogap have found that the inelastic scattering associated with excitations is dominant, but some nearly elastic incommensurate scattering peaks are present for $T \gtrsim T_c$. Note that x-ray experiments often lack the energy resolution to distinguish elastic and inelastic signals, espeically if the relevant excitations have energies below ~ 100 meV. However neutron scattering, which has better energy resolution, similarly suggests that the striped state is a ground state, while the pseudogap nematic state emerges through meV-scale excitations [33, 37].

The difference between ground state stripe order and low-lying finite-energy fluctuations has been illustrated through magnetic scattering in $La_{2-x}Sr_xCuO_4$with added zinc impurities, as described in the review [38] and shown in Fig. 1.11. $La_{1.85}Sr_{0.15}CuO_4$ has no elastic spin-ordered superlattice peaks, but does have low-energy incommensurate peaks at 2 meV. The addition of approximately 1% Zn impurities, substituted for Cu, is insufficient to significantly change the carrier density, but does add weak disorder to the material. In the disordered compound $La_{1.86}Sr_{0.14}Cu_{0.988}Zn_{0.012}O_4$, the low-energy peaks near 2 meV are nearly identical, but now sharp zero-energy peaks are also present, implying that the additional Zn impurities stabilize a ground-state spin-stripe order.

It isn't immediately clear why, out of numerous HTSC cuprate materials, LBCO has such a uniquely stable stripe state. However, the stabilization of LBCO's stripes may be caused at least in part by structural transitions occurring near the charge-ordered region of the phase diagram [31]. The relevant structural phases are summarized in Fig. 1.12. It was mentioned above that the copper-oxygen planes can be viewed as the central slices of octahedra. In the low-temperature tetragonal (LTT) structural phase, the octahedra in each unit cell tilts along either the [100] or [100] directions. This distortion provides the spontaneous symmetry breaking along the a and b lattice directions seen in the charge

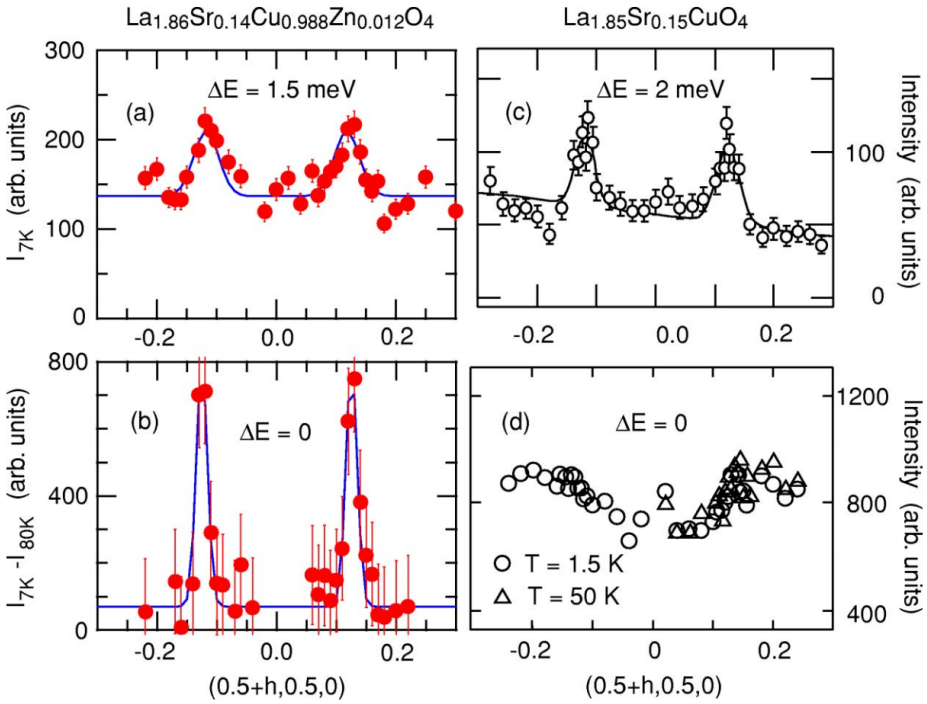

Figure 1.11: **Magnetic Scattering peaks in $La_{2-x}Sr_xCuO_4$with and without Zn impurities.** In "clean" LSCO, stripes are fluctuating and only observed at finite energy (upper right). With the addition of disorder, stripe-like fluctuations are still present at finite energy (upper left) but now stable stripes are also present in the ground state (lower left). Diagram is from [38], but compiled from multiple data sources listed therein.

striped state and creates a corrugated texture within the copper-oxygen planes. Suggestively, the phase line defining the LTT structural phase almost overlaps with the $T_{CO}(x)$ line defining charge order, with a small divergence near $x = 0.155$. However, it is not certain whether structural phase stabilizes the charge order or vice versa. One comment should be added about the way these lattices are described in the literature: because adjacent octahedra would tilt in opposite directions, the high-temperature 3.8Å-wide unit cell of LBCO would technically need to be redefined in the LTT phase in order to remain periodic. However, the tilt angles are extremely small (0.1°) and most researchers simply use the same tetragonal unit cell throughout.

Secondly, the length scales relevant to the striped state are very different from those of the pseudogap. The maximum correlation lengths quoted previously for $La_{2-x}Ba_xCuO_4$'s

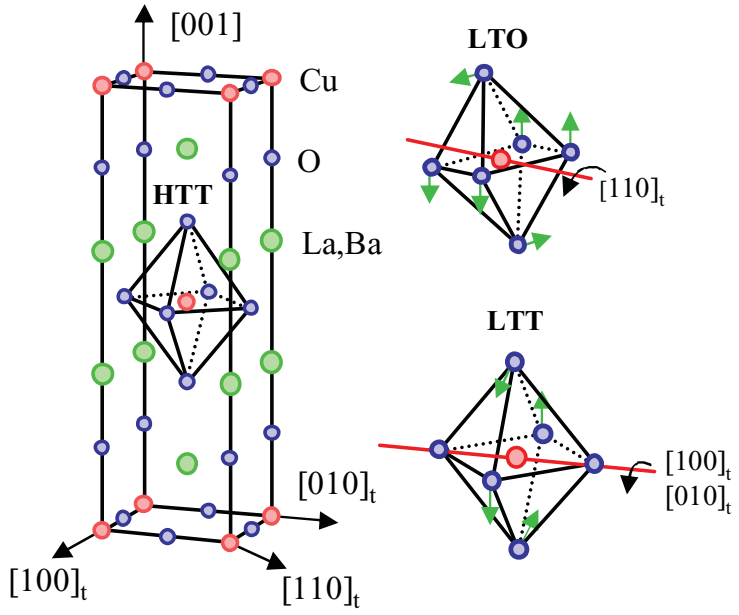

Figure 1.12: **Summary of structural phases in $La_{2-x}Ba_xCuO_4$.** In the high-temperature tetragonal (HTT) phase, CuO_6 octahedra lie flat. In the low-temperature orthorhombic (LTO) phase they rotate along $\langle 110 \rangle$ directions. In the low-temperature tetragonal (LTT) phase, octahedra rotate along $\langle 110 \rangle$ directions.

striped state can be in excess of 100 times larger than the unit cell width. In contrast, the pseudogap charge modulations observed in YBCO and Hg-1201 have $\xi_{max} \sim 10a$ [30]. In many materials, this maximum only occurs well below the superconducting dome, while in $La_{2-x}Ba_xCuO_4$the strongest stripe ordering occurs at the non-superconducting 1/8 anomaly. Again, STM clarifies that only smectic order is short-range in the pseudogap, while nematic order (which x-rays are less sensitive to) may have length scales more comparable to LBCO's stripe order [28].

Finally, while the pseudogap is apparently common to every cuprate superconductor, the combination of a suppressed T_c near $x = 1/8$ and a stable stripe phase has only been observed in a very small number of materials. $La_{2-x}Ba_xCuO_4$and Zn-disordered $La_{2-x}Sr_xCuO_4$have already been mentioned and complete 1/8 anomalies have also been observed [39, 40] in $La_{1.6-x}Nd_{0.4}Sr_xCuO_4$ (LNSCO) and $La_{1.8-x}Eu_{0.2}Sr_xCuO_4$ (LESCO). LESCO is especially unusual because its characteristic temperatures for charge order, spin

order, and the LTT structural phase are relatively well-separated and it may not superconduct for any $x < 0.125$. It should be noted that all of these examples are La-214 materials. As an unfortunate coincidence, none of the La-214 cuprates can be easily cleaved in vacuum, so the large-scan-area STM techniques that have proven fruitful in the pseudogap have not been applicable to LBCO or other superconductors with stable stripes.

1.10 Proposed causes of the striped state

A couple of results have indicated that the stripe state in $La_{2-x}Ba_xCuO_4$is, like high-temperature superconductivity, a collective state of Cooper pairs with d-wave symmetry [41]. Tunneling spectroscopy observes an energy gap (Fig. 1.13(a)) that occurs well above T_c, vanishing only above the charge ordering temperature. Measured at low temperatures, the magnitude of the gap reaches a maximum at $x = 1/8$. ARPES corroborates this evolution of the gap and demonstrates that the gap has the same d-wave symmetry observed in the superconducting state (Fig. 1.13(b)). A simple computer model [42] including Cooper pairing (short-range attraction), long-range Coulomb repulsion, and quenched disorder is able to reproduce a schematic phase diagram, shown in Fig. 1.13(c), where stripes and clumps of charge occur at intermediate carrier densities, as in LBCO.

A proposed *pair density wave* (PDW) state may explain why the co-occurrence of Cooper pairing and charge stripes causes a suppression of T_c [43]. In addition to the d-wave symmetry of the phase of the superconducting order parameter in k-space, the PDW also includes a real-space modulation of the phase, specifically a π phase shift between adjacent stripes within the copper-oxygen plane. Across multiple CuO_2 planes, the PDW order is predicted to stack with the "woodpile" structure depicted in Fig. 1.13(d), with a half-period offset between the stripes in second-nearest planes. Note that the location of the charge stripes is identical to what has been confirmed in scattering experiments, only the addition of a relative phase shift between stripes is new. In this config-

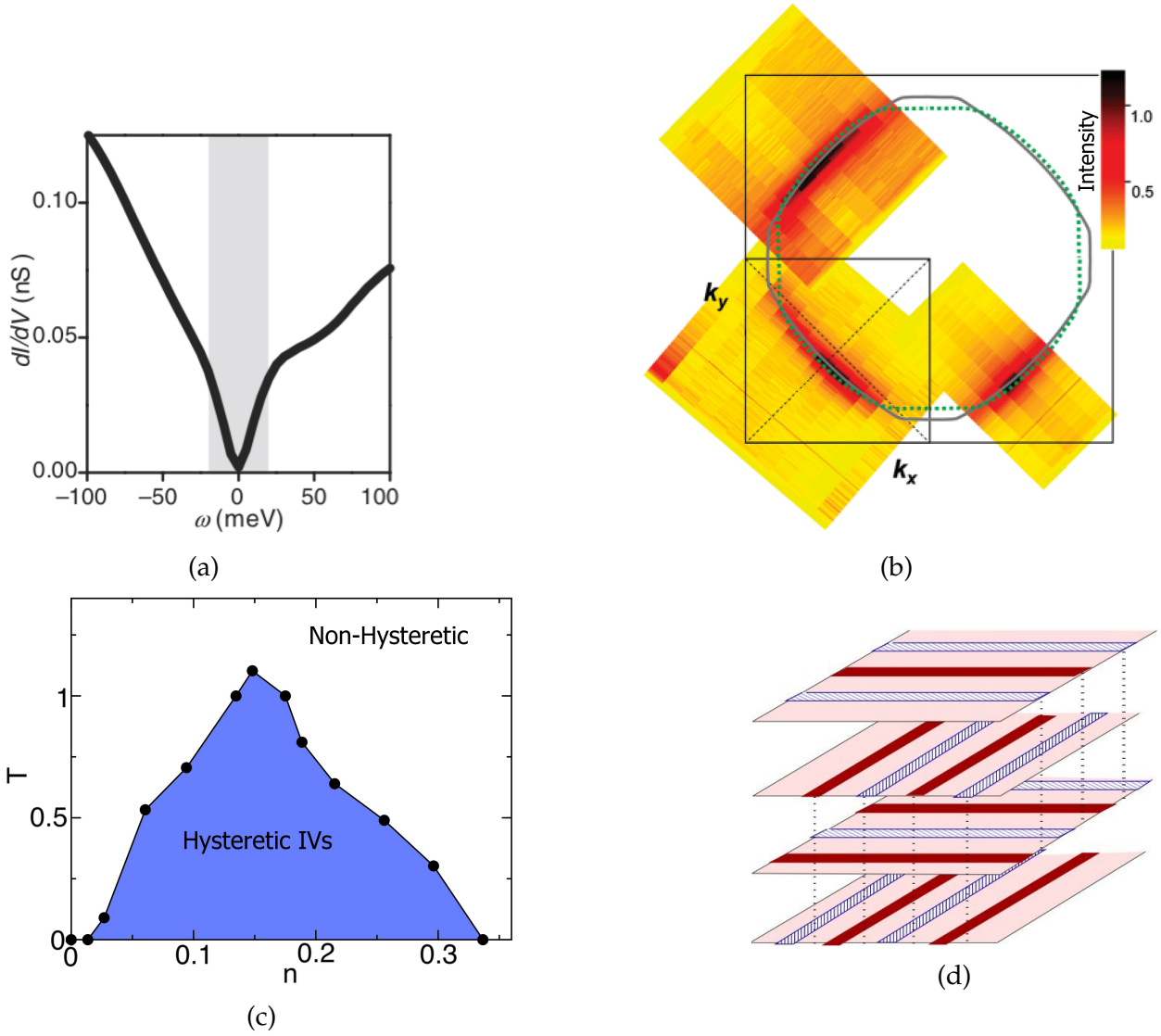

Figure 1.13: **Cooper pairing in the striped state of $La_{2-x}Ba_xCuO_4$.** (a) Tunneling spectroscopy shows that the gap, seen here as a kink in the density of states and illustrated by the gray band, reaches a maximum at $x = 1/8$ and occurs throughout the stripe state, including points above T_c [41]. (b) ARPES on the same sample similarly shows a complete d-wave gap due to Cooper pairing. This spectral map was measured at $T = 16$ K, well above $T_c \sim 4$ K. (c) Simulations with pairing and Coulomb interactions can reproduce a temperature-doping phase diagram with the same kind of intermediate peaked region of stripe order seen in LBCO [42]. Stripes were distinguishable as having hysteretic current-voltage characteristics. (d) Stripes may cause a suppression of T_c via a *pair density wave* state [43], in which a superconducting order parameter is proposed to have a phase that modulates in real space. Copper oxygen planes (pink) stack as shown and adjacent stripes have alternating positive (blue) or negative (red) relative phase.

uration, Josephson coupling between adjacent planes, 2nd-nearest-neighbor planes, and 3rd-nearest-neighbor planes all cancel by symmetry considerations. The only remaining phase-coherent contribution to three-dimensional superconductivity comes from 4th-nearest neighbor CuO_2 planes, which would explain the extremely weak superconductivity and low T_cs observed in the 1/8 anomaly, despite the presence of strong pairing. To date, the real space phase structure of the proposed PDW state has not been explicitly confirmed experimentally, but the existing body of evidence is consistent with its existence. In addition to the previously discussed observation of Cooper pairing in the striped state, some transport experiments in single-crystal $La_{2-x}Ba_xCuO_4$have observed behavior consistent with the PDW's description of two-dimensional superconducting planes with weak interlayer coupling [44]. As shown in Fig. 1.14, careful magnetoresistance measurements on well defined crystal faces of $La_{1.905}Ba_{0.095}CuO_4$ show that the in-plane resistivity ρ_{ab} vanishes at a higher temperature than the interplanar resistivity ρ_c, and that this effect is greatly enhanced by magnetic fields perpendicular to the CuO_2 planes. The anisotropic vanishing of the resistance is consistent with layer decoupling, and the magnetic field enhancement of this resistance anisotropy is interpreted as thermal fluctuations of pancake vortices that are pinned by the Lorentz force more easily when current flows parallel to the CuO_2 planes.

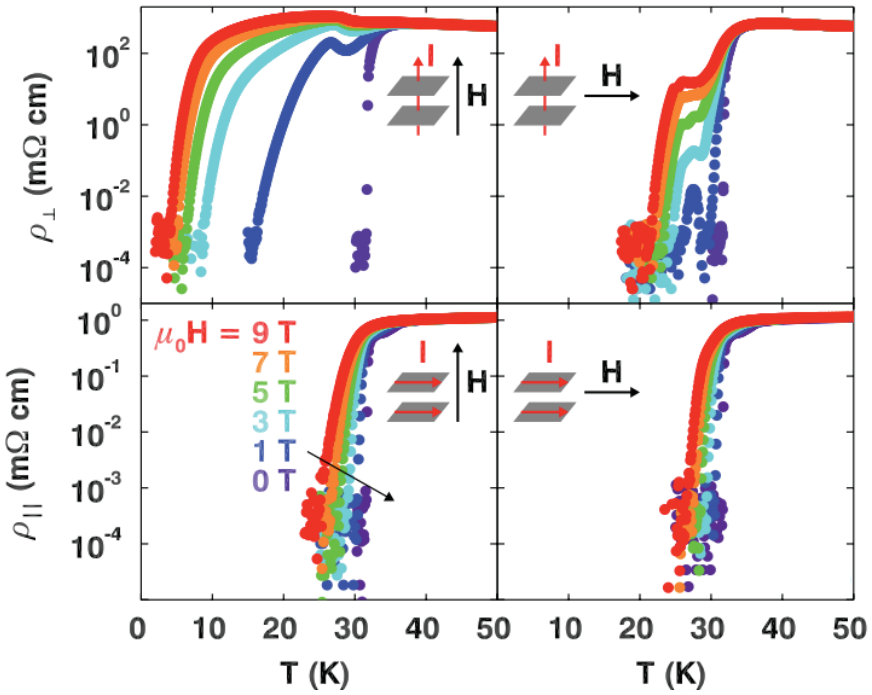

Figure 1.14: **Magnetoresistance measurements from [44] in $La_{1.905}Ba_{0.095}CuO_4$.** With field along the c-axis, superconductivity is observed within the CuO_2 planes (lower left) at higher T than superconductivity between the planes (upper left). Higher magnetic fields exaggerate this anisotropy through the formation of decoupled pancake vortices. Magnetoresistance effects are less significant for field parallel to the CuO_2 planes (upper and lower right), because vortices then maintain coherence along the field direction and pin more easily.

Chapter 2

Low-Frequency Resistance Noise

2.1 Motivation to study noise in LBCO

The experiments shown below seek to detect the presence of the charge-ordered phase in LBCO via its inherent resistance anisotropy. This will be facilitated by studying microfabricated thin film samples, in order to limit the number of charge-ordered domains. Even in the small samples studied here, an extremely large number domains are likely, based on the correlation lengths expected from scattering experiments. For example, in a 50 nm thick, 2 µm x 10 µm LBCO sample, nearly 2×10^5 domains will be present at $x = 1/8$, where $\xi_c \sim 2.5$ nm and $\xi_{ab} \sim 50$ nm. At dopings away from $x = 1/8$, the number of domains will be even greater.

We can expect that for such a large number of domains the percentage of the sample that is charge-ordered along the a-axis and the percentage ordered along the b-axis will be very close to equal, and therefore any measured transport properties will be nearly isotropic. However, as domain walls between a- and b-oriented stripe domains move at finite temperature, small fluctuations in resistance should occur. Therefore, we will seek to probe the striped state through measurements of resistance fluctuations or "noise." This section will outline a general model of the low-frequency fluctuations in solids, and then review previous studies of resistance noise in cuprates.

Historically, low-frequency resistance fluctuations in solid-state materials have been an area of active research. In particular, it was observed in a wide variety of materials - metals, semiconductors, and oxides - that the spectral density S of resistance fluctuations

scale with frequency f as $S \sim 1/f$. The origins of this apparently universal behavior were not well-understood until the model of P. Dutta and P. M. Horn [45].

2.2 Electronic noise and the Dutta-Horn model

Describing the Dutta-Horn model for $1/f$ noise is easier with some context, so we will first describe two simpler types of noise — the Johnson-Nyquist noise of a resistor and the noise of a fluctuating two-level system.

Johnson-Nyquist noise is the voltage noise in a resistive material due to Brownian motion of the charge carriers. It is independent of the voltage or current applied to the resistor (in the absence of Joule heating) and has a "white" or frequency-independent spectrum. The *power spectral density* (PSD) S_{VV} of any time-varying voltage signal $V(t)$ can be defined, at a frequency f, as the squared complex modulus of the Fourier transform $\hat{V}(f)$. For a signal discretely sampled at time intervals Δt,

$$S_{VV}(f) \equiv \hat{V}(f) \cdot \hat{V}^*(f) = (\Delta t)^2 \left| \sum_{n=-\infty}^{\infty} V(n\Delta t)\, e^{-2\pi i f n} \right|. \tag{2.1}$$

For Johnson noise, the power spectral density is found to be

$$S_{VV}(f) = \overline{\hat{V}(f)^2} = 4k_B T R, \tag{2.2}$$

where k_B is the Boltzmann constant, T is temperature, and R is the sample resistance. For a sense of scale, this means a 1 kΩ resistor will generate $\sim 4\text{nV}/\sqrt{\text{Hz}}$ voltage noise at room temperature; a simulation of this flat spectral response is shown in Fig. 2.1(a)-(b). This relation for Johnson-Nyquist noise was originally observed and derived for the specific case of a resistor [46, 47], but was later found to be a specific example of the fluctuation-dissipation theorem [48], which applies to any system that obeys detailed balance and has a dissipative force. In $1/f$ noise experiments at sufficiently high frequencies,

the $1/f$ noise power will decay below the Johnson noise power, so the Johnson noise will be considered as a high-frequency background signal present in most low-frequency noise spectra.

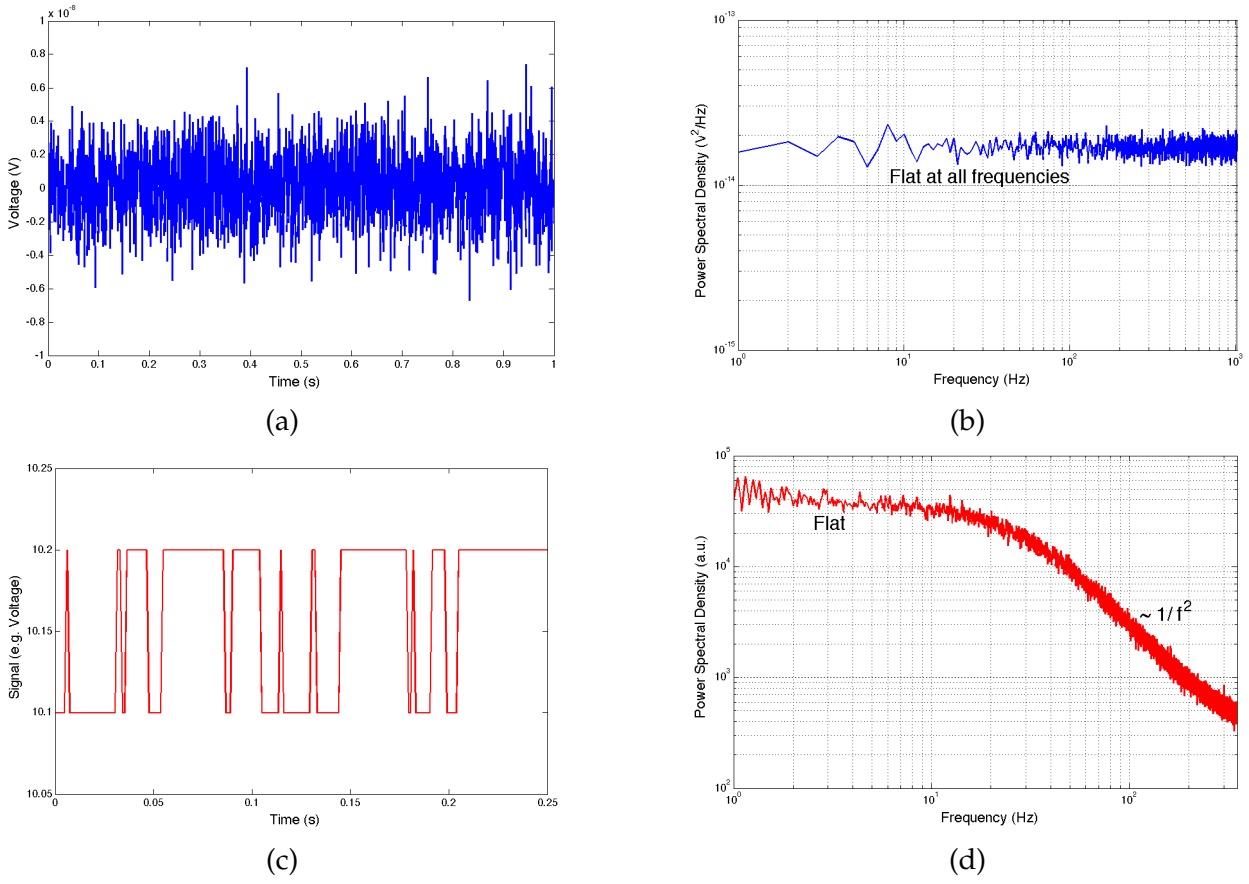

Figure 2.1: **Example voltage noise signals and their power spectral densities.** (a) Simulated time-varying voltage noise signal of a 1 kΩ resistor at 300 K. (b) PSD of Johnson noise, which has a white frequency-independent spectrum. (c) Simulated voltage noise from a two-level system (TLS). (d) Characteristic Lorentzian spectrum of a TLS, which is flat at low frequencies and decays as $1/f^2$ at high frequencies. The turning point of the spectrum is at $f_c \sim 1/2\pi\tau_c$ where τ_c is the lifetime of the states.

We can also imagine a two-level system in which each of the two states has a different resistance and some lifetime τ_c. A symmetric system is assumed for convenience, but this description easily generalizes to the asymmetric case in which the two states have different lifetimes. With a constant current applied, the time-dependent voltage will have the telegraph-like behavior shown in Fig. 2.1(c). The autocorrelation function of the

voltage will be

$$r_{VV}\left(t'\right) \equiv \left\langle \frac{\left[V(t)-V_0\right]\left[V(t+t')-V_0\right]}{\sigma^2} \right\rangle_t = r_{VV}(0)e^{-t'/\tau_c}. \tag{2.3}$$

Then the Wiener-Khinchine theorem [49] states that the power spectral density is given by the Fourier transform of r_{VV},

$$S_{VV}(f) = \int_{-\infty}^{\infty} r_{VV}(t')e^{-2\pi i f t'}dt' = 4r_{VV}(0)\frac{\tau_c}{1+(2\pi)^2\tau_c^2 f^2}. \tag{2.4}$$

In the limit $f \ll \tau_c$ this *Lorentzian* spectrum gives an approximately constant S_{VV} and when $f \gg \tau_c$, $S_{VV} \propto 1/f^2$, as shown in Fig. 2.1(d).

In the Lorentzian spectrum of Fig. 2.1(d), the variation with frequency f near the characteristic frequency $1/\tau_c$ is somewhere between f^0 and f^{-2} and could be considered to be "nearly $1/f$." This approximation of $1/f$ behavior is especially pronounced if we consider a superposition of several Lorentzian spectra with different characteristic frequencies that are roughly logarithmically spaced, as shown in Fig. 2.2(a). This could describe a system in which resistance depends on a small number of two-level fluctuators as pictured in Fig. 2.2(b). Characteristic fluctuation frequencies may, for example, vary according to thermally activated hopping across energy barriers of different heights.

The Dutta-Horn model considers the spectrum generated by an ensemble of two-level thermally activated fluctuators that couple to resistance [45]. The total PSD is a continuous sum of Lorentzians with different characteristic times τ

$$S(\omega) \propto \int_0^{\infty} \frac{\tau}{\omega^2\tau^2+1} D(\tau)d\tau, \tag{2.5}$$

where $D(\tau)$ is the distribution of characteristic fluctuation times. The integral can produce a variety of spectra depending on the distribution $D(\tau)$. If we consider the case where $D(\tau) \propto \tau^{-1}$ within the range τ_1 to τ_2, and $D(\tau) = 0$ elsewhere, then equation 2.5

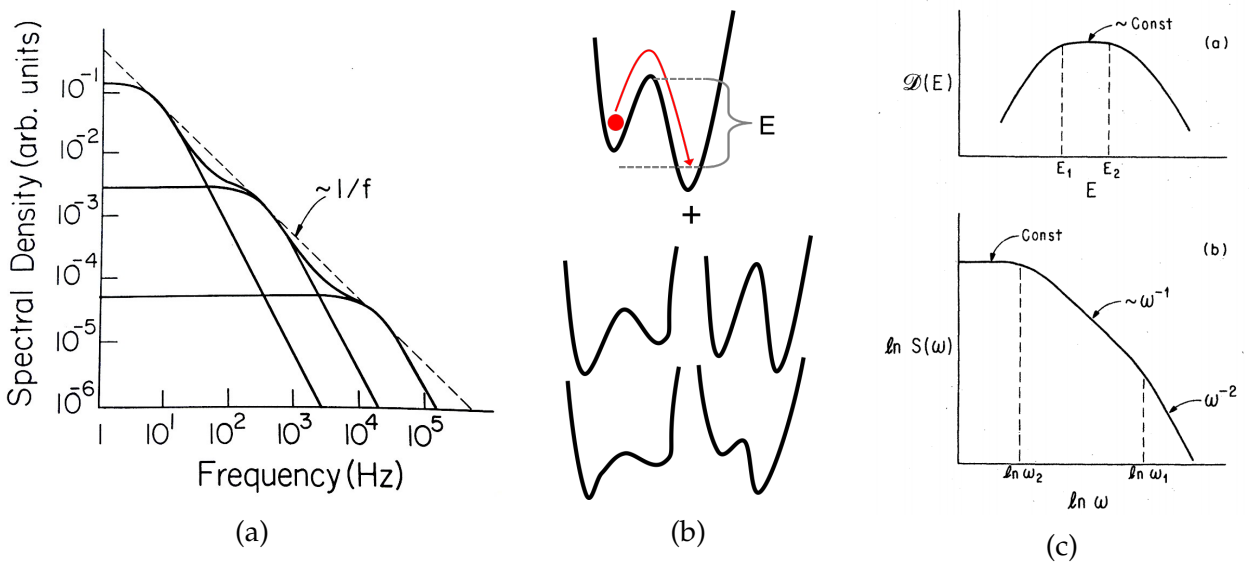

(a) (b) (c)

Figure 2.2: **Creation of $1/f$ spectra from superposition of TLS spectra.** (a) Addition of three Lorentzian spectra. (b) Ensemble of thermally activated two-level systems with various energy barriers E as considered in the Dutta-Horn model. (c) Fluctuators with a constant distribution of energy barriers give noise that is $1/f$ over some frequency range.

becomes

$$S(\omega) \propto \frac{\arctan\left(1/\omega\tau_1\right) - \arctan\left(1/\omega\tau_2\right)}{\omega}. \tag{2.6}$$

If $\tau_2^{-1} \ll \omega \ll \tau_1^{-1}$ then the spectral density has the scaling $S(\omega) \propto \omega^{-1}$. If the state switching of each TLS is caused by thermal activation, then the switching time of the TLS will be related to its energy barrier E by

$$\tau = \tau_0 \exp\left(E/k_B T\right). \tag{2.7}$$

If the number of fluctuators is defined as N, then the distribution of energy barrier heights is

$$D(E) = \frac{dN}{dE} = \frac{dN}{d\tau} \cdot \frac{d\tau}{dE} = D(\tau)\frac{\tau_0}{k_B T} e^{E/k_B T} = D(\tau)\frac{\tau}{k_B T}. \tag{2.8}$$

So the previously stated condition for $1/f$ noise, that $D(\tau) \propto \tau^{-1}$ over a range τ_1 to τ_2, is

equivalent to the statement

$$S(\omega) \propto \omega^{-1} \quad \text{iff} \quad D(E) = \text{constant} \quad \text{for} \quad k_B T \ln(\tau_1/\tau_0) \lesssim E \lesssim k_B T \ln(\tau_2/\tau_0), \quad (2.9)$$

as depicted in Fig. 2.2(c). So $1/f$ noise requires thermally activated processes to have a constant energy distribution.

The real strength of the Dutta-Horn model, however, goes beyond this equivalence of $1/f$ to constant $D(E)$, and considers energy distributions that are slowly varying, rather than constant. In particular, it shows that when $D(E)$ varies slowly compared to $k_B T$, the power spectral density of resistance noise will scale as $1/f^{\alpha}$ with $0.8 \leq \alpha \leq 1.4$ and can qualitatively be considered "$1/f$" [45]. The integrand in equation 2.5 can be combined with equation 2.7 and Taylor expanded for $dD(E)/dE \ll k_B T$. This gives the PSD

$$S(\omega, T) \propto \frac{k_B T}{\omega} D\left(\tilde{E}\right), \quad (2.10)$$

where $\tilde{E} = -k_B T \ln(\omega\tau_0)$ and only the first expansion term has been kept. If $D(E)$ is constant, this gives the $1/f$ behavior derived in equation 2.9, but otherwise $D(E)$ will cause additional ω and T dependence. Equation 2.10 implies that if ω and T are simultaneously varied so as to keep $\tilde{E}$ constant, then $(\omega/k_B T)S(\omega, T)$ will also be constant, which can be stated as a pair of differential equations. Solving these equations gives

$$\alpha(\omega, T) = 1 - \frac{1}{\ln(\omega\tau_0)} \left(\frac{\partial \ln S(\omega, T)}{\partial \ln T} - 1 \right), \quad (2.11)$$

where α has been defined as $-\partial \ln S_{VV}/\partial \ln \omega$, the local exponent of the $1/f^{\alpha}$ noise.

Equation 2.11 is an important prediction of the Dutta-Horn model, as it relates deviations of α from 1 to temperature variations in the noise. Because these two noise properties can be measured independently, this relation can be checked against experiment, as shown in Fig. 2.3. Note in particular the energy distribution in Fig. 2.3(b). The

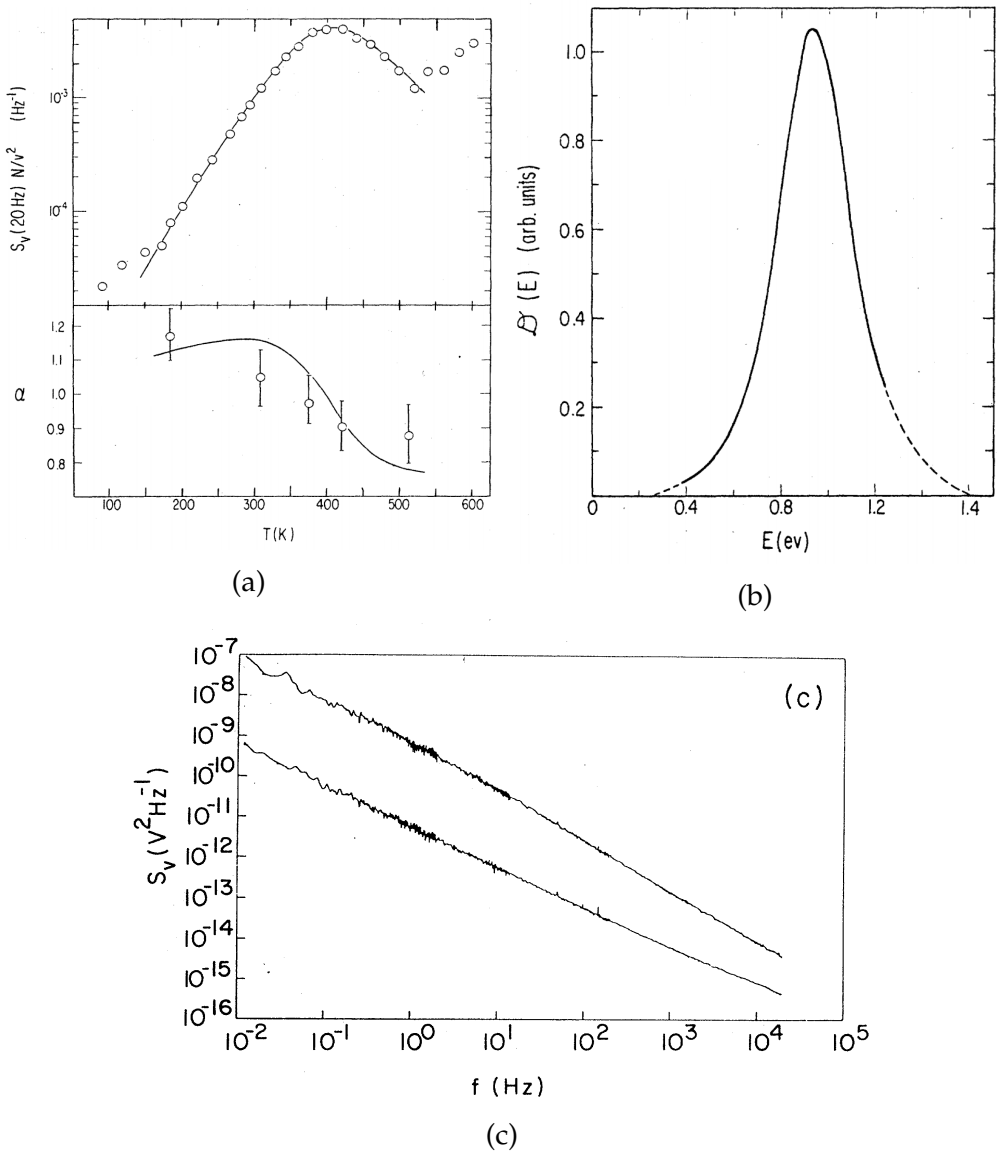

Figure 2.3: **Experimental confirmation of $1/f$ noise and the Dutta-Horn model.** (a) Dutta-Horn analysis of noise in Ag films, from [50]. Solid line in the upper curve is an empirical fit to S_V and is used to calculate the noise exponent α via equation 2.11. Solid line in the lower plot is this prediction, which agrees well with the measured exponents (circles). (b) The Dutta Horn model also allows for calculation of the fluctuation energy distribution by equation 2.10, and for the Ag noise data gives a peaked function. Note that although $D(E)$ is far from constant, it *is* slowly varying compared to k_BT, which is only 25 meV at room temperature (approximately the width of the solid line). (c) A different experiment on thick oxide films [51] shows that $1/f$ behavior typically persists over many orders of magnitude. The frequency limits associated with the finite width of $D(E)$, as depicted in Fig. 2.2(c) are usually not encountered in practice.

Dutta-Horn requirement that $D(E)$ vary slowly compared to k_BT does *not* mean that it doesn't vary at all; k_BT is typically small and still allows for a large number of energy distributions. Comparisons of the Dutta-Horn model with experimental $1/f$ data in metals typically gives $D(E)$ as a function peaked at some eV-scale energy. This is a plausible distribution and peak energy for many processes that would be expected in solids, e.g. oxidation of a metal, or population and depopulation of charge traps. Therefore, the Dutta-Horn model is considered a much more realistic explanation of $1/f$ noise than the initially described strict requirement that $D(E) =$ constant.

The discussion of the Dutta-Horn model concludes with a summary of some properties of general $1/f$ noise:

1. $S_V(\omega) \propto (\text{sample volume})^{-1}$. This is a plausible dependence on sample volume if the fluctuators described by the Dutta-Horn model are properties of the bulk material. The experiments on LBCO will not explicitly study this volume dependence, but will include volume normalization in order to best compare the noise in different samples. The increase in noise at low volume also motivates our decision to use thin film growth and lithographic microfabrication in order to create LBCO samples with the smallest possible volumes.

2. $S_V \propto \langle V \rangle^2$. The PSD will scale quadratically with the time-averaged voltage or the current across the device, which is consistent with the notion that $1/f$ noise is caused by *resistance* fluctuations. The PSD is typically measured in units of V^2/Hz, so if the resistance noise is caused by fluctuations ΔR, then Ohm's law gives a voltage fluctuation $\Delta V = I(\Delta R)$ and $S_V \propto (\Delta V)^2 \propto I^2(\Delta R)^2 \propto V^2(\Delta R)^2/R^2$. Normalizing by the DC voltage squared will be important if comparing samples with different resistances, or different driving currents. Also, high currents should be used in order to best resolve $1/f$ resistance fluctuations above background voltage noise sources, such as Johnson-Nyquist noise and amplifier noise.

3. $S_v \propto f^{-\alpha}$ with $0.8 \lesssim \alpha \lesssim 1.4$. As shown in Fig. 2.3(c) this behavior can span extremely wide frequency ranges, although this may be challenging to observe. At high frequencies, the $1/f$ noise is small and may be hard to distinguish from sources of background noise, while at low frequencies experiments can become prohibitively time-consuming. Note the total energy of fluctuations in a $1/f$ sample is proportional to $\int_0^\infty f^{-\alpha} df$ and appears to diverge at both ends of the integral. This problem is resolved by the frequency limits imposed by the finite width of typical fluctuator energy distributions, as depicted in Fig. 2.2(c), but these limits are usually outside of experimentally accessible frequency ranges. The exponent α is typically close to 1 because, in equation 2.11, $|\ln(\omega\tau_0)| \gg 1$. The thermal hopping "attempt frequency" τ_0^{-1} is usually assumed to be very large, e.g. comparable to the material's Debye frequency. Another consequence of the fact that $\omega \ll \tau_0^{-1}$ is that $\ln(\omega\tau_0)$ and therefore α, by equation 2.11, should be insensitive to changes in ω.

2.3 Low-frequency noise in cuprates

In most solids with $1/f$ resistance noise, the microscopic events responsible for the noise are not explicitly known, although a number of researchers such as Weissman [52, 53] have developed diagnostic noise techniques for investigating noise in systems of interest. $La_{2-x}Ba_xCuO_4$ offers a unique opportunity in this regard, as a clear fluctuation source is suggested by the disordered spontaneous symmetry breaking of the striped state. When a DC current is applied to LBCO and a charge-ordered domain has stripes parallel to the current direction, the accumulated charge carriers in the stripe provide a high-carrier-density pathway for current to flow, lowering resistance. When charge-stripes are perpendicular to the current within a region, carriers must tunnel across the antiferromagnetic regions between stripes, and resistance is high. In LBCO, the two-level systems considered in Section 2.2 would correspond to stripe-ordered regions. Stripe orientation

along the crystal's a-axis, and orientation along the b-axis are the two states possible for each TLS; the energy barrier between the two states likely depends on the local pinning of the striped state to disorder.

Because the a-b resistance anisotropy of LBCO has not been explicitly measured, it is difficult to estimate the possible magnitude of resistance noise in the striped state. However, we can consider the plausibility of stripe-detection with $1/f$ noise by comparison to a few other experiments. X-ray experiments [34] have estimated that the peak-to-trough amplitude of the striped charge modulation in $La_{1.875}Ba_{0.125}CuO_4$ is only 0.063 holes, which suggests that the resistance anisotropy and therefore noise in LBCO may be weak even though LBCO has larger charge- and spin-order correlation lengths than most other cuprates, as discussed in Section 1.9. One of the few direct measurements of a-b transport anisotropy in a HTSC material was reported in untwinned $La_{2-x}Sr_xCuO_4$ and $YBa_2Cu_3O_{7-y}$ crystals [54], in which $\rho_a/\rho_b \sim 2.5$ for some dopings and temperatures in YBCO. However, it is not clear the extent to which these results generalize to other samples. The YBCO measurements observed maximal above-T_c anisotropy both at extreme underdoping and optimal doping, with $\rho_a/\rho_b \sim 1$ at intermediate dopings. This observation of anomalous behavior in two "hot spots" of the phase diagram differs from most other observations of symmetry breaking in the pseudogap, and because of the difficulty in obtaining untwinned samples, few experiments have sought to reproduce these experiments.

Later magnetotransport experiments on $La_{2-x}Sr_xCuO_4$ thin films sought to observe similar resistance anisotropy, by measuring the zero-field Hall resistance R_{xy} as a function of in-plane angle [55]. With a charge-stripe orientation at some angle to the direction of applied current, anisotropic transport could cause mixing of longitudinal and transverse voltages even in the absence of magnetic field. However, it was found that the dominant source of conductance mixing was caused by atomic-height terraces in the substrate, which caused anisotropic defect formation and hence conductance in the LSCO

films. In non-superconducting materials with well-established charge ordering, such as $NbSe_3$, low-frequency noise has been used successfully to detect the presence of an inhomogeneous fluctuating electronic phase. [56]. At critical electric fields where the $NbSe_3$ charge density wave begins to slide, the relative change in the noise PSD is much greater than the relative change in the DC resistance, demonstrating the improved sensitivity of noise techniques to charge order, over standard DC transport techniques.

Previous studies from the Van Harlingen research group [57, 58], on resistance fluctuations in the cuprates also suggest that the stripe state should be detectable as noise. As described in Fig. 2.4(a)-(c), resistance measurements in narrow (250 nm) wires of slightly underdoped $YBa_2Cu_3O_{7-y}$ found telegraph-like noise between T_c and approximately 150 K, consistent with noise originating from a pseudogap phase such as an electron nematic. Current-voltage curves were observed to be hysteretic below T_c suggesting that the nematic behavior may persist into the superconducting state. In wider (3 µm) YBCO wires, individual fluctuators were mostly unobservable, but the combined behavior of many fluctuating stripe domains was observable via the power spectral density. Compared to the high-temperature background PSD, additional noise turns on below a temperature T_E which is comparable to T^* (Fig. 2.4(d)). This noise onset temperature was found to correlate with the measurement frequency as given by the Arrhenius equation $f = f_0 \exp(-\Delta E / k_B T_E)$.

However, some details of the measurements in [57, 58] complicate the interpretation of the resistance noise as fluctuating nematic order or stripes. The fit of the data to Arrhenius behavior indicates that the onset of noise is described solely by thermally activated hopping between existing states, rather than a phase transition in which new fluctuation states would emerge. The activation energy for this process was found to be ~ 0.4 eV in most samples. This is larger than the ~ 150 meV quasiparticle energies observed in the pseudogap by STM [28], but is comparable to the activation energy for oxygen diffusion in YBCO [59]. At least one sample in [58] also demonstrated significant changes

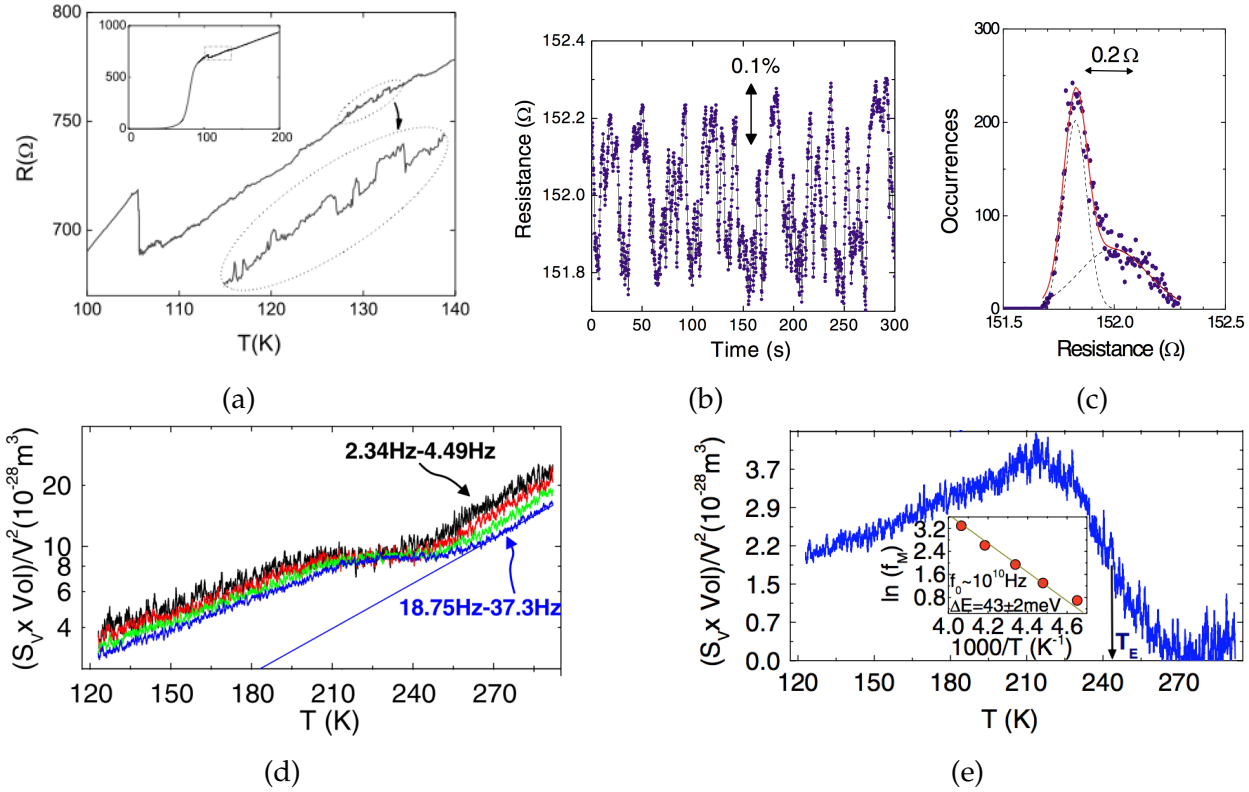

Figure 2.4: **Previous measurements of resistance noise in YBCO.** (a) Resistance as a function of temperature (inset) with two levels of zoom onto a noisy region of the curve. In this 250 nm wide x 500 nm long YBCO sample with T_c ∼75 K, noise begins below about 150 K, which is comparable to T^*. The noise may be caused by the pseudogap nematic phase. (b) Telegraph-like noise at 100 K in the same sample. (c) Histogram of values for resistance values from (b), showing clear bimodal behavior. (d) Integrated Normalized PSD vs. temperature in a 3 µm wide x 15 µm long YBCO wire with T_c =58 K. Different color curves indicate different octaves of integration. As the sample is cooled, the noise observed at high temperatures decays exponentially, but near 220 K, an additional noise source turns on. (e) With the high-temperature background subtracted, a peak is visible in $S_V(T)$; T_E was defined as the temperature where the excess noise reached half its maximal value. Plotting T_E and noise frequency (inset) gives a good fit to Arrhenius behavior, suggesting the noise is caused by thermal activation rather than a sharp phase transition.

in S_v between temperature cycles. In other words, the noise in YBCO may be caused by mobile oxygen dopants rather than any correlated electron state. Since $La_{2-x}Ba_xCuO_4$ is cation-doped rather than oxygen doped, we can rule out this alternative source of noise.

Additionally, it was observed that while the magnitude of S_V changes with doping, the noise onset temperature T_E is doping-independent, in contrast to measurements

of T^* through other techniques. The possible nematic correlation length implied by the noise experiments is also at odds with other pseudogap experiments. Many of the YBCO noise samples, including at least one 3 μm-wide wire showed two-level resistance noise, suggesting a single fluctuating domain comparable to the sample size; in contrast, STM and x-ray have suggested a charge-order correlation length of ≤ 5 nm. Using a technique described in [60] noise anisotropy measurements were also performed in a cross geometry fabricated from a YBCO film and the anisotropy parameter $S_{\text{anis}} = \langle \det(\delta\boldsymbol{\rho}) \rangle \,/\, \left\langle \text{tr}\left[(\delta\boldsymbol{\rho})^2\right] \right\rangle$ was calculated, where $\boldsymbol{\rho}$ is the 2D resistivity matrix. S_{anis} should be 1 if the noise is scalar, and -1 if the noise is caused by rotation of an easy conductance axis which would be possible for stripes. The noise in a YBCO sample with T_c =58 K was found to have $S_{\text{anis}} \sim 0$, which may suggest that the fluctuation source is not stripe-like. More importantly, S_{anis} was also temperature-independent, implying that the additional noise appearing below 220 K in most samples did not change the local resistance isotropy of the dominant fluctuators. In addition to the inherent scientific interest in LBCO's 1/8 anomaly, the complications in the YBCO noise measurements also motivated our study of resistance fluctuations in LBCO. LBCO's strong stripe phase and stable oxygen stoichiometry suggest that measuring its striped state through resistance noise should be more straightforward and more meaningful than equivalent measurements in YBCO.

Finally, we briefly discuss the noise model of Carlson [61], which was developed to explain the results of [57] and provides a useful description of fluctuations in cuprates. In both LBCO and other cuprates, the correlation length of charge ordering has been experimentally confirmed to be small (≤ 50 nm) and the material is inherently disordered due to the distribution of dopant atoms. Therefore, domain formation is expected, as depicted in Fig. 2.5(a). These domains can be mapped onto a resistor network (Fig. 2.5(b)), in order to compute the total sample resistance for a given domain configuration, and can also be

mapped onto the random-field Ising Hamiltonian,

$$H = -J \sum_{\langle i,j \rangle} \sigma_i \sigma_j - \sum_i (h + h_i)\, \sigma_i, \tag{2.12}$$

in order to compute time-evolution of the domains at finite temperature. Domain orientation is represented as a spin-like variable σ_i at site i, the coupling coefficient J represents the tendency for neighboring domains to coalign, and the random field $(h + h_i)$ models the pinning of the stripe domains to underlying disorder in the material. Thermal activation of the domains is seen to randomly flip their orientation, causing resistance noise. One of the surprising results of the Carlson model is that even in multi-domain systems, such as the 2D 6×6 domain grid modeled for Fig. 2.5(c), the noise may be dominated by a single fluctuator due to the correlation of adjacent domains in regions with weak pinning. This may explain why some of the YBCO noise experiments, in samples that are large compared to the domain size, still show two-level resistance noise.

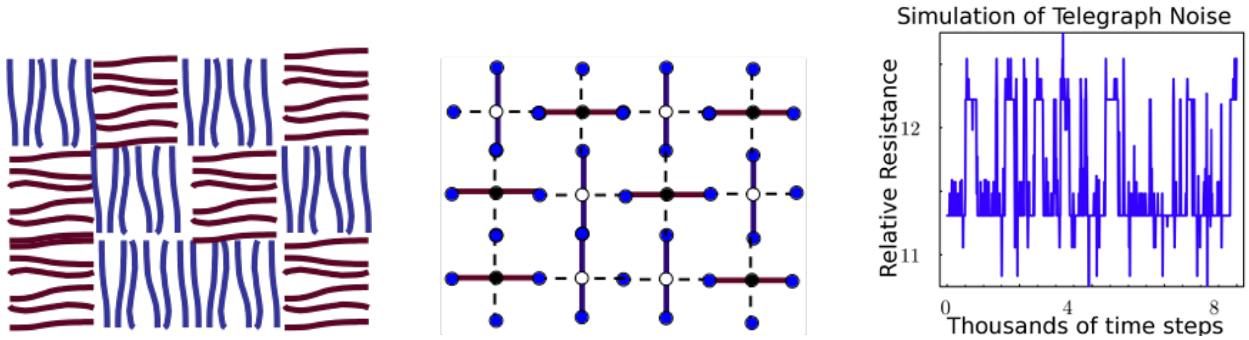

(a) (b) (c)

Figure 2.5: **The model for cuprate resistance noise described in [61].** (a) A two-dimensional configuration of stripe domains is mapped onto a (b) resistor network and the Ising Hamiltonian (to compute dynamics). (c) The resulting resistance fluctuates, and may be dominated by a single large fluctuator even for a large number of domains. The example shown here was for a 6×6 grid and shows clear telegraph-like behavior.

Chapter 3

Experimental Methods

3.1 Synthesis of $La_{2-x}Ba_xCuO_4$ powders and deposition sources

The $La_{2-x}Ba_xCuO_4$thin films samples studied in this work were grown by pulsed laser deposition (PLD), a physical vapor deposition technique. The goal of PLD is perfect stoichiometric transfer of material from a deposition source, or *target*, to a substrate. Therefore, the deposition source, usually a polycrystalline ceramic, must have the same stoichiometry as the desired film material.

Simple deposition sources can be synthesized through solid-state reaction as shown in Fig. 3.1. Oxide powders are repeatedly ground, mixed, and fired in a furnace. Diffusion of material between adjacent grains eventually mixes the constituent elements and hopefully forms the desired phase. As an example, the expected reaction for Nd-doped LSCO would be

$$\begin{aligned} & 0.74\,(La_2O_3) + 0.2\,(Nd_2O_3) + 0.12\,(SrCO_3) + CuO + 0.03\,(O_2) \\ \rightarrow \quad & La_{1.48}Nd_{0.4}Sr_{0.12}CuO_4 + 0.12\,(CO_2)\,. \end{aligned} \tag{3.1}$$

Solid state reaction was used to synthesize initial LBCO, LNSCO, and LESCO deposition sources, but the quality of the films deposited from these sources was insufficient. Because target quality correlates with the quality of films grown from that target, we pursued a more precise metalorganic synthesis route for LBCO powders and targets.

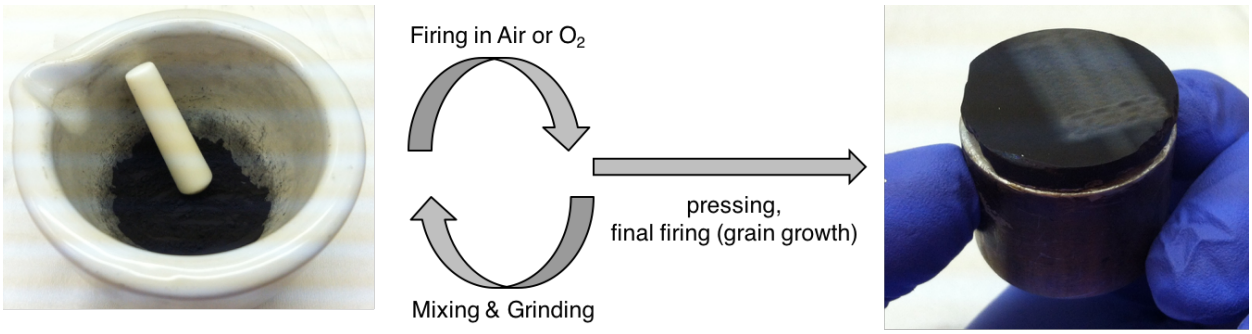

Figure 3.1: **Solid-State Reaction of Oxides.** Single metal oxides are mixed with the appropriate stoichiometry, ground in a mortar and pestle (or a ball mill), and fired in a high-temperature furnace with oxygen or air. The grinding and firing is repeated as needed, then the final powder is pressed into a pellet and fired again. The final firing step is intended to cause grain growth and close pores in the ceramic material, improving density. The powder and pellet shown here is $La_{1.48}Nd_{0.4}Sr_{0.12}CuO_4$.

To define the desired standards of quality for LBCO deposition targets, we require some general discussion on the correlation between target properties and film properties in physical vapor deposition.

Quality of a PLD-grown film material depends critically on homogeneity and density of deposition sources [62]. Laser ablation of low-density targets may cause release of loosely connected grains, increasing the occurrence of large, possibly misoriented particles in the grown film [63], as described in Fig. 3.2. Accumulation of large particles in the film can occur either by direct exfoliation of solid material from the target, or by transfer of large droplets of molten material that splash onto the substrate. Even if these large material-transfer events do not occur during deposition, target porosity and granularity may still contribute to inhomogeneous evaporation. For example, it is known that during laser ablation of conducting microstructures, plasmonic enhancement of the local electric field can generate "hotspots" where rapid evaporation occurs [64]. In a low-density PLD target, such plasmonic effects will cause rough areas in the target surface to evaporate faster and more violently, which enhances evaporation from grain boundaries and lowers the density of low-density surface patches even further [63]. It could be said that, because laser ablation has an inherent tendency towards surface roughening, beginning

each growth with the densest possible deposition source is critically important.

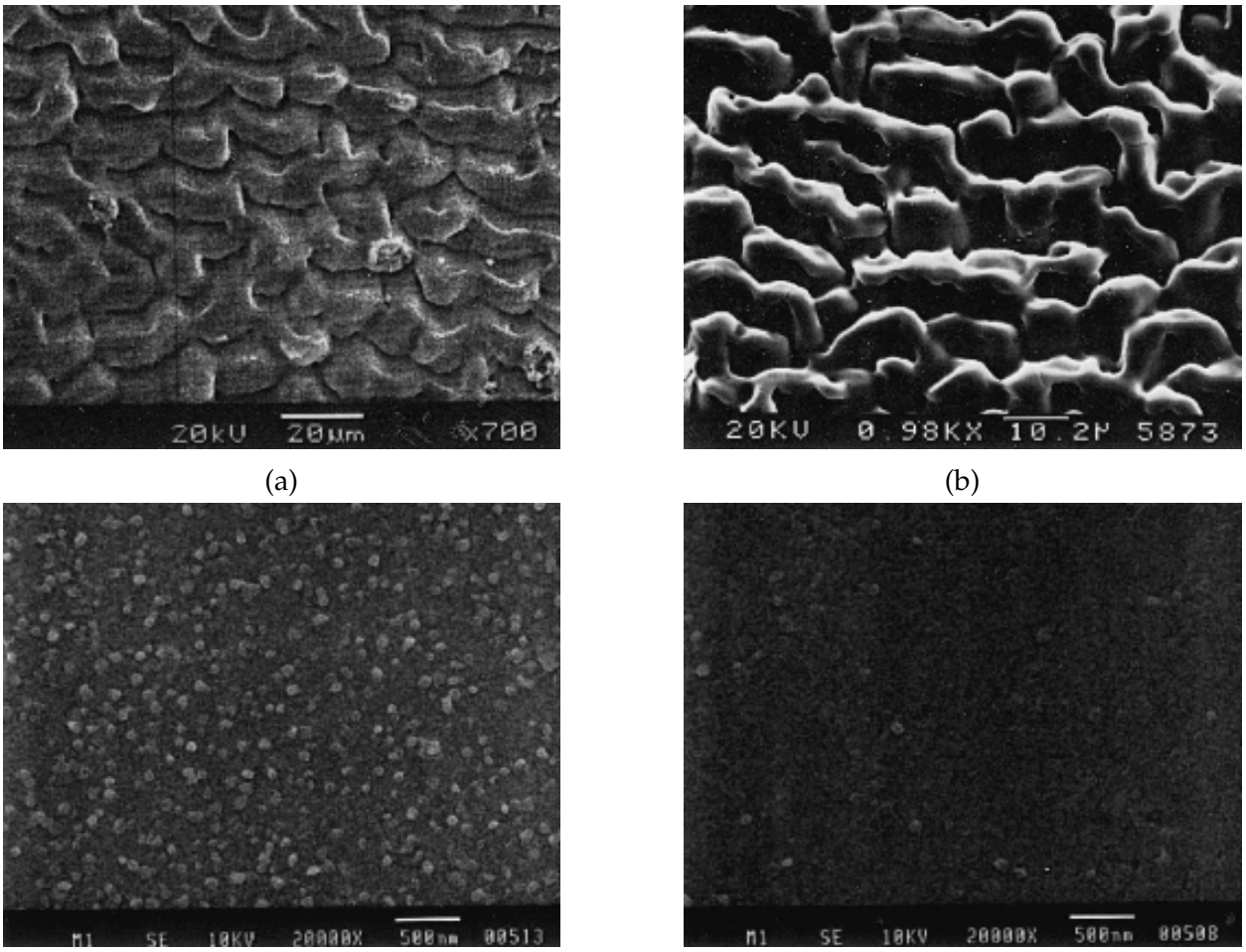

(a) (b)

(c) (d)

Figure 3.2: **Target surface roughening and generation of film particulates with sparse and dense TiO_2 deposition sources.** (a) Sparse TiO_2 target after after 200-300 pulses per site of 1 J/cm^2 Nd:Yag radiation. Pits are visible where large pieces of material have been ejected. (b) Dense TiO_2 target after same exposure. No evidence of ejection of large particles, but surface roughening is apparent; roughening increases with additional exposure (c) Film deposited from sparse TiO_2 target, with lots of particulates. (d) Film deposited from dense TiO_2 target, with fewer particulates. From [63].

The small interaction volume of pulsed laser light with the target surface and the highly directional deposition plume suggest that chemical impurities or inhomogeneities in the target will translate to inhomogeneities in the deposited film. Some work on graphite deposition has indicated that source inhomogeneities can also cause a spatially varying evaporation rate [65]. Similar effects of low-density and inhomogeneous targets

have been reported in other physical vapor deposition techniques, such as cathodic arc deposition [66] and DC sputtering [67], in addition to PLD.

PLD targets may also be created through consolidation of oxide powders synthesized through chemical routes, often involving complexes of metal ions with organic molecules. Metalorganic techniques can offer some advantages over solid state reaction. Because the reaction process occurs on the scale of individual metal ions (rather than at the boundaries of large grains), metalorganic techniques can provide extremely good chemical homogeneity and phase purity. Metalorganics also tend to produce powder with fine-grained microstructure that is easy to compress into dense targets. If powders of sufficient quality are synthesized, then pelletization of said powders into useful PLD targets is relatively straightforward.

A variety of metalorganic techniques have been used to synthesize oxide powders, but many are challenging to implement successfully. For several metalorganic chemistries, the relevant metalorganic complexes are depicted in Fig. 3.3. In all, the goal is to bind organic molecules to metal ions in such a way that the metal ions are kept separate until temperatures at which the organics burn off and the metals oxidize and coalesce. The most common metalorganic technique for ceramic powders is perhaps the Pechini process, in which metal cations are chelated by an organic acid, which is then polymerized and calcined. Possible limitations of the Pechini process include unintentional precipitation if the solution pH isn't precisely controlled, residual carbon in the finished sample, or inhomogeneity due to an incorrect ratio of cations to chelating compounds.

Steric entrapment has been shown to produce polycrystalline ceramics of quality comparable to those synthesized via more traditional precursor routes, but with considerably simpler chemistry and process control [71, 72, 73]. In a steric entrapment process, dissolved metal salts and polymer are mixed and dehydrated so as to embed metal ions in random network of polymer. In contrast to most other metalorganic techniques, explicit metal-organic bonds do not need to be considered; the space-filling polymer is

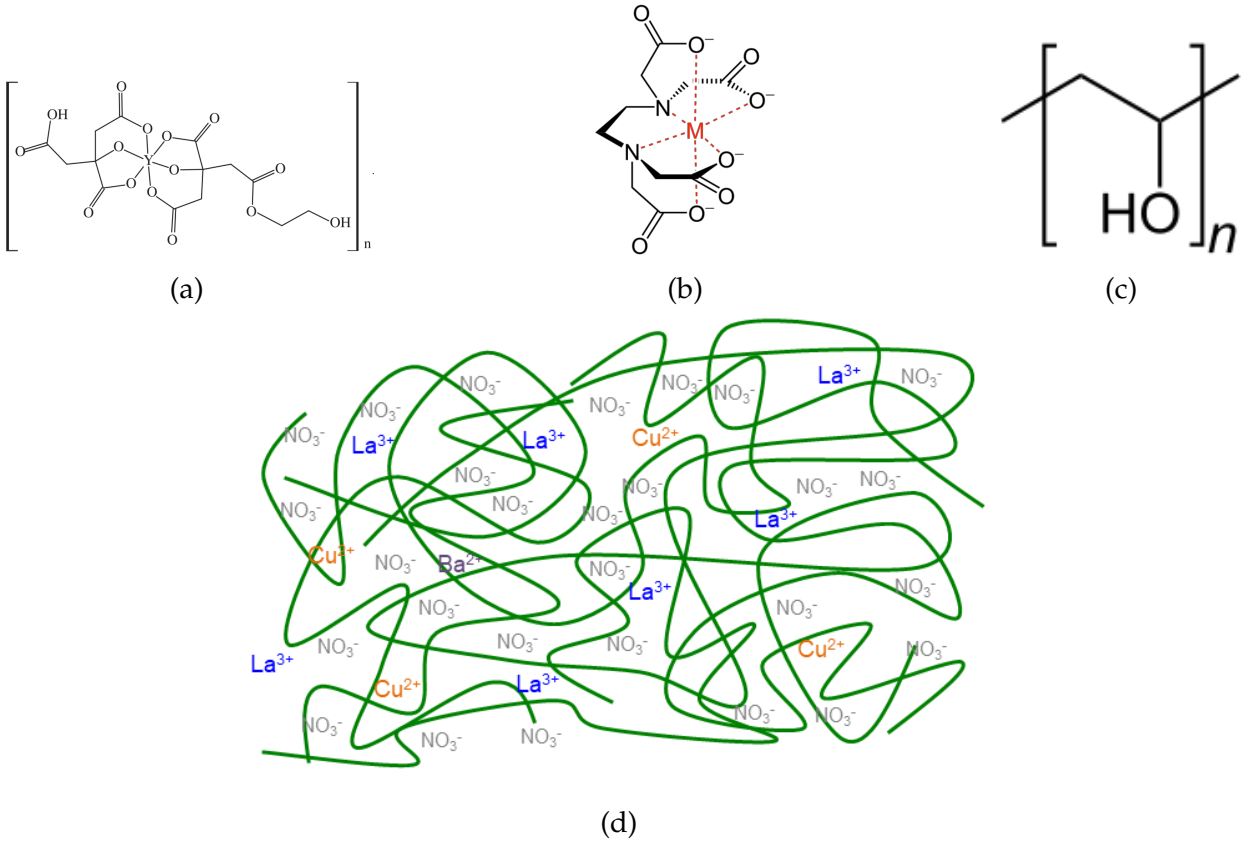

Figure 3.3: **Binding of metal ions to organic molecules in metalorganic ceramic synthesis.** (a) In the traditional Pechini process, metal ions are chelated by one organic molecule and then polymerized by another. Here a Y^{3+} ion is enveloped by two citric acid molecules (left), bound with an ethylene glycol molecule (right). (b) Alternative metalorganic processes involve chelation by ethylene-diamine-tetraacetic acid. (c) The monomer of polyvinyl alcohol which was used here for synthesis of LBCO powders by steric entrapment, and as a binder during pelletization. The OH groups can function as weak binding sites, but in our application there are far more cation valences than organic binding sites. Molecular diagrams from [68, 69, 70]. (d) Sketch of the random ion-polymer matrix formed by steric entrapment. Green lines indicate polymer. The precursor formation does not rely on specific metalorganic bonds.

enough to prevent premature precipitation of the metal. Working closely with the research group of Waltraud Kriven, we used a steric entrapment technique to synthesize phase-pure nanoscopic LBCO powders, which were pelletized into homogeneous and dense ceramic PLD targets.

The high-purity $La_{2-x}Ba_xCuO_4$ ($x = 0.095$, 0.125 and 0.155) powders used in this study were synthesized through steric entrapment, beginning with lanthanum, barium,

and copper nitrates (Alfa Aesar, Ward Hill, MA, USA) as precursor cation sources. The nitrate salts were dissolved into separate continuously stirred containers of deionized water over 12 h. Nitrate anions were chosen for two reasons: nitrate salts are almost universally soluble, and with the application of heat, form NO_2 which is a strong oxidizer that aids in the combustion of organic material [74]. A 5% weight solution of 80% hydrolyzed polyvinyl alcohol (PVA, Sigma-Aldrich, St. Louis, MO, USA) in deionized water was also prepared by stirring for 24 h, to serve as the entrapping polymer. Aqueous $La(NO_3)_3 \cdot 6H_2O$, $Cu(NO_3)_2 \cdot 2.5H_2O$ and $Ba(NO_3)_2$ solutions were mixed together following the stoichiometry $La_{2-x}Ba_xCuO_4$, and stirred with PVA solution. The PVA and nitrate solutions were combined such that there were 4 times as many positively charged valences from the metal cations as negatively charged OH groups from the PVA, ensuring that there were more cations in solution than could be chemically bonded to functional groups. A few drops of nitric acid (HNO_3) were added to lower the solution's pH to around 0.5 to prevent gelation and precipitation during the reaction.

The stoichiometric precursor solution was heated on a hot plate with continuous stirring (400 °C, 300 RPM) to form a thick aerated gel, which was vacuum dried at 140 °C and -850 mbar for 24 h. The resulting green crisp foam was ground in an agate mortar, heat treated in air at 500 °C for 1 h, ground further to reduce particle size, and finally calcined at 800 °C for 30 minutes to completely remove volatile material. Differential scanning calorimetry and thermogravimetric analyses (DSC/TGA, Netzsch STA 409 CD, Selb, Germany) were performed on both as-synthesized powders and powders preheated at 500 °C for 1 h to study the precursor-to-ceramic powder conversion and phase formation. The experiments were performed at 5 °C/min and 30 °C/min to optimize the calcination temperature. TGA measures mass loss of a heated sample while DSC measures the temperature difference between the sample of interest (the dried polymer-nitrate mixture) and an inert reference (usually alumina). Due to latent heat, DSC will usually show peaks at temperatures where a thermally activated reaction is occurring. Apparent den-

sities of the powder particles were measured using a gas pycnometer (AccuPyc 1330 Pycnometer, Micromeritics, Norcross, GA). Sintered specimens bulk density was measured by the Archimedes' method using deionized water at room temperature (ASTM C373). We measured the phase purity of each batch of calcined powder in an x-ray diffractometer designed for powders (Cu K-α wavelength of 0.15418 nm, Bragg-Brentano configuration, Siemens/Bruker D5000, Billerica, MA, USA).

To reduce particle size and increase specific surface area before consolidation, calcined powders were ball-milled at 100 RPM for 8 h with cylindrical YSZ milling media in 200% ethanol by weight. During the last 15 minutes of milling,1.5% weight PVA and 1% weight ethylene glycol (EG, Fisher Scientific, Hampton, NH, USA) were added as binder to prepare for consolidation of bulk PLD targets. Milling media was removed and the ethanol solution dried in a vacuum oven at 70 °C and -850 mbar for 24 h. The dried binder-coated granules were ground and sieved through 116 µm mesh. The intention of the polymer binder at this stage is to hold the pressed powder grains together until the binder decomposes during the final pellet firing and sintering. There is a trade-off here; ceramics with no binder will crumble long before they are sintered, but most of the volume occupied by binder will remain as a void or pore in the completed target, lowering the density. The weight percentages of 1.5% PVA + 1% EG used here were chosen because they are equivalent to approximately 5% of the volume in the consolidated LBCO pellet, so we were aiming for a "safe" density of 95% in the targets. Higher density targets may have been possible with less binder, but would have required more process engineering in order to ensure cohesion.

Powders were first compacted in a 30 mm diameter cylindrical steel die, uniaxially pressed under ∼100 MPa for 5 minutes. Uniaxially pressed samples were vacuum sealed in a latex membrane and further compacted under ∼275 MPa (40,000 psi) for 5 minutes in a cold isostatic press (CIP, Model CP 360, American Isostatic Press, Columbus, OH, USA). CIP'ed samples were heated in air to 500 °C at a rate of 1 °C/min and held for 1 h

to remove the PVA + EG binders, then heated at 5 °C/min to 1050 °C and sintered for 4 hours. The resultant pellets were in 22 mm diameter x 7 mm thick disks for use as laser deposition targets, and we also made 10 mm diameter disks for diagnostic measurements of density, crystal structure, magnetic properties and electrical resistance. These were nominal sizes after uniaxial pressing, isostatic pressing, and sintering.

3.2 Pulsed laser deposition

Sintered bulk LBCO ceramics, as prepared by steric entrapment, were used as sources for pulsed laser deposition of thin, epitaxial $La_{2-x}Ba_xCuO_4$ films. This section describes some of the general principles of pulsed laser deposition, in order to motivate the specific techniques and growth conditions that were used to make $La_{2-x}Ba_xCuO_4$ films. The later discussion of the measured properties of our LBCO films will rely on the information presented here, especially because many film properties varied significantly with deposition parameters.

PLD was first attempted shortly after the development of the first lasers [75], but it remained relatively obscure until it was demonstrated as a growth technique for the high-temperature superconductor $YBa_2Cu_3O_{7-y}$ [76]. Pulsed laser deposition is a type of physical vapor deposition (PVD), in which energy is injected into a solid material in order to vaporize it, and the vapor is recondensed onto a heated substrate or part in order to form a thin film coating. In PLD, the initial energy injection method is a fast high-energy laser pulse that vaporizes or *ablates* the target material. An illustration of a typical PLD setup, similar to the one used in this study is shown in Fig. 3.4(a). The region of the deposition source affected by the radiation is small, determined by the focusing of the laser and the optical penetration depth, and the energy is transmitted rapidly; this casues a rapid "phase explosion" at the target surface [77] that ejects a plasma at thousands of °C. Fig. 3.4(b) illustrates the rapid plasma formation and deposition, and Fig. 3.4(c) shows

the plasma plume from a typical LBCO growth. Because the plume expansion is driven primarily by the kinetic energy of the irradiated material, it occurs normal to the target surface, regardless of the incident laser angle. The high effective temperature makes PLD a preferred technique for materials with high melting temperatures that are inaccessible with traditional evaporation techniques, or materials with complex multi-element stoichiometries where the explosive evaporation ensures that the deposition rate of different elements matches the target stoichiometry. PLD must be performed in a vacuum chamber, so that the plasma can reach the heated substrate without excessive cooling or interaction, however oxide PLD typically occurs in a small background pressure of O_2 or ozone, in order to fully oxygenate the films. In depth reviews of the PLD technique are available in [78, 79].

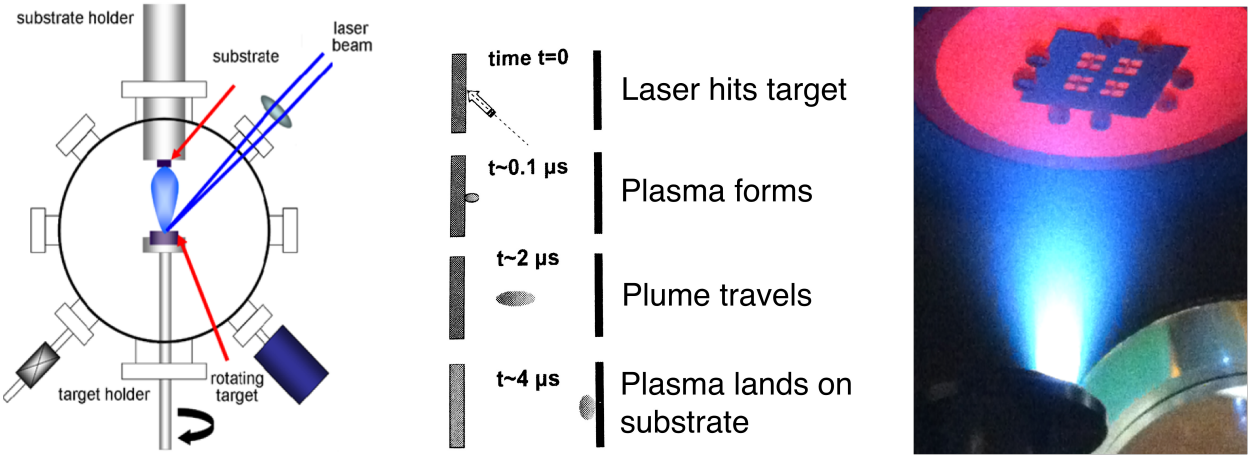

(a) (b) (c)

Figure 3.4: **Pulsed Laser Deposition.** (a) Schematic of a typical vaccum chamber for PLD, from [80]. (b) The plasma generation process and deposition onto substrate, from [79]. (c) Photo of plasma plume during deposition of an LBCO film. In this instance, the film was deposited onto a small substrate mounted onto a heater assembly (red-orange) behind a stainless steel mechanical mask.

Laser deposition is possible with a variety of laser sources, but pulsed UV is advantageous in most applications. Whereas optical wavelengths may require careful attention to absorption lines in the target material, most materials used in oxide PLD absorb UV wavelengths easily. Shorter wavelengths also decrease the effective target-laser interac-

tion volume, thereby increasing energy density. Pulsed lasers have much higher *peak* intensities than continuous-wave lasers, although they have lower *average* intensities. As an example, the laser used in this study was typically ran with $\geq$ 200 mJ per pulse and had 20 ns pulse widths, giving peak intensities $\geq$ 10 megawatts, with average intensities $\leq$ 1 Watt for pulse rates of a few Hz. With a pulsed source the irradiated target area will receive more energy in the $\sim$ 100 ns before it vaporizes, increasing the effective temperature of the plasma. PLD seeks to make the energy injection fast enough that the sample does not have time to pull energy away as heat.

The pulsed UV laser used in to grow LBCO is an *excimer* laser, which is a portmanteau of "excited dimer." In our excimer laser, the excited state responsible for the stimulated emission is a metastable bound state of krypton and fluorine, which decays to a ground state in which the Kr and F atoms unbind and repel. Kr and F do not normally form bonds at equilibrium; the unstable dimerized state is much higher energy than the ground state, so the decay creates a high-energy (UV) photon. The formation of the excimer state mostly occurs by two reactions,

$$\begin{aligned} \mathrm{Kr}^+ + \mathrm{F}^- + (\text{Kr or Ne}) &\rightarrow \mathrm{KrF}^* + (\text{Kr or Ne}), \\ \text{and} \qquad \mathrm{Kr}^* + \mathrm{F}_2 &\rightarrow \mathrm{KrF}^* + \mathrm{F}, \end{aligned} \tag{3.2}$$

where the superscript * indicates an excited state. The third Kr or Ne atom in the first reaction carries away excess energy; because 3-body interactions occur rarely, the excimer laser is pressurized to 3.0-3.7 atm, in order to increase the collision rate. Most of this pressure is neon, only 0.1% of the mixture is fluorine. In both processes the reactants include a state that is already non-equilibrium, Kr^+, F^-, or Kr^*, so the laser's gas mixture must first be pre-ionized. Once formed, the KrF^* state quickly decays into separate Kr and F atoms and emits a UV photon. The excimer laser operates by alternating preionization pulses with high energy (22-31 kV across a large capacitor bank) discharge pulses that

drive the laser output. Only approximately 2% of the energy used by the laser system is emitted as photons, the waste heat generated in the laser gas limits the pulse rate to a few Hz. The laser used to grow LBCO films (Compex 301; Lambda-Physik/Coherent, Santa Clara, CA) emits a UV wavelength of 248 nm at energies between 50 and 1500 mJ/pulse and repetition rates $\leq$ 10 Hz and was typical run at 3 pulses/second and energies near 250 mJ.

The optical path from the excimer laser to the vacuum chamber in which LBCO was grown is shown in Fig. 3.5. Mirrors are quartz with a coating specifically designed for 248 nm. Initial LBCO growths were instead performed at 193 nm wavelength (with corresponding optics), before the switch to 248 nm. 193 nm was shown to incur significantly more energy loss at each mirror, lens, or vacuum window, while 248 nm has near 100% transmission, except perhaps at the vacuum chamber window. A rectangular aperture, set to match the beam shape of our laser was used to block the low-energy fringe at the edge of the beam and ensure homogeneous energy density across the beam width. A focusing lens, placed a few cm from the vacuum window was adjusted such that its focal point would coincide with the top surface of the LBCO targets. This position was calibrated to sub-mm accuracy through extensive imaging of the focused beam. The focused beam was approximately 0.8 mm $\times$ 2.5 mm with an ellipsoid shape. The beam remained stationary during deposition, but the target was moved such that material was efficiently ablated from the entire target surface. This motion was performed using two motors coupled to the target carousel; the target was slowly translated laterally, while quickly rotating along its own axis at $\sim 110^{\circ}$/s, such that the effective beam path resembled a spiral segment with average pulse-to-pulse spacing comparable to the focused beam width. The lateral motion of the target was performed at a nonlinear rate such that more time was spent ablating from the outer edge of the target's surface and less time was spent at the target center, such that the distribution of laser shots per unit area would be roughly constant across the surface. The target-to-substrate distance for our growth was

approximately 65 mm, and the substrate was slowly rotated during deposition in order to improve film uniformity.

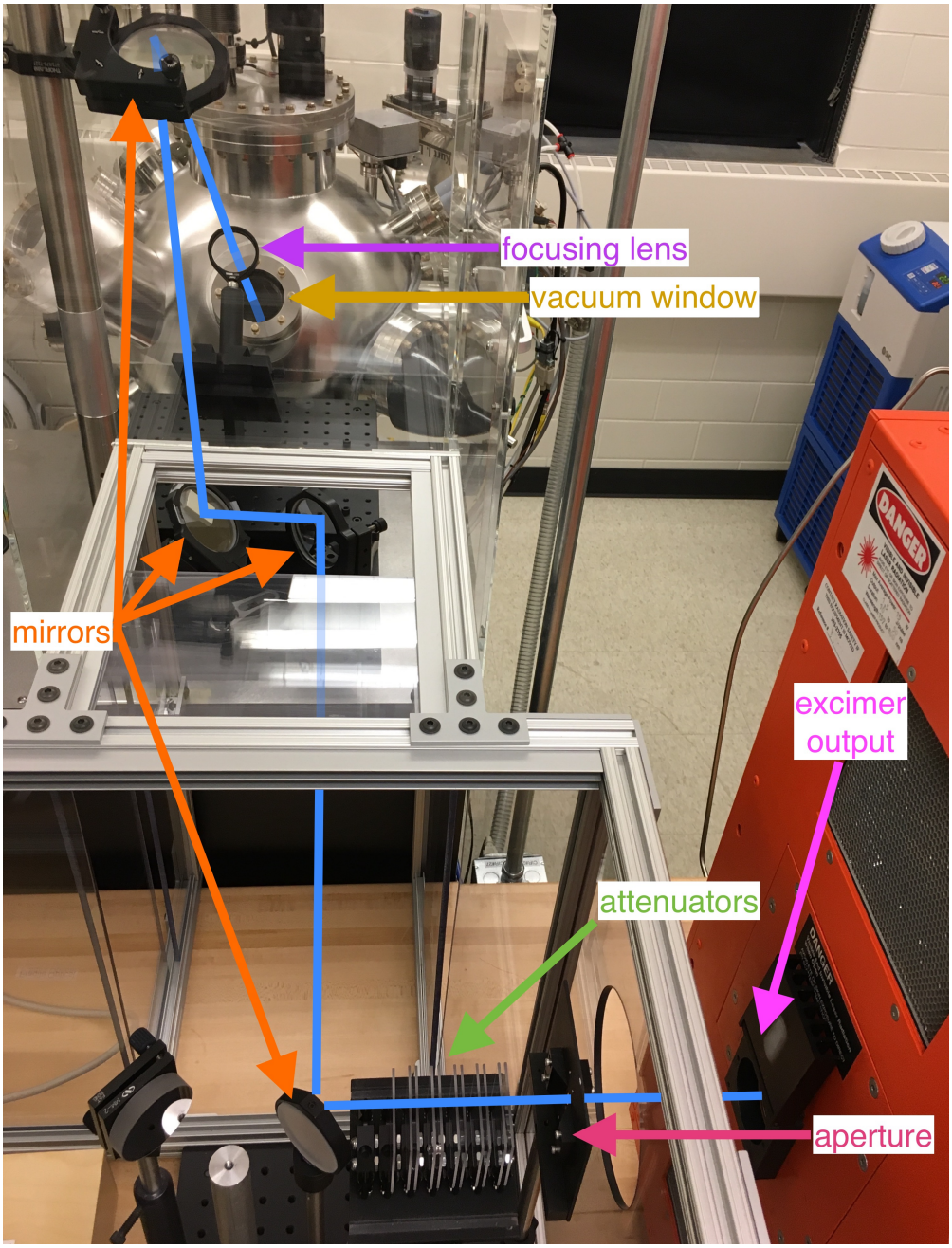

Figure 3.5: **Optical Path from Excimer Laser to PLD Chamber.** Beam path is illustrated in light blue, begins at the laser (large orange instrument) and ends at the target inside the vacuum chamber.

Excimer pulse energy is usually controlled by setting the discharge voltage, and uses

feedback from an internal energy meter in order to reach a user-defined setpoint energy. However, it was observed that pulse-to-pulse variations in the energy are smallest for discharge voltages near 26.5 kV. To maintain optimal pulse consistency, the laser was operated as close as possible to this optimal voltage, and the energy was instead controlled primarily by adding or subtracting quartz plates to an attenuator stack in front of the laser (Fig. 3.5). These $2'' \times 2'' \times 1/8''$ quartz plates (Chemglass, Vineland, NJ) were calibrated and found to attenuate the energy by about 10% per plate, such that N plates would have a transmission factor of 0.9^N. Secondary, fine control of the energy was still performed by adjusting the discharge voltage/internal setpoint at the laser itself. This attenuator setup gave typical laser energy variations of less than $\pm$10mJ between pulses, compared to $\pm$50mJ variation without attenuation.

In reality, the perfect stoichiometric transfer and smooth epitaxial film growth idesired in a PLD process may be difficult to obtain, and may only be possible within a narrow range of deposition parameters. Growth parameters – the most important of which are laser energy, substrate temperature, and background O_2 pressure – can affect both the creation of plasma and the kinetics of adatoms on the substrate surface. In-situ growth monitoring is possible, but difficult. The most popular in-situ diagnostic for PLD is probably relativistic high-energy electron diffraction [81], which measures surface crystallinity in real time, but this was not implemented in our growth system. Alternatively, PLD depositions recipes may be optimized by growing films in a wide range of conditions and studying their properties ex-situ. Favorable material properties, such as sharp superconducting transitions, can then be correlated with specific growth parameters. The laser deposition of $La_{2-x}Ba_xCuO_4$ was optimized in this way and relied on post-growth film characterizations by atomic force microscopy (AFM), x-ray diffraction (XRD), low-temperature resistance, and low-temperature magnetic measurements (the Meissner effect). This style of comprehensive empirical analysis of film properties is especially important for a technique like PLD where it may not be obvious what effect any given change in growth

parameters will have. An attempt is made in the following paragraphs to discuss the "usual" behavior of PLD under different growth conditions, but this only serves to guide the interpretation of later empirical results.

The energy of the laser pulses is perhaps the most important tunable parameter in PLD. The energy density or *fluence* at the target surface determines both the effective temperature of the irradiated material and the energy of the adatoms impinging on the heated substrate. Too low of a laser energy will not fully vaporize the irradiated target material but will instead partially melt the target surface and drive phase separation as it re-cools between each pulse. Depending on the temperature-composition phase diagram of the mixed oxide target at high temperatures, some elements will separate from the remaining solid and vaporize at lower temperatures than others. For example, as shown in Fig. 3.6(a), Y_2BaCuO_5 undergoes incongruent melting, forming a solid Y_2O_3 phase and barium- and copper-rich vapor [82]. At low fluence, this drives yttrium accumulation as confirmed in Fig. 3.6(b). Low-energy PLD tends to deposit non-stoichiometric films. Higher fluence will fully vaporize the target material such that the deposition plume matches the stoichiometry of the target material and further increases in the fluence increase the average particle energy within the plume. High-energy adatoms will more easily diffuse across the substrate surface and form a crystalline phase, but incident particles with energies $\gtrsim 200$ meV will begin *resputtering*, or eroding material that is already deposited in the film. Because the sputtering of a solid varies with atomic mass and bond structure, this is usually non-stoichiometric. The resputtering process in high-energy PLD is usually indicated as surface roughening in the deposited film, however some experiments have detected resputtering directly [83, 84], as discussed in Figs. 3.6(c) and 3.6(d).

A careful distinction must be made between the *total* laser pulse energy, typically expressed in Joules, and the laser energy density, or *fluence*, typically expressed in J/cm^2. For example, if the beam area and pulse energy are increased by the same factor, such

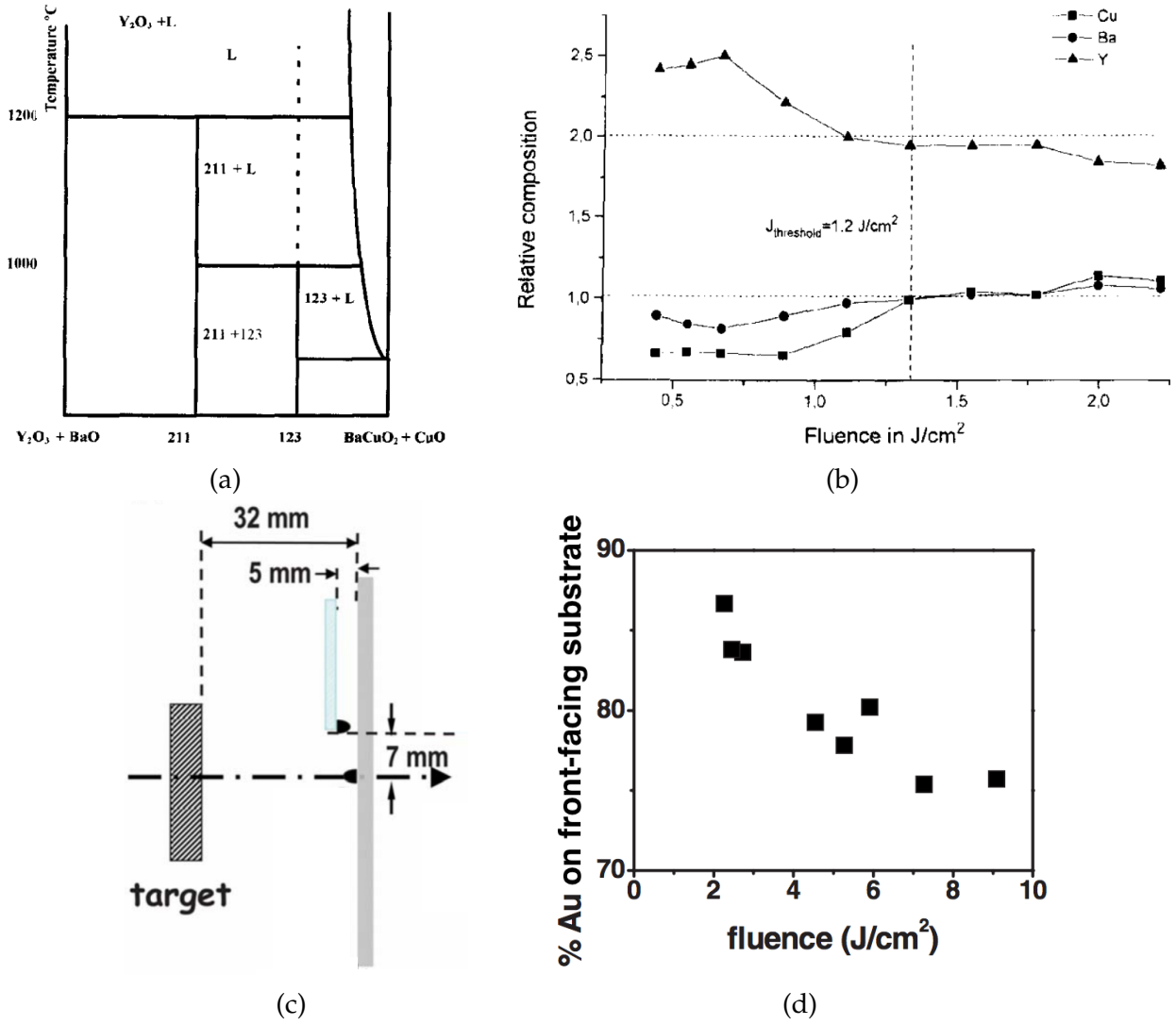

Figure 3.6: **Impact of Laser Fluence in PLD.** (a) High-temperature partial phase diagram of YBCO along the 211-123 line. The 211 phase shows incongruent melting, leaving behind a solid Y_2O_3 phase. The 123 (superconducting) phase also melts incongruently. (b) Stoichiometry of a Y_2BaCuO_5 target surface, measured by energy dispersive x-rays, after ablation. As expected based on the phase diagram, low fluence ablation makes the target Y-rich and presumably causes non-stoichiometry in the deposited film as well. From [82]. (c) Target-substrate geometry for the Au-resputtering experiment in [83]. The front-facing (grey) substrate is typical for PLD, the reverse-facing substrate (light blue) is intended to catch resputtered material from the main substrate. Total amount of gold was measured, by Rutherford backscattering, at the points indicated by black dots. (d) As fluence is increased, less of the total deposited Au remains on the primary substrate and more of it is resputtered onto the rear-facing substrate.

that the fluence remains constant, the microscopic plasma kinetics relevant to PLD (e.g. average energy per adatom) are unchanged, but more material will be ablated, which will change the deposition rate and possibly the growth dynamics occurring on the substrate surface. In our LBCO depositions, the laser spot size was kept constant (0.8×2.5 mm^2) for all growths, ignoring the slight defocusing caused by varying target heights. Even for the highest laser energies used for LBCO, the estimated deposition rate was still less than 1 $\AA$/pulse, or a single atomic layer per pulse, so we do not expect, for example, an energy-dependent crossover from 2D to 3D growth modes. The laser energy probably affected the LBCO growths primarily via the effective plasma temperature and average adatom energy.

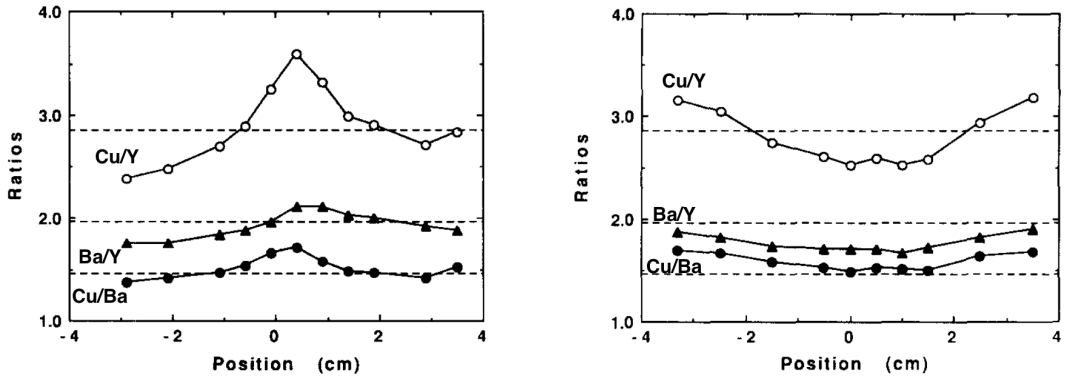

Figure 3.7: **Impact of background O_2 pressure in PLD.** (a) Variation of stoichiometry with lateral position on substrate for deposition of YBCO in vacuum. (b) Spatial stoichiometry variation for YBCO deposition in 200 mTorr. Scattering depends on element and is pressure-dependent. From [85].

The pressure of background O_2 gas (or other gas) during ablation also influences the properties of PLD-grown films. Gas pressure affects film growth primarily through the scattering of energetic particles in the deposition plasma. Film stoichiometry can be pressure-dependent because light elements will scatter more easily from collisions with gas molecules. An example PLD study of YBCO [85], shown in Fig. 3.7, found that films grown in high O_2 pressure tended to be Cu-deficient at the plume center, while the op-

posite was true for films grown near vacuum. Gas scattering also decreases the average energy/particle of ablated material incident on the substrate, so that increasing the pressure of a PLD process is in some ways similar to lowering the laser energy. The amount of O_2 during deposition can also determine the final oxidation level of films that can accommodate oxygen vacancies, such as $YBa_2Cu_3O_{7-y}$, although LBCO rarely deviates from the 214 oxygen stoichiometry. Even at high pressures, PLD is a very directional deposition technique. In LBCO depositions at 300 mTorr for example we found that at angles $\geq 10^\circ$, typical deposition rates were less than half that at the center of the plume.

Compared to the effective temperature of the ablated plasma (1000-3000 °C), the typical substrate temperatures (500-900 °C) for PLD are quite low. By Newton's law of cooling, higher substrate temperatures will keep newly incident adatoms near the hot plasma temperatures for a longer time after each pulse. This can affect formation of high-temperature impurity phases even when the substrate temperature is too low to drive phase separation on its own; $LaCuO_3$ is one such impurity phase that may occur in $La_{2-x}Ba_xCuO_4$ growth. The ability of atoms to "wet" the surface of the film and to fill voids and vacancies is described by Arrhenius behavior (see [79], p. 186), and will cause film topography to be strongly temperature-dependent. The most important effect of substrate temperature may be that at elevated temperatures, elements with high vapor pressure will be less likely to stick to the substrate. This means that, even if the stoichiometry of the deposition plume perfectly matches the target composition, the adhesion of the plasma to the substrate will not necessarily preserve stoichiometry. As pure elements, barium's vapor pressure is much higher than copper's, which is much higher than lanthanum's. This will correlate roughly with the vapor pressures of the same elements in LBCO, and suggests that at elevated growth temperatures, our films will likely be slightly copper-deficient and very barium-deficient. The vapor pressure of oxygen is high, but unimportant because LBCO's oxygen stoichiometry will depend more on post-deposition annealing than deposition kinetics.

The substrates used for $La_{2-x}Ba_xCuO_4$ film growth were $LaAlO_3$ ($\langle 100 \rangle$ orientation, $10 \times 10 \times 0.5$ mm, one side polished, MTI Corporation, Richmond, CA), which was chosen because it is inert, insulating, and very closely lattice matched to LBCO. The unit cell of LBCO is rhombohedral at room temperature, with angles very close to 90°, so it is usually described as a pseudocubic structure with a lattice parameter 3.787 $\mathring{A}$. Bulk LBCO's in-plane lattice parameter at room temperature varies from 3.793 $\mathring{A}$ at $x = 0.06$ to 3.782 $\mathring{A}$ at $x = 0.24$ [86], which is within 0.15% of the $LaAlO_3$ (LAO) lattice parameter. Low-temperature crystallographic studies reveal that neither the lattice parameter of LBCO [31, 87], or LAO [88] change significantly with temperature, so the epitaxial strain should be low at all dopings and temperatures. The slight exception is LBCO's distortion in the low-temperature orthorhombic (LTO) state, in which the in-plane lattice parameter b_0 can be up to 0.8% larger than a_0, at low dopings. In our samples, it isn't known whether this LTO structural phase is modified by epitaxial pinning of the LBCO to the LAO substrate. Because the lattice mismatch of LBCO to LAO is extremely small, we expect our thin film samples to accurately reproduce the same correlated electron physics seen in bulk LBCO.

Before growth, the LAO substrates used for LBCO growth were modified from their as-received state. A large amount of previous work has been done on annealing and surface properties of $LaAlO_3$, primarily as it pertains to $LaAlO_3/SrTiO_3$ heterostructures (see, e.g.[89], although many literature results are in conflict). One such annealing recipe was used in this work in order to smooth the edges of atomic steps, present in the as-received LAO due to slight misalignment of the manufacturer's polishing instrumentation with the LAO lattice. Before use as a substrate for LBCO, each piece of LAO was cleaved (if necessary), then annealed in a tube furnace with flowing oxygen at 950 °C for 8 hours. The unpolished reverse side of annealed substrates were coated, via e-beam evaporation, with 50-100 nm titanium and 100 nm gold. The gold served to homogenize the substrate temperature once the substrates were attached to our growth chamber's heater assembly, and the titanium acted as both an adhesion layer for the gold, and as

an approximate blackbody material to homogenize radiative heating near the substrate. Note that because $LaAlO_3$ is extremely insulating, the temperature at the polished substrate surface during film growth is probably not determined by direct heat conduction from the backside-attached substrate heater, but rather through radiative heating and heat conduction through the background O_2 gas.

3.2.1 Optimal recipe for PLD of LBCO

Initial growths of $La_{2-x}Ba_xCuO_4$films spanned a wide range in growth parameters, in order to optimize the deposition recipe. The experimental results associated with this optimization of film properties are interesting in their own right, and are described in Section 4.2. However, for clarity, the optimum laser deposition recipe used for our "finalized" $La_{2-x}Ba_xCuO_4$ films is summarized here; this describes the parameters used to create most of the samples used in the resistance fluctuation experiments. Before each growth, targets were resurfaced with sandpaper up to 1200-grit ($\sim 15\,\mu m$) and loaded into a vacuum chamber, along with a single-crystal $\langle 100 \rangle$-oriented $LaAlO_3$ substrate affixed with silver paint to a heater assembly. To minimize stray contaminants, cleaning and mounting of the LAO substrates onto the heater plate was performed in a cleanroom.

After initial evacuation of the chamber ($< 5 \times 10^{-7}$ Torr), oxygen gas was circulated to attain a background pressure of 300 mTorr and the substrate was heated to 750 °C. The KrF pulsed excimer laser was first fired at the target, at an energy of 250 mJ/pulse, for 900 pulses with a shutter shielding the substrate from deposition. This "pre-ablation" step was intended to remove any anomalous surface layer from the target after polishing.

Then for 2000-6000 pulses, the continuously rotating heated $LaAlO_3$ substrate was exposed to the deposition plume; at a 3 Hz pulse rate this takes $\leq$ 30 minutes. After deposition, each film underwent an in-situ three-stage annealing process: 1) 15 minutes at 750 °C in 300 mTorr O_2 (growth conditions) to allow diffusion and improve homogeneity,

2) 15 minutes at 540 °C in 740 Torr O_2 near a structural transition of $LaAlO_3$, and 3) 30 minutes at 450 °C in 740 Torr O_2 to ensure stoichiometric oxygen concentration. The films discussed below were 50-100 nm thick for general studies of film properties and 25-50 nm thick for resistance noise measurements.

3.3 Film characterization techniques

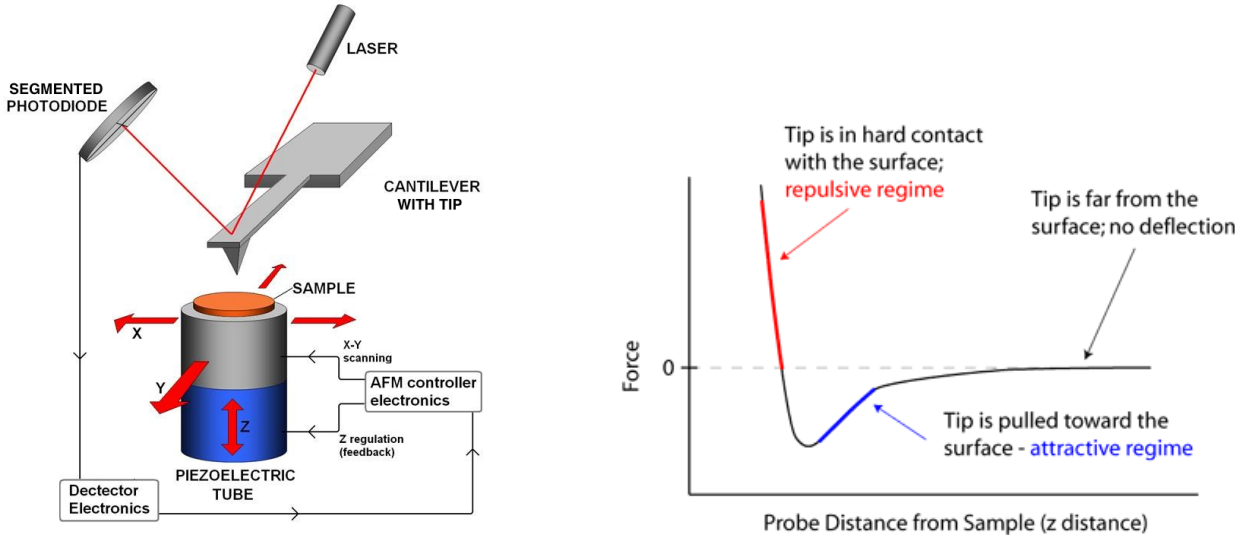

(a) (b)

Figure 3.8: **Atomic force microscopy.** (a) Schematic of a typical atomic force microscope, from [90]. (b) Generic curve describing the force on the tip from the sample, as a function of tip-sample separation, from [91]. Van der Waals attraction gives way to repulsion at short distances.

Structural characteristics of deposited $La_{2-x}Ba_xCuO_4$ films were determined by atomic force microscopy (AFM) and x-ray diffraction (XRD). AFM provides topographic data, or images of a sample's surface height in small scan areas, with sub-nm height resolution and few-nm lateral resolution. This makes it an ideal technique to study the morphology of thin films, and for PLD in particular, it can provide some retrospective insight into what kinetics may have occurred during growth. The force microscope used in this work (Cypher S, Oxford Instruments Asylum Research, Santa Barbara, CA) was similar to the

illustration in Fig. 3.8(a). A sharp silicon tip on the end of a cantilever (Tap300Al-G, BudgetSensors, Sofia, Bulgaria), which is fabricated by micromechanical methods and has typical tip radius ~ 10 nm, is positioned over the sample surface. Imaging is performed by rastering the sample in two dimensions, using a piezoelectric scanner. As the sample surface height changes, the tip experiences a force, mostly due to sample-independent Van der Waals forces, as described by Fig. 3.8(b). This force deflects the cantilever according to Hooke's law, and the cantilever deflection is read out using a laser reflected from the cantilever head into a split photodiode.

In practice, the sample-tip separation is not allowed to vary, since this would likely crash and dull the tip. Instead, feedback electronics connect the photodiode to a height-adjusting piezo and are used to maintain the tip at a constant height above the sample, even as its topography varies. Additional spatial resolution can be obtained by operating the AFM with a slightly modified protocol known as *tapping mode*. In tapping mode, an additional piezoelectric attached to the base of the cantilever is used to oscillate the tip close to its resonance frequency, near 300 kHz for the tips used here. The effect of tip-sample interaction is to then modify the cantilever's resonance, which causes a change in oscillation amplitude as detected by the photodiode. The benefits of tapping mode are twofold: firstly, it only brings the tip close to the sample for brief moments during the oscillation period, reducing the likelihood of tip damage compared with constant-contact AFM. Secondly, the use of an AC rather than DC signal allows the feedback electronics and topographic read out to use of a *lock-in* amplifier, a highly frequency- and phase-selective AC amplifier that excels at rejecting noise. For LBCO films, 5 µm wide tapping-mode AFM images were typically recorded in at least two well-separated locations on each wafer, in order to ensure the underlying film texture was imaged rather than anomalous post-growth contamination.

Unlike the local real-space data provided by AFM, x-ray diffraction provides sample-averaged reciprocal-space structural data, describing to sub-$\mathring{A}$ precision the spacing be-

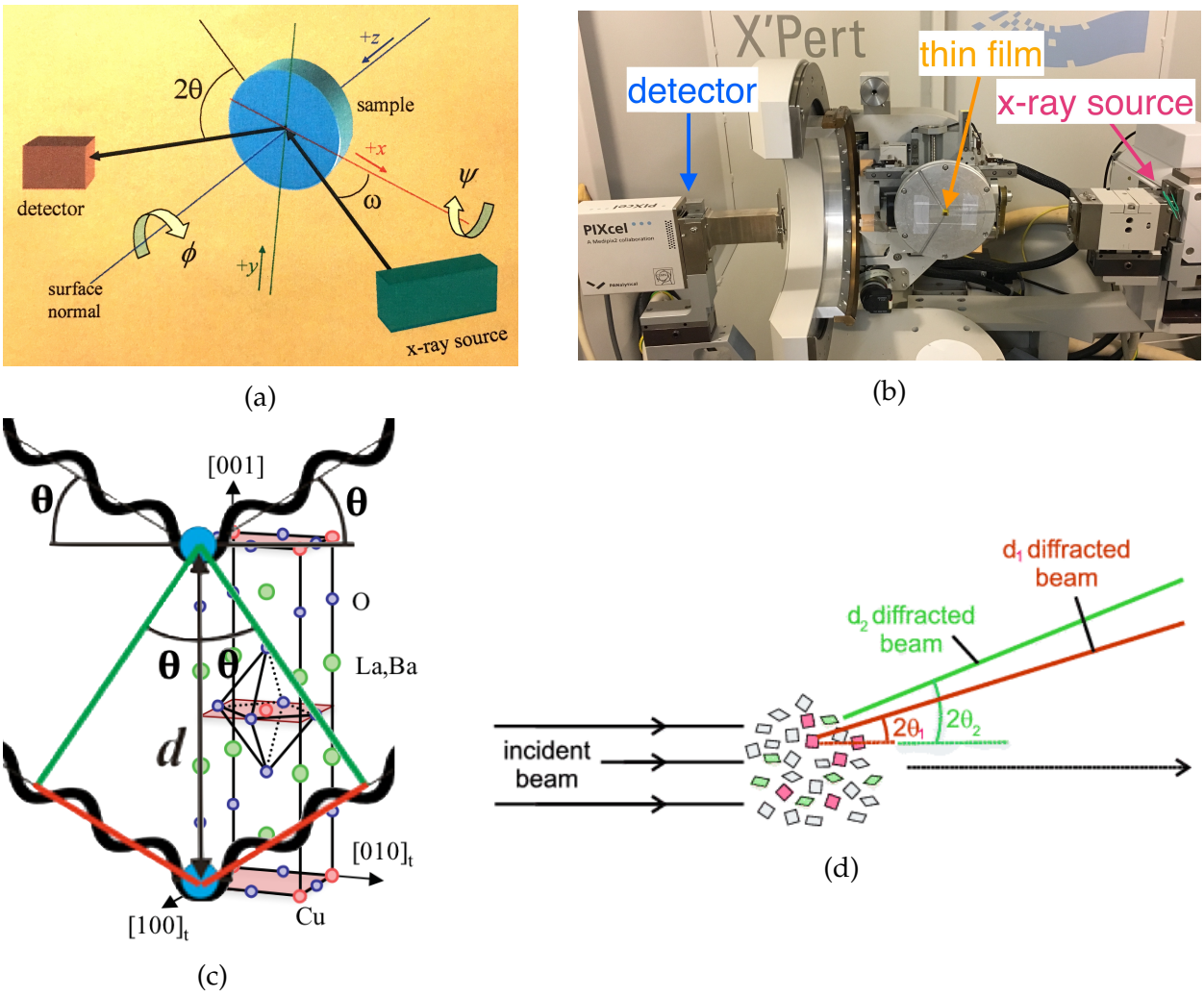

Figure 3.9: **X-ray diffraction.** (a) Schematic of the x-ray diffractometer used to study LBCO thin films. Possible scan directions are ω, ϕ, ψ, and the coupled $2\theta - \omega$ direction. (b) Photo of diffractometer with a 5 mm cuprate film. (c) Diffraction from LBCO's CuO_2 planes. The beam illustrated here diffracts from planes parallel to the c-axis and has a path length difference of 4 wavelengths, corresponding to the (0 0 4) peak. In LBCO, destructive interference from the CuO_2 plane in the center of the unit cell forbids odd-numbered c-axis reflections. Composite image with elements from [31, 92] (d) Powder diffraction, diagram from [93]. When the Bragg condition is satisfied, the incident beam diffracts from some of the randomly oriented grains in a powder sample. By scanning $2\theta - \omega$, a powder diffractometer detects all such Bragg peaks present in a polycrystalline material, and can be used for structure or material identification.

tween atomic layers in a material. For grown films, this provides useful confirmation that the film material has the correct lattice symmetry and dimensions, and therefore the correct phase. XRD experiments relevant to this study are depicted in Fig. 3.9. For two

atomic planes a distance d apart, e.g. the two CuO_2 planes at the top and bottom of LBCO's unit cell, a parallel x-ray beam incident at angle θ to the plane will have a path length difference $2d\sin(\theta)$ as it reflects from the two planes. For constructive interference, this path length difference must be an integer multiple of the wavelength λ, giving the Bragg condition for diffraction,

$$2d\sin(\theta) = n\lambda. \tag{3.3}$$

As angles are varied in an x-ray experiment, strong diffracted intensities will occur at some characteristic angles θ that in turn give information on the interplanar spacing d for known n and λ. The diffraction index n may not be known a priori, but can be guessed by comparisons to databases of known materials with indexed XRD peaks. Some terminology common to XRD experiments must be defined here; the angle of the incident beam with the sample surface is usually referred to as ω, the angle of the reflected beam (or the detector's line of sight) with the sample is θ. Equivalently, the angle between the incident and diffracted beam is 2θ. In general θ and ω may be varied independently, but here they will usually be varied in a coupled way such that $\omega = (1/2) * (2\theta) + \text{offset}$; this is commonly referred to as a "$2\theta - \omega$" scan.

XRD will be applied to LBCO in a couple of different ways. First consider a material that is crystalline on the atomic scale, but has a granular microstructure, such that any x-ray beam incident on the sample sees grains of all possible orientations. If θ and ω satisfy a Bragg condition for the material, then at least *some* of the grains will be at the correct orientation to diffract. Therefore, a $2\theta - \omega$ scan will detect diffraction peaks associated with every possible Miller index of the material's lattice. The locations and relative intensities of the diffraction peaks serve as a powerful fingerprint to identify the material. Powder diffraction was used to study phase formation in the LBCO powders and targets synthesized by steric entrapment as described in Section 3.1. The polycrystalline PLD targets have small, randomly oriented grains, and for XRD purposes will behave similarly

to a true powder.

In a single crystal or epitaxial film, detection of a diffraction peak requires both the satisfaction of equation 3.3, and the correct orientation of the sample. The scattering vector, which is the k-space difference between the incident and reflected x-ray beam, must be parallel to the normal vector $[hkl]$ of the diffracting planes. Most XRD experiments on our $La_{2-x}Ba_xCuO_4$ films will occur with the scattering vector normal to the film and epitaxially oriented CuO_2 planes, such that scans in the $2\theta - \omega$ direction probe the c-axis lattice spacings of the material. Note that substrate peaks associated with $LaAlO_3$ will also be detected, but because the substrate and film have very different c-axis lattice spacings, $\sim$3.78 $\mathring{A}$ and $\sim$13.25 $\mathring{A}$, respectively, the peaks do not overlap. Alignment to the maximum intensity near the LAO (002) peak was used before all LBCO film XRD experiments in order to account for slight misalignments due to variations in sample mounting or substrate miscut.

For typical LBCO samples, two types of $2\theta - \omega$ scans were recorded in a diffractometer with one-dimensional CCD detector (X'Pert + PIXcel^{1D}, Philips/PANalytical, Almelo, Netherlands). Fast survey scans over a range $2\theta = 10^\circ$ to 100° were performed to confirm the presence of c-axis LBCO peaks, and to look for unintentional off-axis LBCO peaks or impurity peaks; every pixel of the detector was used in order to improve counts and lower the detection threshold for impurity phases. High-resolution scans were performed by scanning LBCO (0 0 n) peaks with $n = 2, 4, ...10$ using a $(1/32)^\circ$ divergence slit on the x-ray source and only the central detector pixel, in order to measure an accurate peak shape. Peaks were fit using the JADE x-ray analysis software, to Pearson-VII peak shapes.

At grazing angles $2\theta \leq 3^\circ$, an x-ray beam will not experience diffraction, but will instead reflect from the electron density in the film. As described in Fig. 3.10, reflecting beams from the top and bottom film surfaces may interfere in a manner that depends on film thickness, density, and roughness. This x-ray reflectivity (XRR) technique is an x-ray equivalent to optical ellipsometry, but is easier to apply to non-standard materials

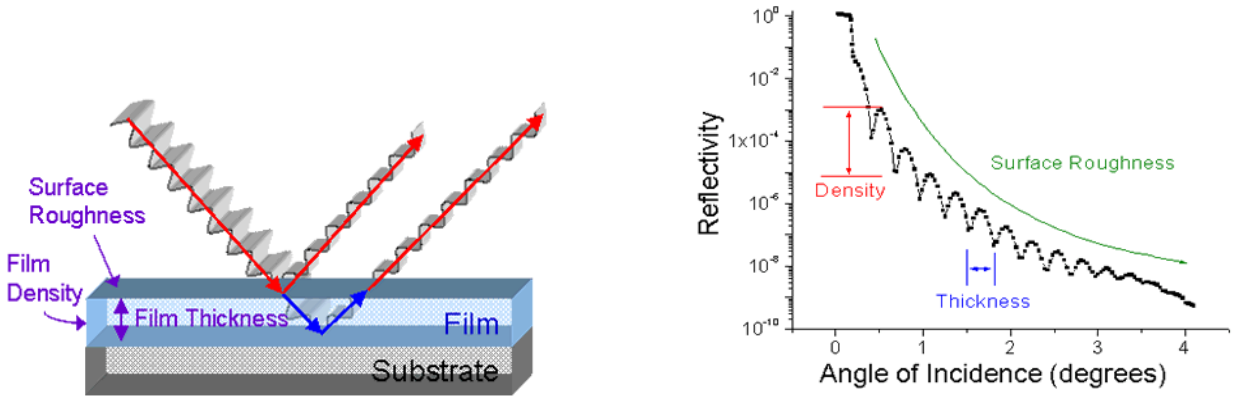

(a) (b)

Figure 3.10: **X-ray reflectivity measurements.** Images from [94]. (a) At shallow angles of incidence, an x-ray beam does not diffract, but instead reflects from both the top film surface and the film-substrate interface. As angle is varied, these two reflections alternate between constructive and destructive interference, with a period that depends on film thickness. (b) Example XRR scan from a thin film of polymer.

(like LBCO) in which the optical index of refraction is unknown. Most importantly, the period $\Delta\theta$ of the interference fringes are dependent solely on the film thickness t, and are related by $t \approx \lambda/(2\Delta\theta)$, with a small-angle approximation. XRR was used primarily as a non-destructive method to measure the thickness of LBCO films.

The flow-through cryostat (STVP-100 Optical Cryostat, Janis Research Company, Woburn, MA) used for most LBCO film experiments, including noise measurements, is described in Fig. 3.11. Liquid helium, which has a boiling point of 4.2 K at ambient pressure, flows through a transfer line into the sample space at the bottom of a small cryostat. The entire flow path is vacuum insulated until helium exits to a recovery system at the top of the cryostat. A small probe connects room-temperature electronics at the top of the cryostat to the low-temperature sample stage. A needle valve on the transfer line controls the cryogen's flow rate and hence the cooling power. At low flow rates the helium is already in the vapor phase and is warmer than 4.2 K by the time it reaches the sample space. A heater/vaporizer at the base of the cryostat, where the helium enters, warms the vapor to a temperature set by a temperature controller (LS340, Lakeshore Cryotronics, West-

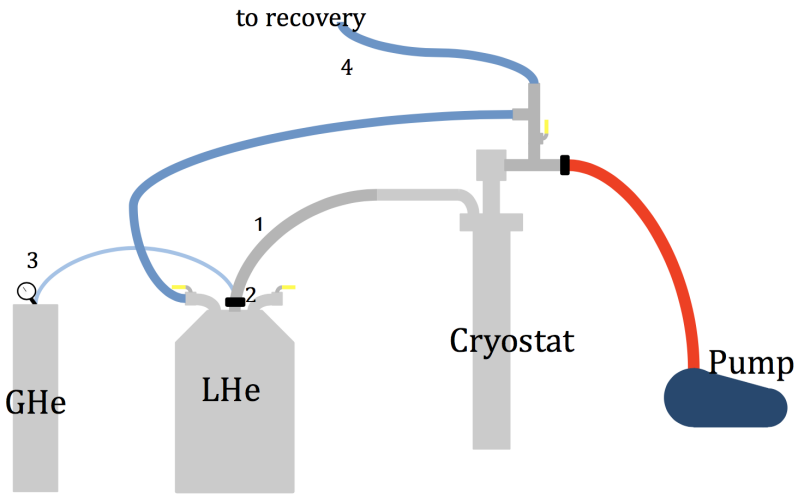

(a)

(b)

Figure 3.11: **Flow-through cryogenic system.** (a) Schematic of the flow-through cryostat system used for 2-coil measurements of the Meissner effect, resistance fluctuation experiments, and some resistance-vs-temperature experiments. Gaseous helium is used to pressurize the vapor space at the top of a liquid helium dear, which forces the 4.2 K cryogen through a transfer line into the vacuum-insulated cryostat. Flow rate is controlled by a needle valve on the transfer line. Temperature is controlled by a 25 W heater that warms vapor entering the bottom of the sample space, and temperature is measured by a sensor close to the sample. (b) Photograph of the same system, configured for noise measurement. Pump and gaseous He cylinder are out of view to the left, and the data acquisition computer is out of view to the right.

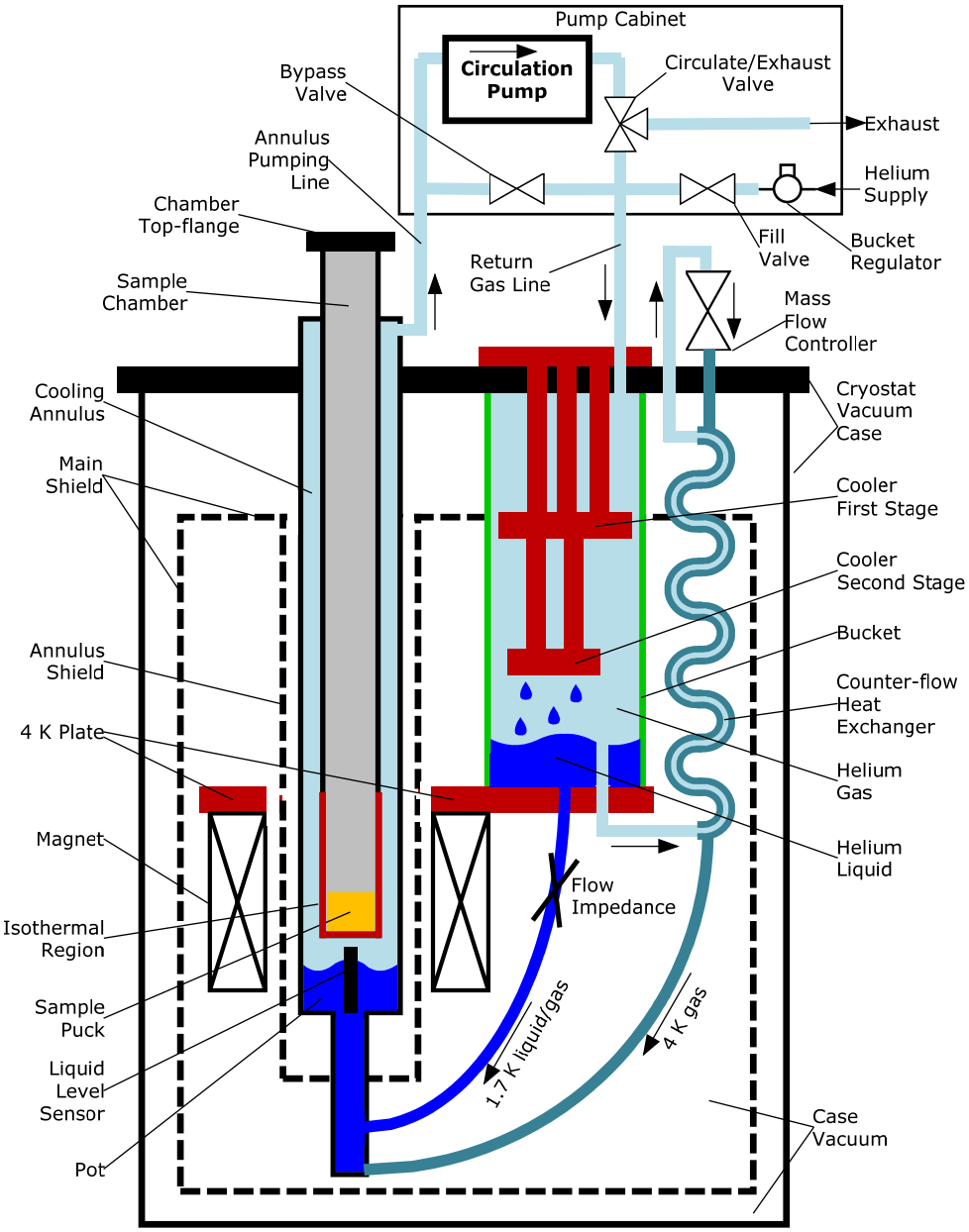

Figure 3.12: **Schematic of the cryogenic "Physical Property Measurement System" (PPMS).** All Hall effect experiments, and many of the LBCO resistance-vs-temperature experiments, were performed in this system. The PPMS uses a pulse-tube cryocooler and can obtain magnetic fields of ± 9 T. The cryogenic system used for vibrating SQUID magnetometry (VSM) is made by the same manufacturer and is similar to what is depicted here, with the addition of a longitudinally oscillating sample rod.

erville, OH). The temperature controller use PID (proportional-integral-derivative) feedback to set the heater output power appropriately, relative to the measured temperature

at the cryogen inlet. A second temperature sensor (DT-670A1-CU SiO_2 diode, Lakeshore Cryotronics, Westerville, OH), mounted on the end of the experimental probe, close to the sample, measures the actual sample temperature, which is usually 0.2 K to 10 K warmer than the cryostat's vaporizer temperature, depending on flow rate.

For the LBCO resistance fluctuation experiment, a flow-through system allows convenient access to variable temperatures above 4 K, but may also cause additional noise if an unstable or time-dependent helium flow couples to the voltage across a measured LBCO device. Because LBCO's resistivity is temperature dependent, especially near T_c, large temperature fluctuations may cause resistance fluctuations that could be mistaken for noise associated with the stripe state. Varying temperature gradients across the sample could also cause time-dependent thermoelectric voltages that could resemble finite-current resistance fluctuations. Therefore, some precautions were implemented to avoid temperature fluctuations and acoustic noise, which could cause temperature fluctuations by coupling to the flowing helium gas. Vibration isolation, in the form of styrofoam and rubber sheets, was placed under the electronics racks, the flow-through cryostat itself, and the liquid helium storage dewar. A styrofoam choke, located at the point where helium exhausted to the recovery system, served as a low-pass filter for helium flow variations, preventing Taconis oscillations [95] and other fast variations. The PID parameters at the temperature controller were mostly "proportional," with a slight integral coefficient, and zero derivative coefficient. This significantly slowed the response of the vaporizer's feedback loop, but prevented sudden variations in heater power. Heater output was limited to less than 5 watts, and was allowed to equilibrate at each measurement temperature for ≥ 1 hour before applying current and recording noise data. Measuring low-frequency noise with good statistics at multiple currents up to 500 µA was a slow data acquisition process that could take 2-5 hours at a single temperature, so long-term temperature stability was critical for these experiments.

Additional cryogenic systems with high-field superconducting electromagnets were

required for the field-dependent magnetometry performed in a vibrating SQUID magnetometer (VSM) and for the Hall effect experiments performed in LBCO thin films. A schematic of the cryogenic "Physical Property Measurement System," or PPMS, (Quantum Design Inc., San Diego, CA) used for Hall-effect experiments is shown in Fig. 3.12; the VSM cryostat is functionally similar. The computer-controlled cryogenics are based on closed-cycle pulse tube refrigeration of helium and can obtain temperatures below 2 K and bipolar magnetic fields up to ± 9 T. This type of system may be prone to trapped flux in the superconducting magnet, and temperature oscillations at the helium-compressor's pulse frequency, so it was deemed inappropriate for resistance noise measurements.

Temperature-dependent resistance measurements on LBCO films were performed by two methods. Early measurements were performed by driving a small AC current ($\sim 10\,\mu$A, 5 Hz typ.) through the film and measuring AC voltage with a lock-in amplifier (7265 Dual-Phase DSP Lock-in Amplifier, Signal Recovery/Ametek, Oak Ridge, TN). Early attempts to contact the LBCO film directly by indium pressing produced high-resistance capacitive contacts, believed to be caused by a non-conducting oxide layer at the film's surface. Additionally, resistance measurements on unpatterned films can provide anomalous results if the films are inhomogeneous, as our early LBCO films grown from low-quality targets were. Therefore, even for simple $R(T)$ characterizations of thin-film LBCO, transport geometries were explicitly defined through deposition of metal contacts; this deposition was similar to the microwire fabrication process described in Section 3.4, but used simple mechanical masks in lieu of photolithography. Later characterizations of $R(T)$ were instead performed in the PPMS system, using the built-in commercial "resistivity" module, which is based on a DC Wheatstone bridge circuit, and can measure three samples simultaneously. Resistance measurements were always performed after AFM, XRD, and magnetic characterizations were complete, because of the semi-destructive nature of depositing contacts.

The Meissner effect in LBCO powders, targets, and films was studied by both VSM

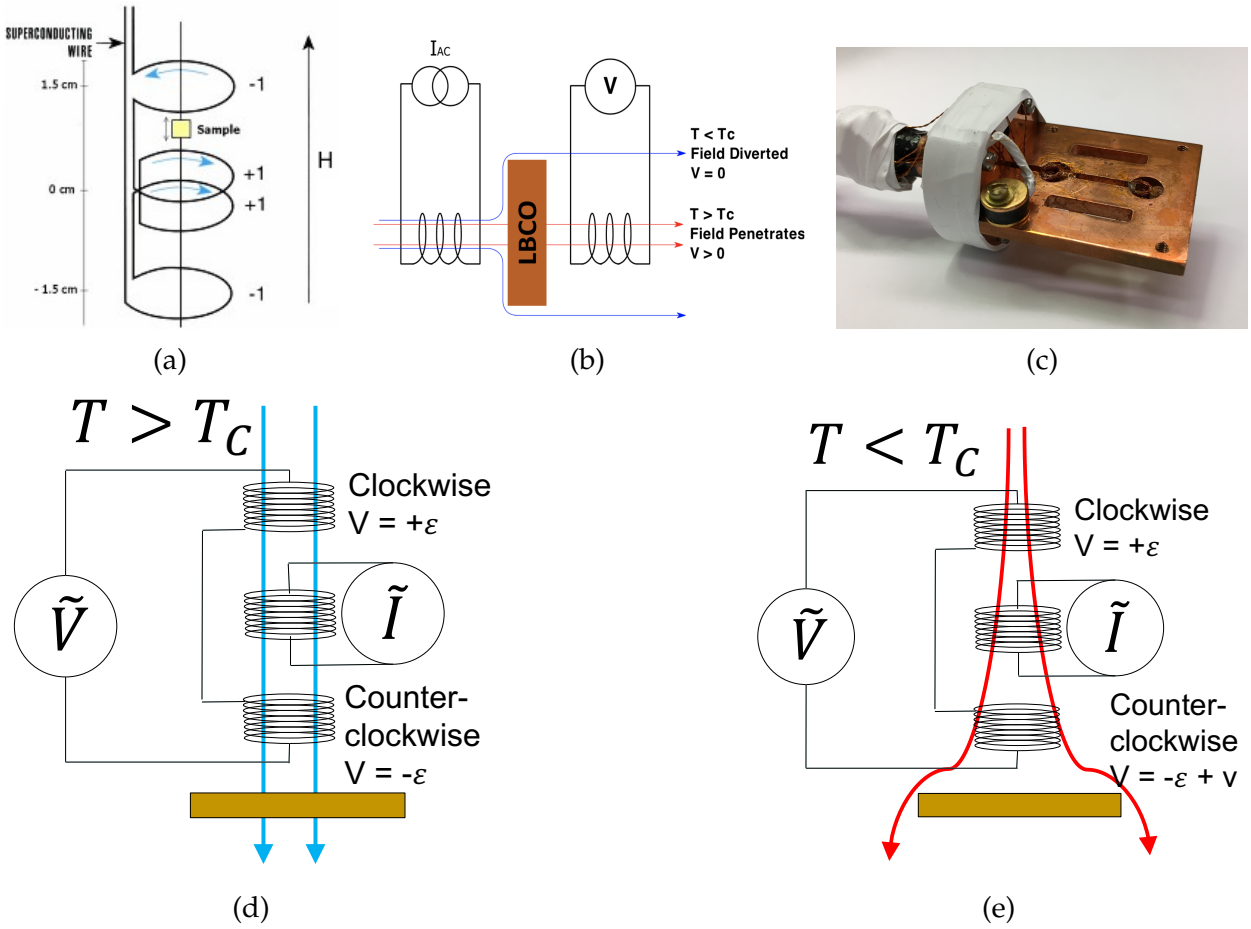

Figure 3.13: **Coil configurations used for magnetometry of the Meissner effect in LBCO.** (a) Diagram of pickup coil used for VSM, from [96]. The second-order gradiometer coil is sensitive to the oscillating magnetic sample, and inductively coupled to an RF-SQUID that functions as a sensitive flux-to-voltage transducer. (b) Diagram of the simplest "2-coil" or inductive technique for measuring the Meissner effect. A high frequency current in one coil generates AC magnetic field that is detected by a second coil on the opposite side of the sample. Above T_c, field penetrates the sample and the transformer outputs finite voltage; below T_c field is deflected and $V = 0$. (c) Photo of the copper 2-coil sample stage used for LBCO; both of the circular holes can hold a coil, allowing dual sample measurement. In the "coil sandwich" configuration of Fig (b), the stage houses two driving coils and an additional plate with pickup coils is mounted on top of the samples. In the counterwound gradiometer configuration of Fig (d)-(e), the stage houses the 3-mm-wide combined gradiometer/driving coil assembly, and no top plate is necessary. (d) Counter-wound coil geometry. In the normal state, field generated by the driving coil enters the two halves of the pickup gradiometer coil symmetrically, such that each gradiometer half has an equal and opposite induced voltage, and the total AC voltage is zero. (e) In the superconducting state, magnetic field is deflected out of the gradiometer half closest to the sample, and the asymmetric coupling produces a finite voltage.

(vibrating SQUID/sample magnetometry) and the "2-coil" inductive technique, as described by Fig. 3.13. The VSM allows measurement in a controllable DC magnetic field and explicitly reports the magnetic dipole moment of the sample. However, this sensitivity also makes it susceptible to background signals from the sample stage, sample-mounting adhesive, and any cross-contamination from previous samples. The sample space is also only $\sim$ 2 mm-wide, posing a difficulty for large samples, such as full-size PLD targets or 10 mm-wide films designated for later fabrication into microwires.

The inductive 2-coil technique is performed either with a film sample between two halves of a transformer, or with a monolithic counterwound gradiometer/driving coil assembly on one side of the sample. It is less precise than VSM as a general magnetic probe, but excels at measuring the Meissner effect's screening of magnetic fields. By Faraday's law, the induced voltage in the pickup coil will scale linearly with both frequency and field magnitude, so the 2-coil experiment is driven by lock-in electronics at high current and frequency (5 mA, 121,111 Hz) in order to maximize the signal. Lock-in detected induced voltages are typically $\leq 300\,\mu V$ and phase shifted by approximately 90 $^\circ$ from the driving current signal. In a 2-coil experiment, superconductivity in a small volume fraction of the sample may not be sufficient to deflect field away from the pickup coil, a measurable pickup coil signal occurs only for relatively strong, homogeneous superconductivity. The VSM may be a better probe of weak superconductivity, but sharp 2-coil transitions are probably a better indication of overall sample quality in homogeneously superconducting samples. In general, the two techniques are fairly equivalent, and magnetic moment can even be numerically extracted from the 2-coil signal if the sample and coil geometry is symmetric and known with sufficient precision [97]. In the results below, however, Meissner signals measured by 2-coil will be reported as unconverted voltages.

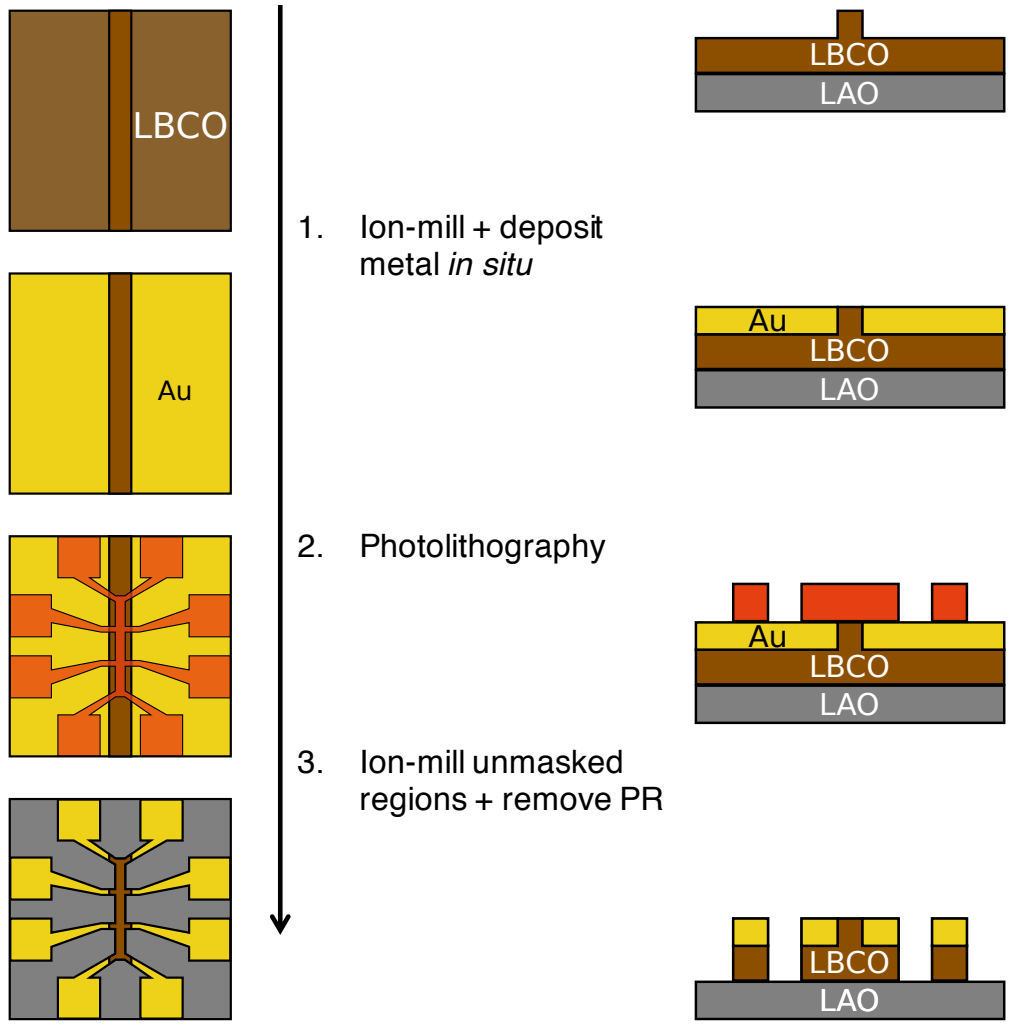

Figure 3.14: **Microfabrication process for microscopic $La_{2-x}Ba_xCuO_4$ wires.** In situ etching before gold deposition makes transparent low-resistance contacts. Wires are defined by ion milling with patterned photoresist acting as an etch mask, then resist is stripped from the finished device. Not shown: a 2-5 nm sticking layer of Cr or Ti between the LBCO and Au. Left column is top-down view of sample, right is side view.

3.4 Microfabrication of LBCO wires

For resistance fluctuation measurements, PLD-grown LBCO films were etched into microscopic wires with metallic contacts by the process described in Fig. 3.14. Either mechanical masking, or image-reversal photolithography was used to block the future location of the microwire, while a metallic layer was deposited on the rest of the chip. To ensure low contact resistance, this deposition of contacts was preceded by an in situ

ion-milling (dry-etching) step to etch away 1-5 nm of film material, removing any possible "dead layer" at the surface of the as-grown film. Without breaking vacuum, 2-5 nm of a chromium or titanium sticking layer was evaporated onto the sample, followed by 30-200 nm of gold. This initial etch/deposition step was performed either in a thermal evaporation system, or an e-beam evaporation system, depending on availability. Typical contact resistances in finished devices were estimated to be $\leq 0.1\Omega$.

After metallization, the geometry of the microscopic LBCO wires was defined using a positive photolithography process (AZ 5214 E Photoresist, Microchemicals, Ulm Germany). A double layer of resist was spin coated to a thickness of approximately 3 µm, UV-exposed in hard contact mode in a manual mask aligner (MJB4, Suss Microtec, Garching, Germany) with Hg-based light source, and then developed for $\sim$ 30 s to remove the exposed photoresist and briefly rinsed in deionized water. A metal-ion free developer was used to avoid unintentional additional of dopants to the LBCO surface. Typical microwire dimensions were 2-4 µm wide and 10-15 µm long. Note that many of the sample features in our devices approach the minimum $\sim$ 1 µm resolution possible for "standard" photolithography with light sources near 350 nm, so a large amount of process engineering and optimization of the lithographic process was necessary. At these length scales, some degree of rounding at the corners of the device were unavoidable.

Once defined, the geometry of the patterned photoresist was transferred to the Au/LBCO layers by *ion-milling*, a dry-etching process, using the photoresist as an etch mask. In an ion mill, a vacuum chamber is filled slight pressure of argon gas (10^{-4} torr typ.), and electron bombardment is used to ionize the argon, forming a sparse plasma. A potential applied between two grids (usually carbon) with carefully aligned, evenly spaced apertures, accelerates the Ar^+ ions, which pass through the grid and fly towards the sample at high energy. An additional "neutralizer" filament after the second grid adds electrons back to the fast-moving positive Ar ions, such that the beam hitting the sample is uncharged. Incident argon atoms with energies of a few hundred eV bombard

the LBCO sample, transferring momentum to and sputtering away the film material. Ion-milling was used for this fabrication because its anisotropic removal of material is good for small resist features, it removes hard material like ceramics efficiently, and because no selective wet-etching process was known for LBCO on LAO.

A 350 V, 65 mA ion beam with 47 V accelerating voltage was used to etch the LBCO microwire samples discussed below. To confirm that the entire film had been etched through, resistance of the etched surface was measured, and the etching process repeated until this surface resistance was immeasurably high, as expected for bare LAO. It should be noted that although ion-milling is less damaging than alternative techniques, there remains a chance that it will damage the microwire regions either through heat or structural disorder, rendering it non-conductive, or not representative of bulk LBCO. This was avoided here by only exposing the sample to the etching beam for 30 s intervals, with 30 s recovery periods, while the sample stage was actively cooled with liquid nitrogen. Stage cooling during etching also prevented ion-beam induced cross-linking of the photoresist, making it easier to remove after the ion-mill process. However, milled photoresist was still difficult to remove with solvents alone, and it was usually necessary to use weak oxygen plasma etching (CS-1701 March/Nordson, Concord, CA) in order to descum the sample before measurement.

Sample yields were not 100%. Nearly all of the optimally deposited LBCO films superconduct *before* fabrication, but it was sometimes observed that microfabricated wires were not superconducting, or had resistance drops at T_c but not all the way to $R = 0$. It is not known whether this is due to initial sample inhomogeneity, ion-beam damage, or some other form of damage due to environmental exposure.

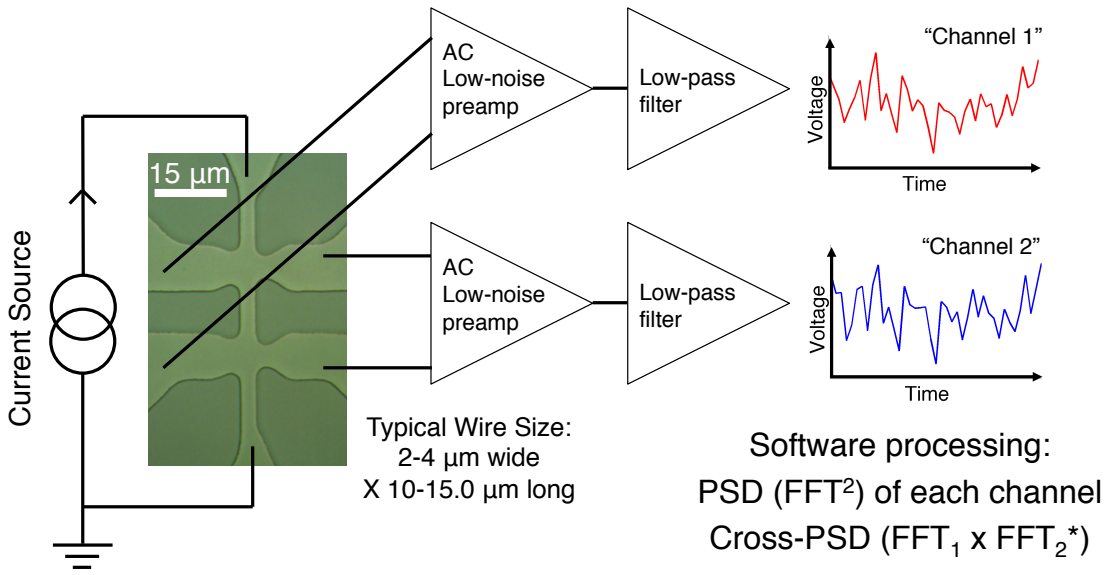

Figure 3.15: **Block diagram for noise measurement with dual voltage channels.** Each single-channel voltage time trace shows noise from resistance fluctuations, Johnson noise in the leads, low-frequency amplifier noise, and any other sources. Cross-correlation between two channels rejects amplifier noise and Johnson noise from the leads.

3.5 Electronics for low-frequency noise

A block diagram description of the typical resistance fluctuation measurement is shown in Fig. 3.15. Constant direct current flows the microfabricated LBCO wire, while two AC-coupled amplifier channels measure the voltage fluctuations along the same length of wire. The outputs of these low-noise preamps are passed through anti-aliasing filters and recorded by a data acquisition computer at finite sampling frequency. The raw data output of the experiment is voltage as a function of discrete time for multiple channels. AC-coupled amplifiers ignore the large average DC voltage across the wire caused by the DC bias current and Ohm's law, and are only sensitive to AC voltage *fluctuations*. This configuration allows high gains to be used for the noise measurement, regardless of the DC resistivity of the wire.

If resistance fluctuations are the sole source of voltage noise in the system, then the two amplifier channels will report the same signal. In reality, the output voltage of each

channel will also be influenced by the Johnson-Nyquist noise in the voltage leads (most of which is from the unmetallized LBCO region), fluctuating thermoelectric voltages at the contacts, and the voltage noise of the amplifier itself. The redundant voltage channel outputs can be cross-correlated by computing the product of the Fourier transform of channel one, times the conjugate Fourier transform of channel two. For two unrelated noise sources, such as two noisy amplifiers, the complex Fourier amplitudes of each channel will have random relative phases, such that when averaged over repeated measurements, the product is close to zero. In contrast, in-phase noise present on both channels will add coherently and average to a finite value. Cross-correlation of the two voltage channels should preserve only noise from the 4-terminal LBCO wire itself (and potentially other shared noise sources).

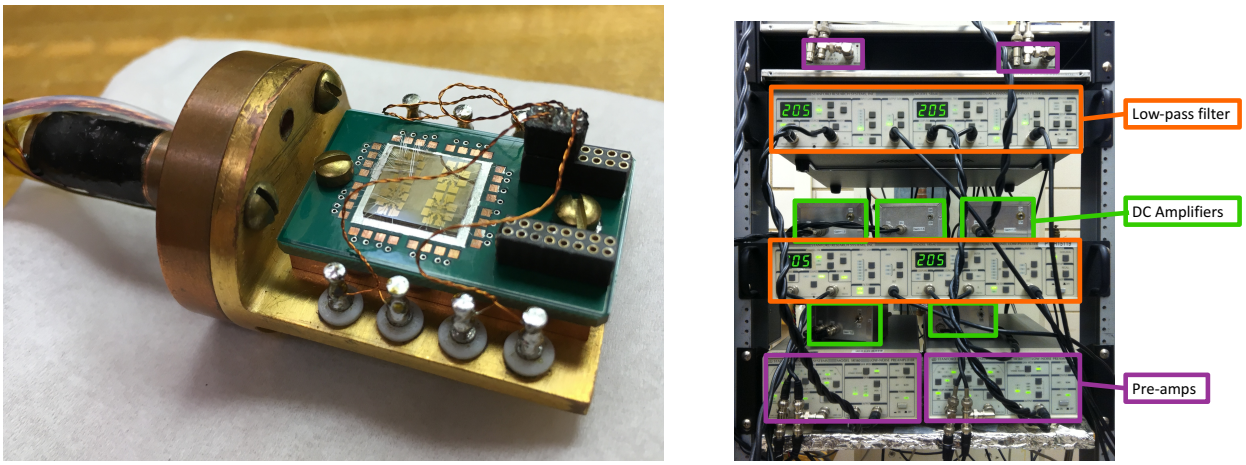

(a) (b)

Figure 3.16: **Apparatus to measure resistance fluctuations.** (a) Sample mounting onto printed circuit board. Gold contacts on the substrate and copper pads on the PCB are connected via wedge bonds with 25 µm aluminum wire; multiple bonds are made per electrical connection, for redundancy and minimization of electromechanical noise. The 8 wires on the probe stage connect to a single quadrant of the chip (i.e. one microwire) at once. Temperature sensor is on the opposite side of the stage (not visible). Where relevant, mating surfaces are coated with silver grease to maintain temperature homogeneity. (b) Noise amplifiers. Low-noise preamps (SR550s and SR560s) are highlighted in purple, custom low-input-current DC amplifiers based on INA116 chips are in green, and SR640 programmable filters in orange.

The sample stage and amplifier rack used for noise measurement are shown in Fig. 3.16.

The SR550 AC preamps (Stanford Research, Sunnyvale, CA) were chosen for their low internal noise [98], which is shown in Fig. 3.17(a). The amplifiers have a gain of 10, input impedance of 100 MΩ, and are AC coupled between 1 Hz and 100 kHz, with a gradual roll off. Many of the noise spectra studied here continue below 1 Hz, this data must be adjusted in software to account for the low-frequency attenuation of the preamps. Preamp output was passed through SR640 programmable low-pass filters (Stanford Research, Sunnyvale, CA), which added up to 80 dB (factor of 10^4) of additional gain and had the sharp frequency cut off [99] shown in Fig. 3.17(b). These filters prevent aliasing, the mapping of signals above the Nyquist frequency, which is half the sampling frequency, to lower frequencies in discrete time data. For the noise experiments in LBCO, this anti-aliasing cutoff was set to 80% of the Nyquist frequency, so 205 Hz for sampling at 512 Hz. In addition to the low-frequency noise from the pre-amps, the SR640s add an additional 5-10 nV/$\sqrt{\text{Hz}}$ input noise at higher frequencies; like the noise of the preamps, this is likely higher at frequencies near 1-10 Hz. In our experiments, the combined amplifier noise and Johnson noise of the sample was be explicitly measured at each temperature by recording voltage noise with zero applied DC current, making LBCO's resistance noise vanish.

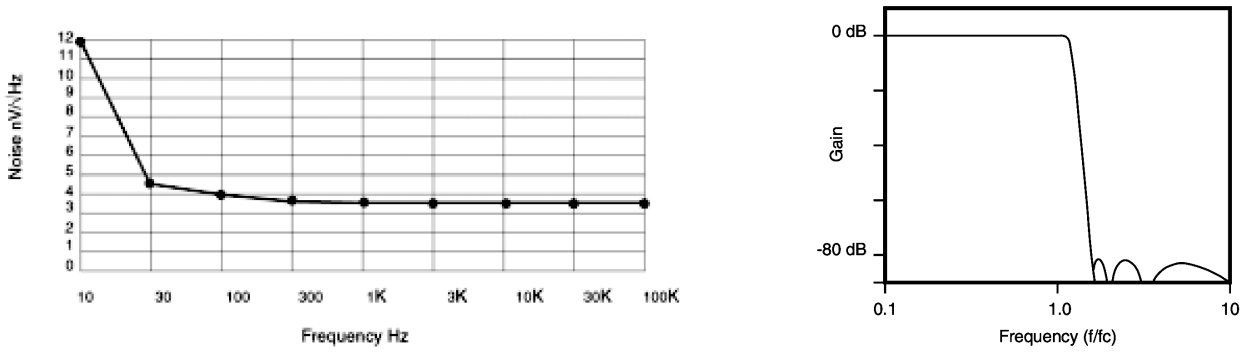

(a) (b)

Figure 3.17: **Amplifier properties affecting noise data.** From [98, 99]. (a) Low-frequency noise expected for AC-coupled SR550 preamps is $\sim$ 12 nV/$\sqrt{\text{Hz}}$ at 10 Hz. (b) SR640 filter's high-frequency attenuation above its programmed critical frequency f_c is more than -80 dB (factor of 10^{-4}).

Although AC-coupled amplifiers are optimal for noise measurement, DC voltage information may also be useful to confirm the superconducting transition in a microwire and study the linearity of IV curves in the normal state. Custom DC amplifiers, based on the INA116 integrated circuit [100], were used to record DC voltages during the LBCO noise experiments. The primary design goal of these amplifiers was to avoid interference with the AC noise measurement. In particular, the DC amps should have stable input bias currents; any current siphoned at the amplifier's input terminal will change the current flowing through the LBCO wire and fluctuations in this current would add correlated noise to the two AC amplifier channels. Data sheets for amplifier chips rarely describe input current noise statistics, but we assume that these current fluctuations will be less than the maximum specified input bias. The INA116 instrumentation amplifier circuit was used because its input bias current is typically less than 5 femtoamps, even at maximum input voltages. For a 100 kΩ device resistance, which is higher than that of the LBCO microwires presented below, a 5 fA current fluctuation is equivalent to only 0.5 nV voltage noise, peak-to-peak. Therefore we will assume the DC amplifiers used in this experiment add no noise to the AC measurement.

The current source used to supply the DC bias current across the LBCO microwire (6221 AC and DC Current Source, Keithley Instruments, Inc. Cleveland, OH) has a 100 µs response time [101], which is significantly faster than the ~ 2 ms time gap between samples in the noise experiment. Therefore the current source should be able to supply constant current across a load with fluctuating resistance. RMS current noise between 0.1 and 10 Hz is rated to be less than 0.002% of the applied DC current, for the entire measurement range used for the LBCO studies. This specification is reported for a 100 Ω load, which is much less than the resistance typical of the LBCO devices in the normal state. For a higher device resistance, we might expect the current noise to be different, so we will explicitly measure current fluctuations in our experiment by recording the time-varying voltage across a 1 kΩ wirewound resistor in series with the LBCO microwire.

Chapter 4

Characterization of LBCO Thin Films

4.1 Phase purity of LBCO powders and high-density pellets

The development of high-quality PLD targets by steric entrapment synthesis enabled our growth of LBCO films. The initial decision to pursue a metalorganic powder synthesis technique was motivated by our observation that initial low-density targets prepared by solid-state reaction produced low-quality films, even under optimal deposition parameters. While not universally required to grow superconducting films, superconductivity in the target itself can be a sign of phase purity and general material quality. Superconducting transitions were observed in our initial solid-state reacted targets, but were extremely broad and incomplete, as shown in Fig. 4.1. Superconductors with broad transitions generally show that the Meissner effect onsets at the same temperature that resistance reaches zero. The transitions in Fig. 4.1, in contrast, illustrate a very unusual type of inhomogeneity. While superconductivity may have occurred in the core of the target, the absence of a complete resistive transition suggests that the target surface (from which films are deposited) may not superconduct at all. The early solid-state reacted targets were also low-density, near 70% for all dopings.

Films grown from the early targets prepared by solid-state reaction also had evidence of inhomogeneity and weak superconductivity, as shown in Fig. 4.2. When films grown from these targets did have superconducting transitions, the superconductivity rarely

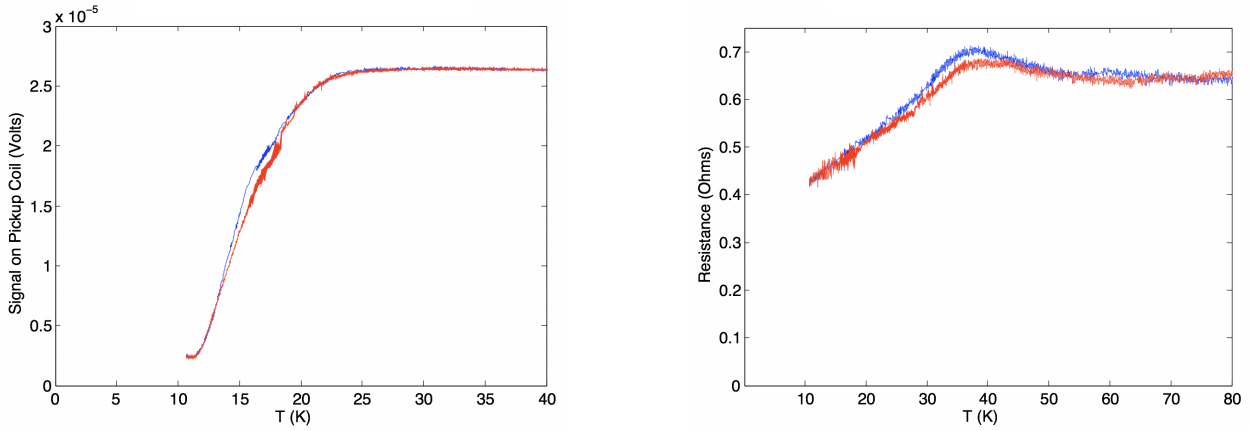

(a) (b)

Figure 4.1: **Superconducting transitions in an early LBCO target made by solid-state reaction.** (a) The Meissner transition, measured in a 2-coil system with a 25 mm coil on each side of the target, begins below 20 K for a $x = 0.155$ target, which should have a transition at 30 K. (b) In the same target, resistance drops gradually below 30 K, but never reaches below 50% of the above T_c resistance. Blue curve was measured while cooling the target, and red was measured while warming; the overlap of these two datasets indicates that the suppressed T_c and broadened transitions are a property of the sample, not thermal lag in the measurement apparatus.

survived the microfabrication process required to make devices for resistance noise measurements. In contrast, films grown from the high-density homogeneous targets prepared by steric entrapment had sharp superconducting transitions and higher yields for fabrication of superconducting devices. This improvement in film properties was likely caused by the improved phase-purity, microstructure, and dopant homogeneity of the LBCO powders and targets synthesized by steric entrapment. This description of favorable target properties will be supported below with direct characterization results on the LBCO powders and targets.

Development of a new metalorganic process for oxide powders requires careful consideration of reaction temperature. For the steric entrapment process, it is known that PVA typically begins burning off near 200 °C, but this initial combustion may leave other organic byproducts that require higher temperatures to remove. Too low of a reaction temperature may leave carbon residue in the finished ceramic powder, or may cause lo-

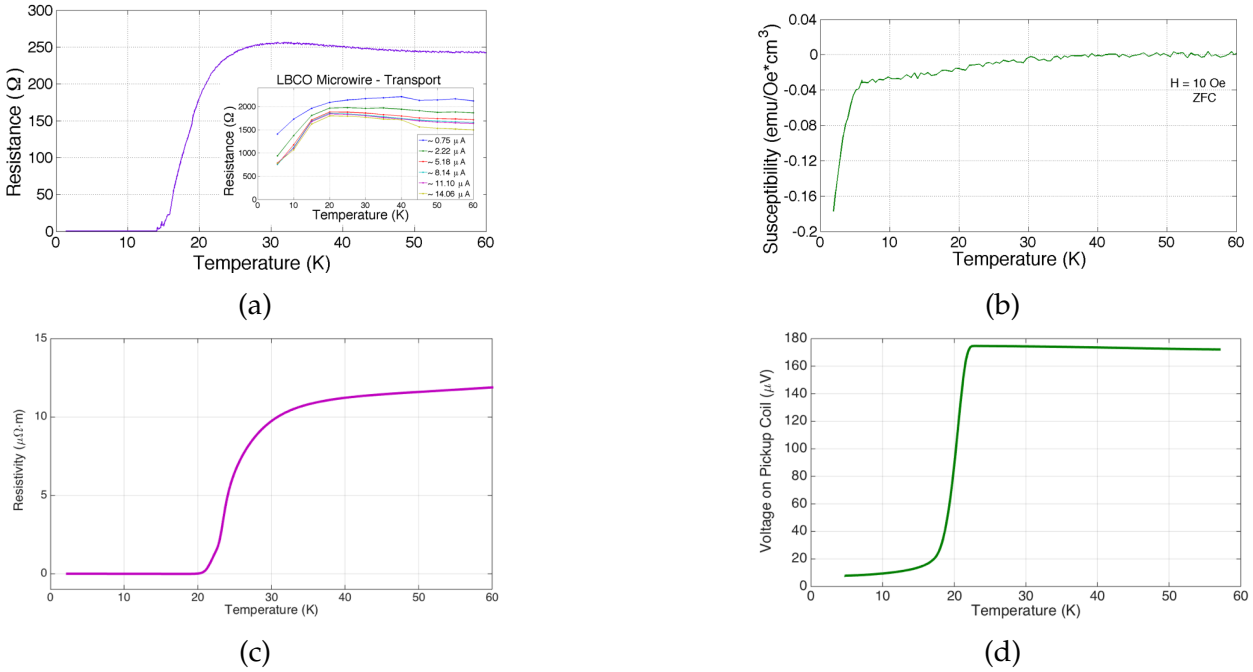

Figure 4.2: **Comparison of superconducting transitions in LBCO films grown from solid-state reacted targets and metalorganic-synthesized targets.** (a) Resistive and (b) Meissner transitions in an optimally-deposited film from a low-density solid-state reacted target. Transitions are broad and the Meissner transition (measured by SQUID magnetometry) occurs at a significantly lower temperature than the resistive transition in the same film, indicating inhomogeneity. Inset in (a) shows that the same film, after fabrication into microscopic wires, has resistive drop of only 50% and a suppressed T_c. Robust superconductivity does not survive microfabrication in films grown from low-quality targets, potentially because an incomplete volume fraction of the initial film is superconducting. (c) Resistive and (d) Meissner transitions in a film deposited from a high-density target prepared by steric entrapment. In contrast to (a)-(b), transitions are sharp. The resistive transition and Meissner transition (measured by 2-coil) occur at approximately the same temperature, indicating homogeneous superconductivity in the films grown from high-quality targets synthesized by steric entrapment.

cal formation of single-metal oxides rather than the desired mixed oxide. Too high of a reaction temperature may drive the formation of impurity phases and therefore inhomogeneity, or may cause the growth of excessively large grains that are difficult to later pelletize. Our strategy to determine the correct reaction temperature was to use DSC-TGA to determine the temperature at which the last residual carbon is removed, and powder x-ray diffraction to study phase formation as a function of reaction temperature.

DSC-TGA data is shown in Fig. 4.3, for both the as-synthesized LBCO-polymer pre-

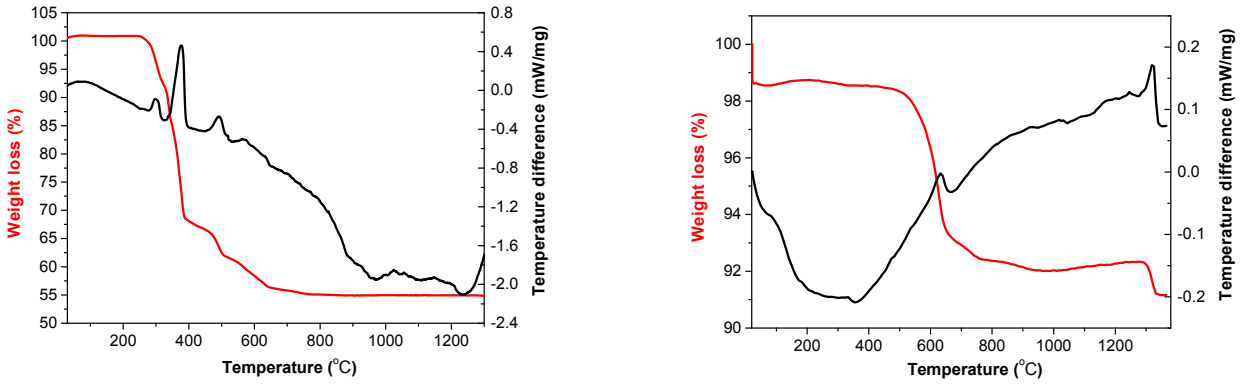

(a) (b)

Figure 4.3: **Differential scanning calorimetry and thermogravimetric analysis (DSC-TGA) of LBCO-PVA precursor powder.** (a) TGA (red) and DSC (black) curves on as-synthesized powder, measured at 5 °C/min (b) DSC-TGA data on powder that has been initially calcined at 500 °C for one hour, measured at 30 °C/min. DSC peaks correspond to combustion reactions as organic material burns off. Most of the organic loss occurs below 500 °C. Pre-calcination however reveals a small final reaction near 650 °C, and mass loss that completes near 800 °C. The feature near 1350 °C is consistent with the melting point of LBCO. Considering the initial organic-to-metal mass ratio, the final mass loss of approximately 50% is consistent with the complete removal of carbon.

cursor prepared by steric entrapment and precursor that was initially calcined in air. The decomposition and removal of organic material occurs predominantly below 650 °C and is complete by 800 °C. This reaction temperature is extremely low compared to alternative techniques. Solid-state reaction favors temperatures approaching the melting point of the material, e.g. 1000 °C for LBCO, and studies of chelation-based metalorganic routes to HTSC powders have obtained pure mixed-oxide phases at approximately 900 °C, with particle sizes in excess of 1 µm [102]. The low reaction temperatures of steric entrapment usually results in nanoscopic grain sizes [71, 72]. Powder XRD scans (along the coupled $2\theta - \omega$ axis) of $La_{1.905}Ba_{0.095}CuO_4$, after reaction at various temperatures, are shown in Fig. 4.4. Although $La_{2-x}Ba_xCuO_4$ has already begun to form at 500 °C, so have La_2O_3 and CuO impurities. By 800 °C, these impurity phases have decomposed and a pure La-214 oxide phase is present. On the basis of this DSC-TGA and powder XRD data, the final powder reaction recipe was to heat first at 500 °C for 1 h, regrind, then heat a second

time at 800 °C for 30 minutes. The initial 500 °C treatment helped to reduce the particle size and favored more gradual release of volatiles at the final 800 °C stage. Higher reaction temperatures were avoided in order to maintain the fine-grained morphology; trial powders reacted at 1000 °C had a noticeably coarser texture visible with the naked eye.

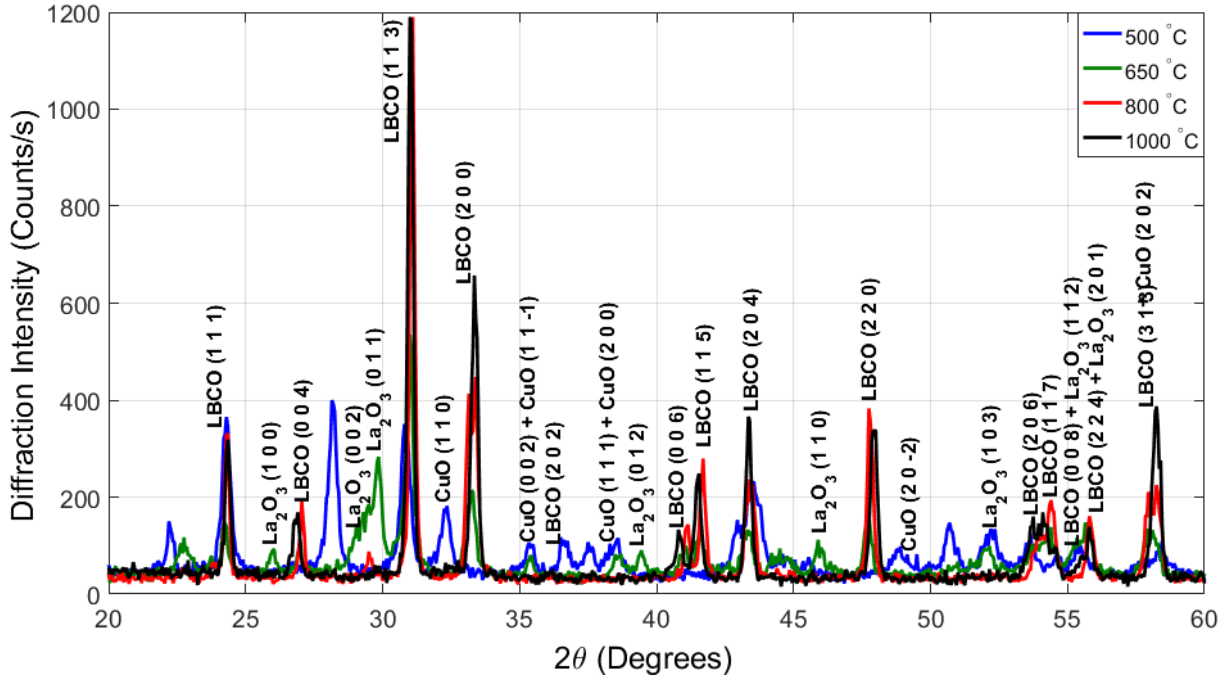

Figure 4.4: **Powder x-ray diffraction pattern of x= 0.095 LBCO powder synthesized at different reaction temperatures.** $2\theta - \omega$ scans were taken at room temperature after the reaction had completed. The La-214 phase begins forming at low temperatures and near-perfect phase purity is obtained at temperatures $\geq$ 800°C. Lower temperatures have numerous impurity peaks, mostly La_2O_3 and CuO. For the 800°C-reacted powder, a slight La_2O_3 impurity peak is still visible near 30°.

The final powders used to form the PLD targets were phase-pure, dense, and superconducting. XRD patterns (Fig. 4.5) indicate high purity of the crystalline $La_{2-x}Ba_xCuO_4$ phase for all three compositions formed into PLD targets. Observed density values for these powders (and their respective targets) are reported in Table 4.1. Observed powder densities are close to the maximum possible densities of LBCO, especially for high-temperature reaction. For $x = 0.155$ powders reacted at 800 °C and 1000 °C, superconductivity was also apparent by measuring magnetization as a function of field at 1.9 K

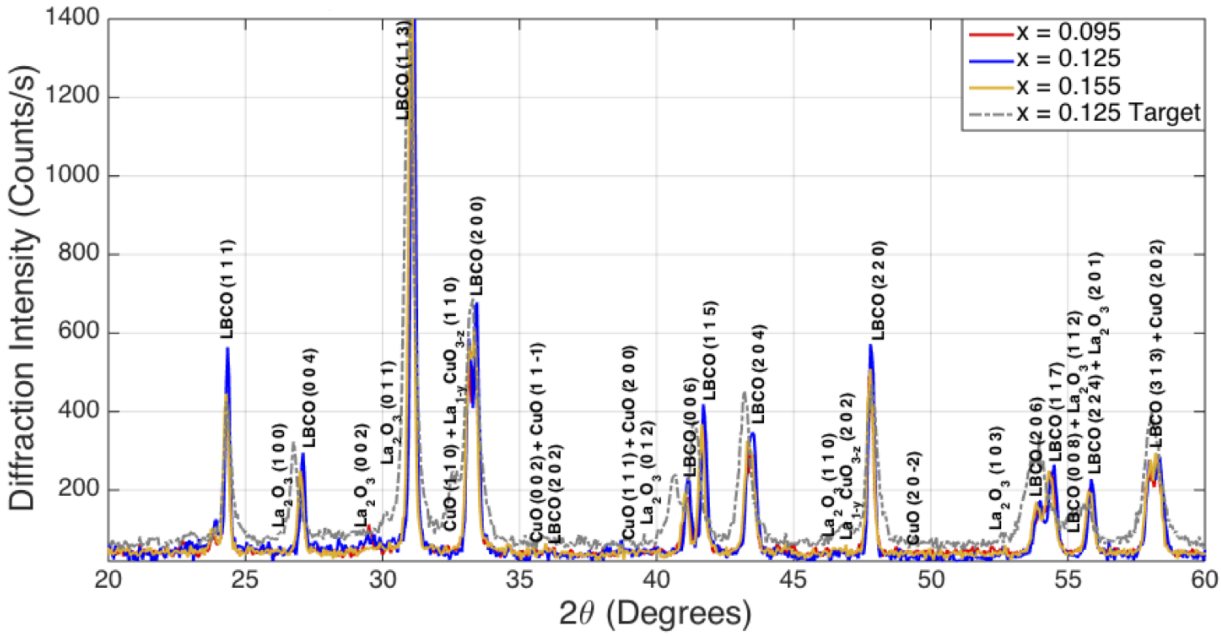

Figure 4.5: **X-ray diffraction patterns of all dopings of LBCO powders used for PLD targets.** $2\theta - \omega$ scans were taken at room temperature after reaction at 800 °. Good phase purity is obtained for all dopings, although a possible impurity peak associated with La_2O_3 (101) may be visible near $2\theta = 30°$. The dashed grey line is the pattern of a completed PLD target, after sintering and polishing. Some peak broadening is apparent due to the strained, small-grain microstructure caused by polishing. However phase purity may actually be improved after the final sintering step – no single-oxide peaks are visible.

(Fig. 4.6). The presence of strong diamagnetism, but no hysteresis, in the 800 °C sample suggests successful synthesis of a superconducting La-214 phase in nanoscopic grains with grain size less than the magnetic penetration depth. Grain size was not measured (e.g. with electron microscopy) other than indirectly through powder magnetometry. In the $x = 0.155$ 1000 °C powder with large grains and robust superconductivity, additional temperature sweeps confirmed the expected $T_c = 30$ K.

Superconductivity is easier to measure in dense, consolidated samples, so additional magnetometry was performed on pieces from small (10 mm diameter) sintered test pellets. Magnetization versus temperature sweeps, shown in Fig. 4.7, were used both to confirm the variation in T_c with doping and to optimize the sintering recipe. Comparison of pellets at $x = 0.125$ and $x = 0.155$ (Fig. 4.7(a)) shows that the LBCO pellet near the 1/8

Table 4.1: **Densities of LBCO powders and targets.** Powder and bulk volumes were measured by gas pycnometry and Archimedes' method, respectively. Ideal densities are the calculated density of a single LBCO unit cell (i.e. a perfect single crystal), and are used to compute the measured density as a percentage.

Composition	Powder Density (g/cm^3)		Bulk Density (g/cm^3)		
	Heat 800 °C	Heat 1000 °C	Ideal	Measured	Density (%)
$La_{1.905}Ba_{0.095}CuO_4$	6.68 ± 0.01	7.02 ± 0.01	7.0729	6.81 ± 0.01	96.25 ± 0.51
$La_{1.875}Ba_{0.125}CuO_4$	6.70 ± 0.01	7.05 ± 0.01	7.0654	6.85 ± 0.01	96.95 ± 0.30
$La_{1.845}Ba_{0.155}CuO_4$	6.63 ± 0.01	7.00 ± 0.01	7.0585	6.74 ± 0.01	95.51 ± 0.25

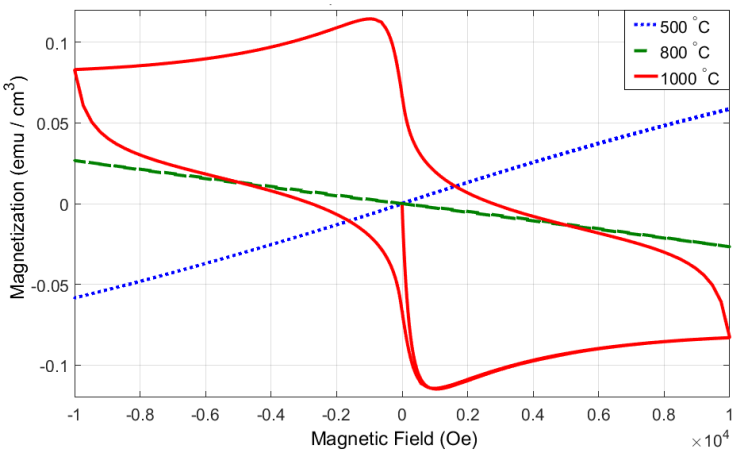

Figure 4.6: **Magnetization hysteresis loops of x= 0.155 LBCO powder synthesized at different reaction temperatures, measured by VSM at 1.9 K.** The powder reacted at 1000 °C, which has large grain size, shows the hysteretic diamagnetic behavior typical of a type II superconductor, with a critical field near $H_{c1} \sim 0.1$ T. The 500 °C-reacted powder is weakly paramagnetic, which is typical for many organic materials. The 800 °C-reacted powder has no hysteresis, but has a diamagnetic moment comparable to the 1000 °C sample. Recalling that superconductors are orders-of-magnitude stronger diamagnets than any other known material, this must mean that the 800 °C sample is also superconducting. One explanation for the lack of hysteresis would be that the 800 °C sample has a typical grain size less than the Ginzburg-Landau penetration depth $\lambda \sim 200$ nm; so the magnetometry confirms that we have nanoscopic grains.

anomaly does have suppressed superconductivity, both in terms of a low T_c and a lesser magnitude of diamagnetism. Several pellet sintering recipes were also attempted, and the sharpest, most complete Meissner transitions were observed in test pellets sintered at 1050 °C for 4 hours. The optimization of the sintering recipe was also studied via bulk pellet density (Table 4.1) and x-ray diffraction (example pattern in Fig. 4.5, grey curve).

Maximal density and phase purity were again observed for the 1050 °C × 4 h recipe.

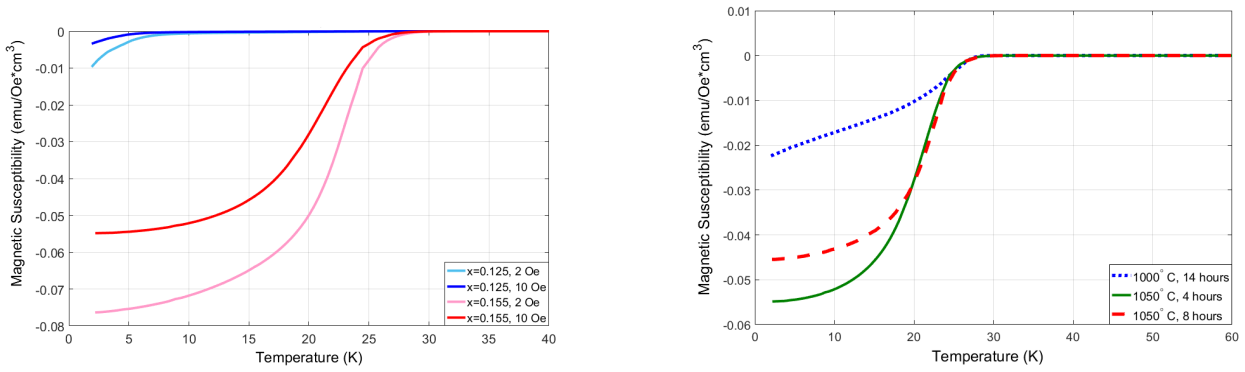

(a) (b)

Figure 4.7: **Magnetic susceptibility measurements of small LBCO test pellets, measured by VSM.** Samples were cooled in zero field, field was turned on at base temperature, and then data recorded during warming. (a) Comparison of pellets' Meissner transitions at $x = 0.125$ and $x = 0.155$ dopings. In agreement with LBCO's phase diagram, the $x = 1/8$ sample has weak superconductivity and a suppressed T_c, near 5 K in this sample; the $x = 0.155$ sample has high T_c. As expected for a highly granular type II superconductor, increasing field rapidly weakens the susceptibility due to flux penetration. (b) Comparison of $x = 0.155$ pellets with different sintering recipes, confirming that 1050 °C × 4 h is optimal. Because the Meissner effect relies on circulating currents, it requires well-connected grains and should be a sensitive probe of the sintered microstructure.

XRD revealed that the unpolished, as-grown surfaces of all sintered pellets and targets contained a measurable amount of a stable $LaCuO_3$ impurity phase. This phase was least prevalent for the brief sintering times at 1050 °C, as used for the final PLD targets. Resurfacing pellets with $LaCuO_3$ and remeasuring XRD patterns showed much less impurity phase; e.g. it is not visible in the pellet pattern shown in Fig. 4.5. This would suggest that $LaCuO_3$ nucleates preferentially at the target surface, rather than throughout the bulk. However, careful additional measurements of unsintered powder were also able to find this impurity phase in trace amounts, suggesting that it is likely present to some degree in all of our targets, even before sintering. Sintering at temperatures above 1050 °C was found to favor formation of the $LaCuO_3$ phase. LBCO's intolerance of longer sintering times (e.g. as suggested by Fig. 4.7(b)) is also unusual. Most materials become denser the longer they are sintered, but repeated trials found that this was not the case for

our LBCO pellets. The kinetics causing this sintering behavior can be complicated and microstructure-dependent, but might occur, for example, if volume change or atomic rearrangement due to crystallization induces microcracks in the ceramic. Note that because LBCO does not withstand long-duration or high-temperature sintering, phase homogeneity and grain size are largely unchanged during the consolidation stage. Therefore, it was especially important that these sample qualities were optimized at the completion of powder synthesis.

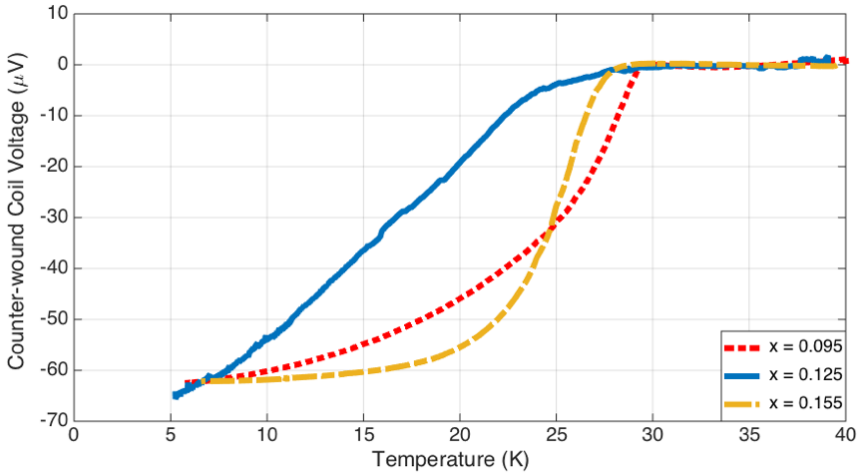

Figure 4.8: **Meissner transitions of the PLD targets at three dopings used for film growth.** Measured in a counter-wound coil geometry with 1-mm-diameter coils at the center of the same surface used for ablation. High T_c is apparent for both the $x = 0.095$ and $x = 0.155$ targets. The $x = 0.125$ target has a high-temperature Meissner onset, but its superconductivity is weaker than the other targets' at all temperatures. We interpret the shape of the $x = 1/8$ Meissner transition as formation of the intended superconducting phase, albeit with some degree of sample inhomogeneity. An alternative optimistic interpretation is that, in very large samples like these 22 mm $\times$ 7 mm targets, magnetic screening may be significant even if only a minority of the sample is superconducting, and therefore the actual *average* T_c of the $x = 1/8$ target may be lower than what is indicated here.

The surface-sensitive Meissner measurement of the three $La_{2-x}Ba_xCuO_4$ ($x = 0.095$, 0.125 and 0.155) targets indicated that each is superconducting (Fig. 4.8). While not strictly necessary to ensure high-quality PVD-grown films, the presence of the superconducting phase in the polycrystalline ceramic target is a strong indication that the desired

superconducting behavior will be easily accessible in the thin films. The diamagnetic transitions of the $x = 0.095$ and $x = 0.155$ targets begin at 29.6 K and 28.4 K, respectively, as expected for the optimal dopings of LBCO [31].

Comparatively, superconductivity is suppressed in the $x = 1/8$ target. Its Meissner transition onsets gradually near 26.5 K and the magnitude of its diamagnetism varies more slowly with temperature than was observed at optimal dopings. This differs from the sharp Meissner transitions below 4 K previously reported in some $x = 1/8$ LBCO single crystals [31]. However, the slow variation in diamagnetism in the $x = 1/8$ target does resemble some granular high-T_c superconductors [103], in which different polycrystalline grains may have varying local dopant concentrations. LBCO is likely to be uniquely sensitive to such doping variations, due to the drastic variation in T_c near $x = 1/8$ apparent in its phase diagram. Therefore, we interpret the shape of the $x = 1/8$ Meissner transition in Fig. 4.8 as evidence for formation of the intended superconducting phase with some degree of sample inhomogeneity.

4.2 Optimization of laser deposition parameters

The pulsed laser deposition recipe was optimized by growing multiple films while varying a single deposition parameter at a time, and studying the films' properties after growth. For example, the per-pulse energy of the laser was optimized by growing films at energies in the range 150 mJ to 400 mJ (note that this is the energy after the attenuation stack, not at the laser itself). Sample AFM data for the sample sequence is shown in Fig. 4.9, while low-temperature resistance data is in Fig. 4.10. The combination of these datasets suggested an optimal laser energy of 250 mJ. Films at 200 mJ and below had broader superconducting transitions, presumably due to dopant inhomogeneity caused by the weak surface diffusion of material deposited at low energy. Films at 300 mJ and above had visibly roughened surfaces in AFM images due to resputtering effects, which

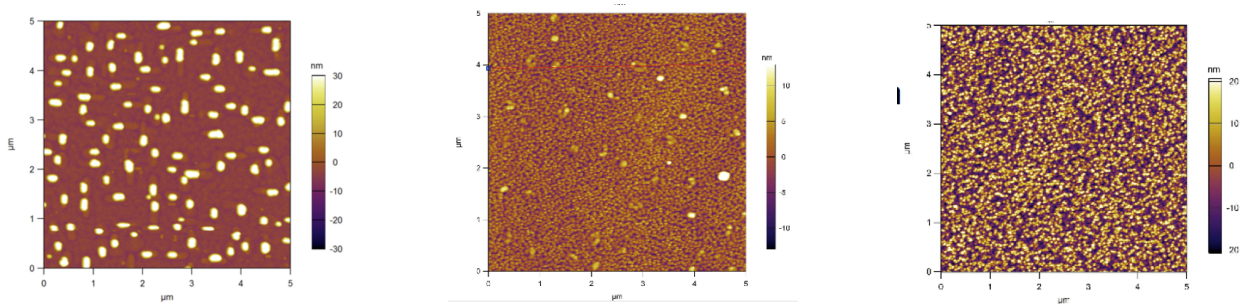

(a) (b) (c)

Figure 4.9: **AFM of LBCO film topography for deposition at different laser energies.** (a) 150 mJ. At low energies, adatoms incident on the susbtrate are not energetic enough to overcome surface tension. Wetting of the substrate is poor, and the LBCO tends to agglomerate in 3D particles rather than a 2D film. (b) 250 mJ. Average surface roughness is only ∼2 nm for a film that is ∼50 nm thick. Some 3D particles or "crystallites" are visible, but the concentration of these particles was found to be highly variable between samples. (c) 400 mJ. At high energies, material incident on the substrate surface is energetic enough to sputter away existing material, which significantly increases surface roughness.

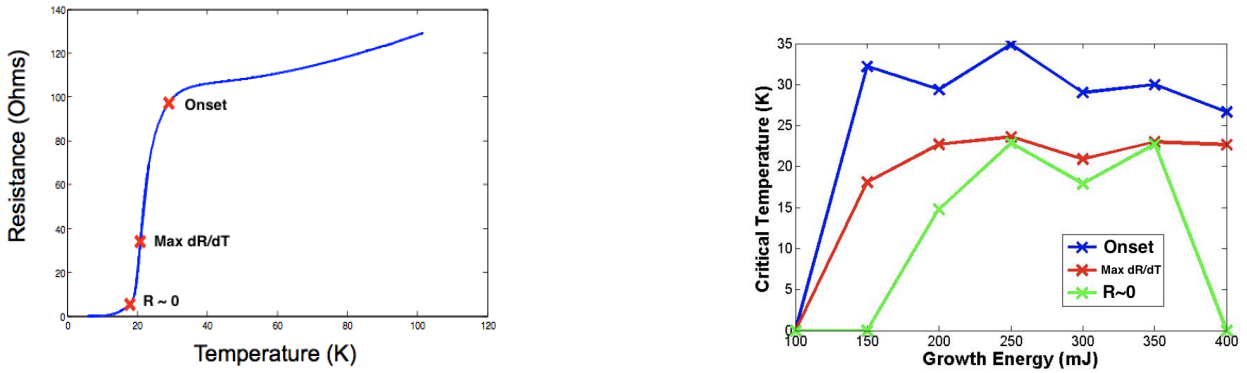

(a) (b)

Figure 4.10: **Sharpness of superconducting transitions in $R(T)$ curves, as a function of laser energy during PLD of x= 0.095 LBCO.** (a) Most of the LBCO thin films have resistive transitions of finite breadth. Three points are identified as shown for each resistance-vs-temperature curve. Resistance was measured with an AC lock-in technique. (b) Superconducting onset, point of maximum slope in $R(T)$, and the "bottom" of the superconducting transition for the studied range of laser energies. Ideal $x = 0.095$ LBCO should have $T_c = 30$ K and a sharp transition, such that the three definitions of T_c overlap; this is most nearly obtained for growths between 250 mJ and 350 mJ.

also tend to cause non-stoichiometry.

The temperature of the $LaAlO_3$ substrate during deposition was optimized by a similar suite of post-growth characterizations. Fig. 4.11 shows x-ray diffraction survey scans

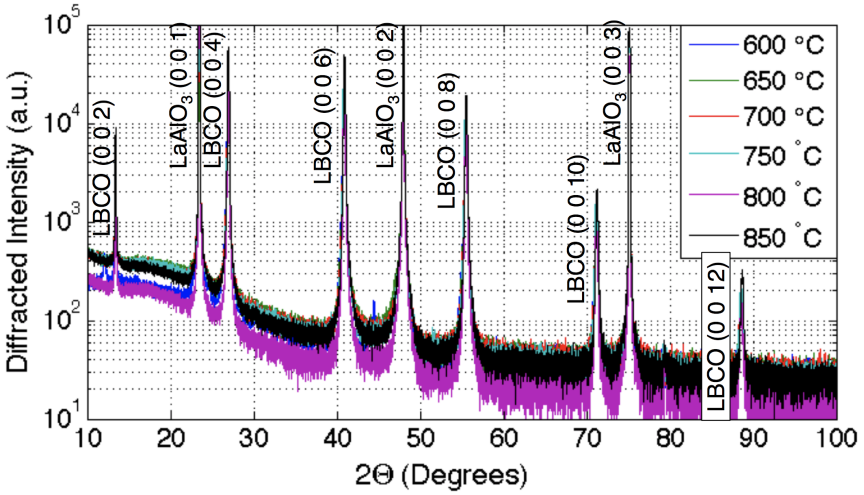

Figure 4.11: **Survey $2\theta-\omega$ x-ray diffraction scans for PLD of x= 0.095 LBCO at variable substrate temperatures (in °C).** Both substrate peaks and film peaks are visible. At all growth temperatures, the LBCO forms the correct La-214 phase and has a c-axis oriented normal to the substrate. The film grown at 600 °C may have additional peaks associated with an impurity phase, near $2\theta = 13°$ and 44°.

for LBCO grown at temperatures between 600 °C and 850 °C. No significant peak broadening or shifts are observed as a function of growth temperature, indicating that the c-axis oriented $La_{2-x}Ba_xCuO_4$ phase occurs at all growth temperatures. Small additional peaks may be observed for the lowest growth temperature, suggesting an impurity phase. Otherwise, the XRD patterns do not clearly point to a singular optimal growth temperature. It should be clarified that, because films were deposited onto highly oriented single-crystal substrates, any impurity phase may also be crystalline and highly oriented, like the primary LBCO phase itself. Depending on orientation, crystalline impurity phases may not have visible peaks at the particular scan conditions used for these diffraction surveys; they may only have peaks at specific rotations around the surface normal (φ) or the incident beam axis (ψ). In other words, the absence of observed impurity peaks in an epitaxial sample does not conclusively prove the absence of impurities. Impurities may also be amorphous, with no XRD signature.

We are also interested in whether our LBCO films have the appropriate in-plane orientation. In principle, the survey scans of Fig. 4.11 only confirm that LBCO's c-axis is

normal to the substrate surface. It may still be possible that the film's unit cells are randomly rotated about the *c*-axis, forming a mosaic structure that could cause unintended behavior in the resistance noise measurement. We want to confirm that this isn't the case. Crystallographic *pole figures* are a standard x-ray technique to confirm the three-dimensional texture of materials and, in this case, are used to confirm epitaxial growth of LBCO on $LaAlO_3$.

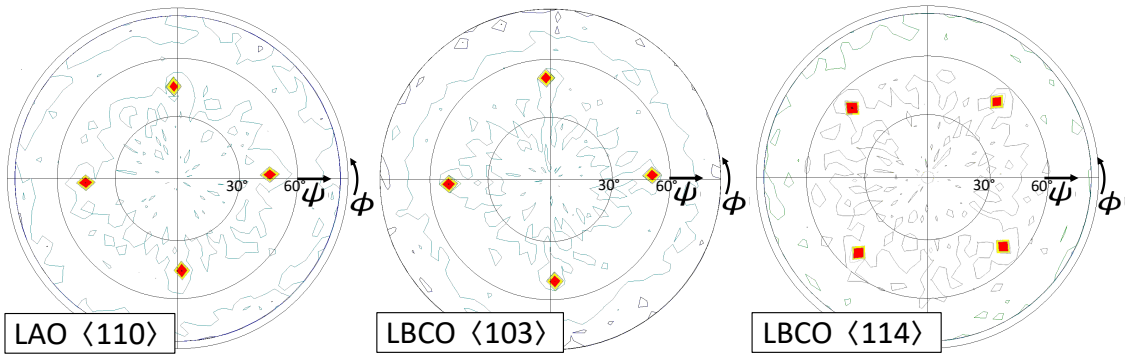

Figure 4.12: **Pole Figures confirming epitaxy of LBCO on LAO.** All scans were performed with Cu K-α x-rays on the same 320 nm-thick LBCO film grown from an $x = 0.155$ source onto $LaAlO_3$. Each figure is recorded by fixing the diffraction angle to probe the set of planes indicated, then rotating the sample through a full range of ψ (tilt angle) and ϕ (angle about film normal). See Fig. 3.9(a) on diffraction angles. The diffracted x-ray intensities are contour-plotted on a stereographic projection, with ψ as the radial cordinate, and ϕ as the angle about the plot origin. Angles with diffracted intensities greater than a few thousand counts/second are shaded orange-red. Figures for the three Miller indices shown here were recorded in sequence, without unmounting the sample. Diffraction peaks occur at (ψ, ϕ) angles expected for the cubic symmetry of $LaAlO_3$ and the the tetragonal symmetry of LBCO. The relative orientations between substrate and film peaks confirm that LBCO was grown epitaxially on $LaAlO_3$.

Pole figures are generated by fixing θ and ω, that is, probing a Bragg condition that tests only for atomic planes at a fixed spacing d, and then rotating the sample in all directions. The sample rotation is described by ψ, the tilting of the sample about the approximate LAO (100) direction, and ϕ, the rotation of the sample stage, equivalent in this case to rotation about the film normal or LBCO's *c*-axis. For the same LBCO film grown from a nominal $x = 0.155$ source, three pole figures are shown in Fig. 4.12, with diffracted intensity plotted as a function of ψ and ϕ (arbitrary color scale). The general problem of

predicting the expected pole figure for a given crystal symmetry and Miller index isn't necessarily straightforward or intuitive, and is often explored through simulation software. This can be more difficult for certain symmetries, or for high-order indices $\langle hkl \rangle$ with large h, k, or l. However, for the simple low-order indices studied in Fig. 4.12, the pole figures are comprehensible and simulation was unnecessary. For example, in the pole figure for the LAO $\langle 110 \rangle = \langle 101 \rangle = \langle 011 \rangle$ family of atomic planes, the four observed peaks correspond to the four equivalent ways a diagonal plane could be defined from an edge at the bottom of LAO's cubic cell, to an edge at the top of the cell. Similar $\langle 110 \rangle$ planes between the side edges of the unit cell are not observed here because the experiment was truncated below $\psi = 90^\circ$ where these peaks would have occurred. LBCO's $\langle 103 \rangle$ figure looks similar to the LAO $\langle 110 \rangle$ figure because in the tetragonal cell of LBCO, $a \approx c/3$. The observation that the LAO $\langle 110 \rangle$ peaks occur at the same angles ϕ as the LBCO $\langle 103 \rangle$ peaks, in the same sample, confirms that the LBCO grows epitaxially. That is, the in-plane orientation of LBCO's crystal lattice is uniform and set by the substrate. Epitaxy is independently confirmed by the observation of LBCO $\langle 114 \rangle$ peaks rotated by 45° in ϕ relative to the LAO $\langle 110 \rangle$ peaks. Unlike some of the other characterizations discussed, pole figures were not studied as a function of film growth parameters. It is assumed that epitaxy occurred in nearly all LBCO films, because of the close LBCO-LAO lattice match, but this was only directly confirmed in one sample.

Surface topography, as measured by AFM, as a function of deposition temperatures is described in Fig. 4.13. Every film in this sequence was grown with a laser energy of 250 mJ. As expected, smoother films appear to form at higher growth temperatures, because of the enhanced surface diffusion. However, the highest temperatures show the presence of a possible impurity phase. All the large crystallites in the film grown at 850 $^\circ$C appear to point in the same direction, so the impurity phase may be a highly-oriented crystalline phase, which may explain why it was not detected by XRD.

Although the structural properties of LBCO from AFM and XRD were only weakly

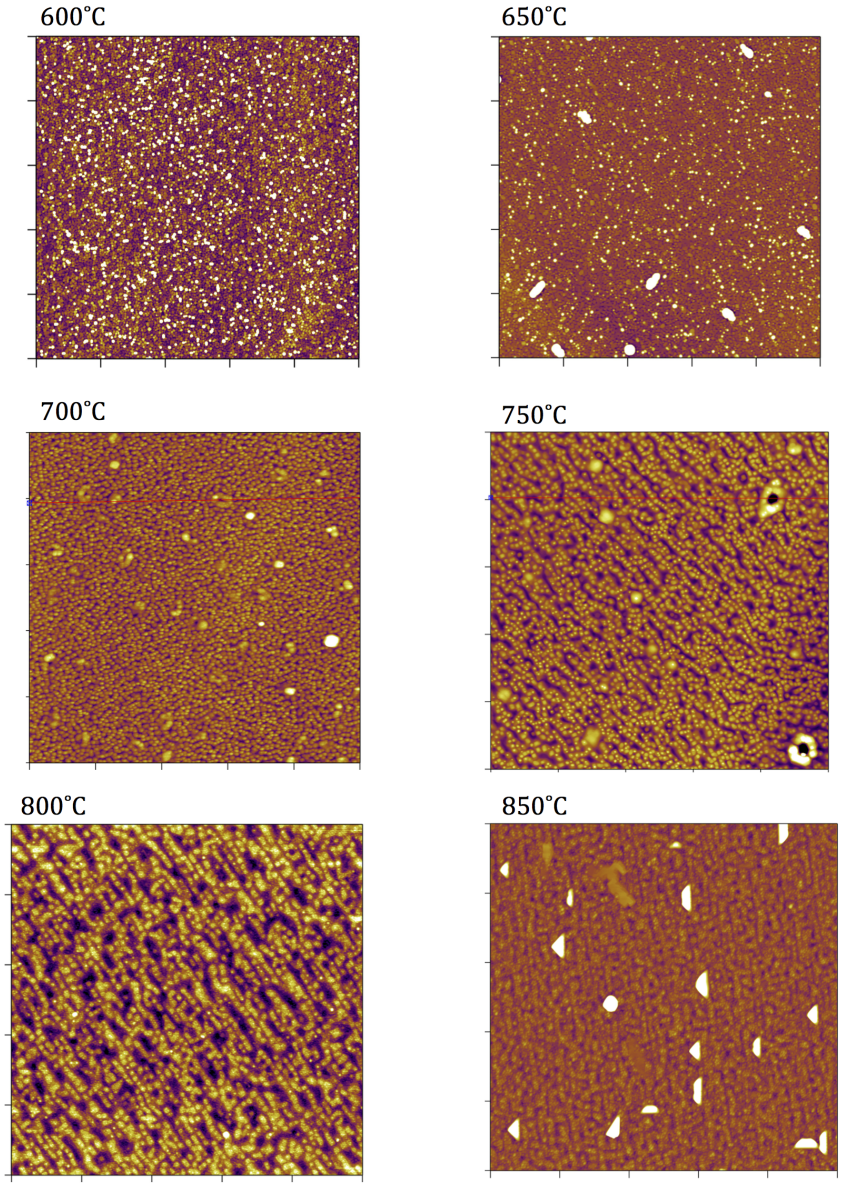

Figure 4.13: **AFM tomography of PLD-grown x= 0.095 LBCO films at variable substrate temperatures.** All scans are 5 µm wide and have color scales spanning either 15 nm (600 °C and 800 °C) or 25 nm (others). The primary lattice directions of the cubic LAO substrate are along the edges of the square scan. At low temperatures, surface diffusion of deposited material is limited and films are rough. The smoothest films are grown near 700 °C. At high temperatures, oriented texturing is visible and may indicate that the underlying substrate's atomic steps correlate with film features. At 850 °C, oriented triangular crystallites are present and may be associated with a 3D impurity phase.

dependent on the substrate temperature during deposition, the superconductivity in the films was strongly affected by growth temperature. Meissner transitions, from the 2-coil

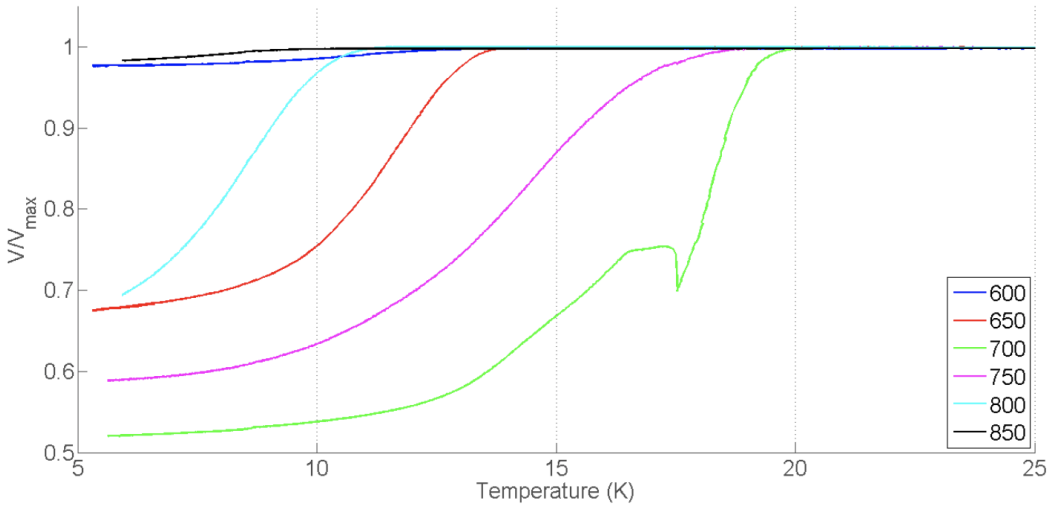

Figure 4.14: **Meissner transitions of PLD-grown x= 0.095 LBCO films at variable substrate temperatures.** Measurements with film samples sandwiched between two inductively coupled coils as in Fig. 3.13(b), show diamagnetic transitions for all growth temperatures but the transitions vary considerably. The feature near 17.5 K in the green curve (700 °C) is believed to be associated with thermal contraction of the coil geometry; it was detectable even with an empty sample stage, and was not present in the next-generation counterwound coil geometry.

technique, are shown for a range of growth temperatures in Fig. 4.14. For films grown from a $x = 0.095$ target, growth temperatures ≤ 650 °C *and* ≥ 750 °C had both suppressed T_c and incomplete superconducting volume fraction, as evidenced by the smaller changes in the pickup coil's voltage. Recall that for $x = 0.095$, $T_c = 30$ K according to the LBCO phase diagram. Critical temperatures close to this value (i.e. as high as possible for an LBCO film), indicate that the deposition process is accurately transferring the correct barium content from the target to the film. The highest-T_c, sharpest Meissner transitions were observed only for growth temperatures near 700 °C. At low growth temperatures, samples may be weakly superconducting due to granularity of the superconducting material, as supported by AFM (Fig. 4.13). At high growth temperatures, samples may be weakly superconducting because barium, which has a much higher vapor pressure than La and Cu, has a low sticking coefficient, and deposited films may have significantly less Ba content than the originating PLD target. The combination of these two effects would

explain the relatively narrow window of growth temperatures for which superconductivity is robust.

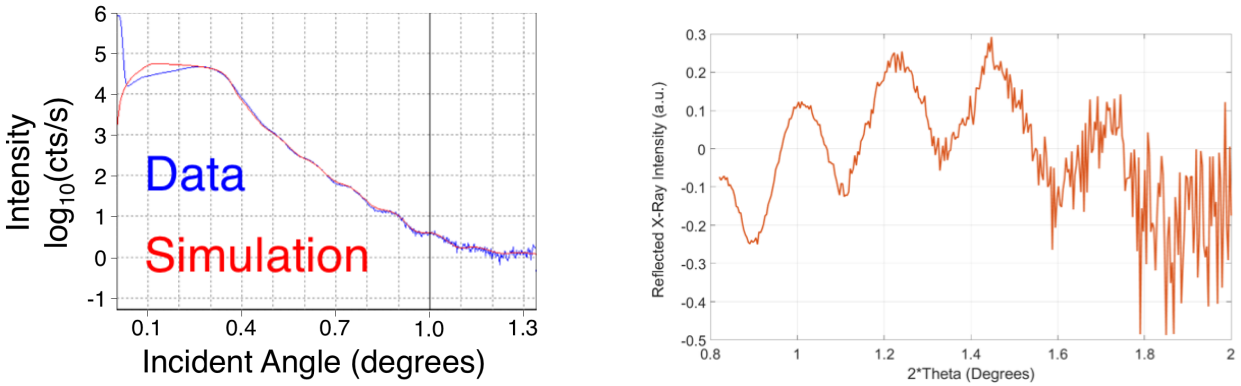

(a) (b)

Figure 4.15: **Interference fringes in x-ray reflectivity used to deduce film thickness.** (a) $2\theta - \omega$ scan on a 29.9 nm-thick LBCO film, at grazing angles where thin-film interference effects dominate. Reflected signal decays rapidly with angle, with superposed small-amplitude oscillations. Computer simulation fits for film thickness, substrate and film roughness, and substrate and film density. (b) Reflectivity scan for a 37.0 nm-thick LBCO film, after subtracting an empirical fit to the background intensity decay. Average peak separation is used to compute thickness $\approx \lambda/2(\Delta\theta)$. This method is simpler than simulation of the full signal.

Film thickness was measured non-destructively via the interference-based x-ray reflectivity (XRR) technique. As shown in Fig. 4.15, reflected intensity is dominated by a rapid decay as incident angle is increased beyond 0.5°, but oscillations are also visible. The full signal can be simulated, as shown in Fig. 4.15(a). In addition to film thickness, the simulation also provides approximate (electron) densities that are consistent with the stoichiometry of $La_{2-x}Ba_xCuO_4$ and $LaAlO_3$, and rms roughness values of the film-substrate interface and top film surface that are consistent with AFM images. However, simulation is time consuming and prone to systematic errors in the computed sample thickness, so most samples' thicknesses were instead computed by subtracting a simple fit to the background decay in the reflected intensity with angle. The thin-film interference oscillations are then clear and their average period gives thickness t by $t \approx \lambda/2(\Delta\theta)$, with $\lambda = 0.154056$ nm for the Cu K-α line.

Film thicknesses calculated from XRR allowed estimation of the average deposition rates from the three LBCO targets prepared by steric entrapment. For the optimal deposition recipe at 300 mTorr O_2, 250 mJ laser energy, and 700 °C, these rates were found to be 0.127 $\mathring{A}$/pulse for the $x = 0.095$ target, 0.117 $\mathring{A}$/pulse for the $x = 0.125$ target, and 0.171 $\mathring{A}$/pulse for the $x = 0.155$ target. The rate at which target material is vaporized in PLD depends sensitively on the granularity and density of the ceramic target, so these variations are probably caused more by target microstructure, rather than stoichiometry. For example, the least dense target, $x = 0.155$, also had the highest ablation/deposition rate. We estimate that there is approximately 20% growth-to-growth variation in the deposition rate, for all targets. Crucially, the deposition rate for all films in this study was significantly less per-pulse than the typical atomic layer spacing of LBCO, which is near ~ 2 $\mathring{A}$. This "slow" deposition rate favors two-dimensional diffusive growth kinetics that are good for sample homogeneity, smoothness, and crystallinity [79].

For a small number of samples, a corner of the substrate was masked during deposition, and the thickness computed by XRR was compared to direct measurements of the step edge height from contact and optical profilometry; the complimentary techniques were roughly in agreement. It should be noted that for LBCO films, XRR is vastly more convenient and precise than profilometry. It is extremely challenging to precisely mask samples grown at elevated temperatures, especially when they are thin, and profilometry techniques on twinned substrates show surface features due to twin domains that can obscure features intentionally placed by a deposition mask. The non-destructive nature of XRR also allowed film thickness measurements in samples that were later fabricated into working devices.

A counter-wound coil geometry, similar to that used to study the Meissner effect in the targets, was also used to characterize superconductivity in the films, with a representative transition at each doping shown in Fig. 4.16. Films deposited from targets at dopings $x = 0.095$, $x = 0.125$, and $x = 0.155$ respectively had superconducting onsets at $T_c = 22.5$

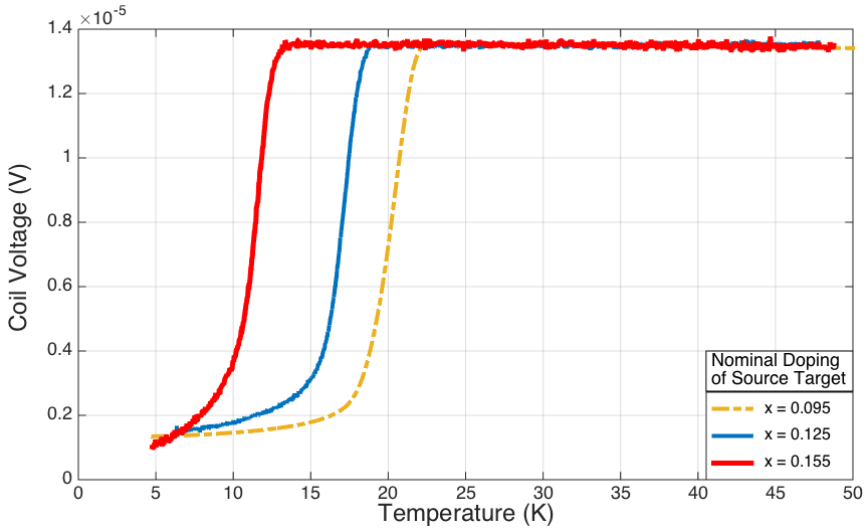

(a)

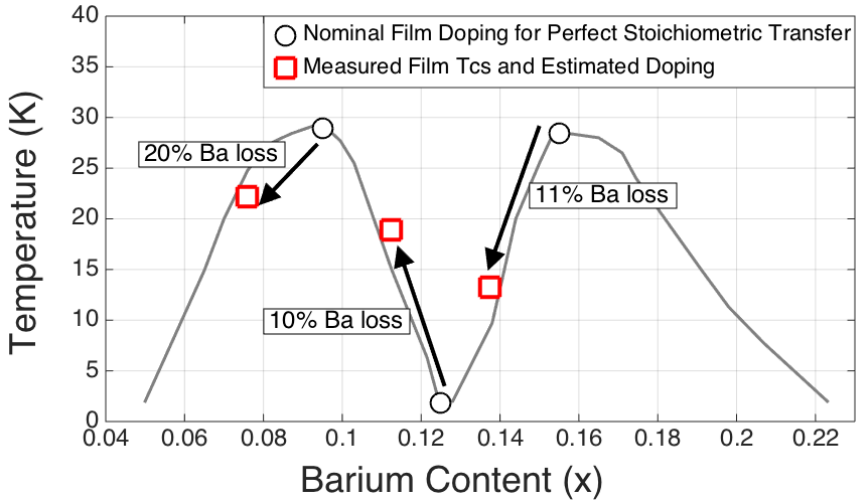

(b)

Figure 4.16: **Comparison of Meissner transitions for LBCO films at three dopings.** (a) Diamagnetic transitions, measured in the counterwound coil geometry of Fig. 3.13, gives Meissner onsets at $T_c(x = 0.095) = 22.5$ K, $T_c(x = 0.125) = 18.9$ K, and $T_c(x = 0.155) = 13.3$ K. (b) The measured T_c's of the LBCO films (red squares) are consistent with the nominal dopings of the PLD targets (white circles) combined with a relative 10-20% barium loss during film growth.

K, 18.9 K and 13.3 K. Naively, one might expect film transitions to occur near 30 K at the optimal $x = 0.095$ and $x = 0.155$ dopings and near 4 K at the $x = 0.125$ anomaly. However, this expectation assumes perfect transfer of dopant stoichiometry from the bulk PLD target to the deposited film. Typically, PLD *does* accurately transfers stoichiome-

try from the deposition target to the ablated *plasma*, but non-stoichiometry may develop during adhesion of the plasma's high-energy adatoms to the substrate, with high-vapor-pressure elements sticking poorly, or preferentially reevaporating from the topmost film layer. In LBCO, the high vapor pressure of Ba means that the deposited material will be barium-deficient relative to the deposition source.

The known phase diagram of LBCO (Fig. 4.16(b)) may be used to quantify the rate of barium loss. For films grown from a bulk target at $x = 0.095$ doping, we compare the $x < 0.095$ boundary curve between the superconducting and normal states to the film's measured T_c at 22.5 K, deducing that the deposited barium-deficient films have the doping $x = 0.076$. Similarly, we estimate that the PLD targets at $x = 0.125$ and $x = 0.155$ gave films with dopings at $x = 0.1125$ and $x = 0.1375$, respectively. Note that for all three compositions studied here, the film doping is $80 - 90\%$ of the target doping, consistent with an approximately constant rate of barium loss due to reevaporation or reduced adhesion. The variation between an 80% and 90% loss rate seems to vary from sample to sample, so post-growth quantifications of the doping will be important for the study of doping-dependent resistance fluctuations in LBCO. The close agreement of the PLD-grown films' narrow Meissner transitions with the superconducting phase diagram of LBCO indicates a high degree of sample quality.

4.3 Failure of multiple spectroscopic techniques and determination of doping

In addition to the indirect determination of doping from T_c, it would be useful to measure the dopant stoichiometry of our films directly, in order to quantify the sample-dependent rate of barium loss. An alternative explanation of the T_c's observed in Fig. 4.16 would be extreme dopant inhomogeneity. If we imagine taking an average of the $T_c(x)$ boundary

over a relatively large range of the doping x, an average T_c near $15-20$ K, like we observe in the PLD-grown films, might be plausible. We would like to confirm that the suppressed T_c's of the LBCO films are truly due to barium loss during deposition, and not due to severe inhomogeneity.

Unfortunately, many common spectroscopies used to measure stoichiometry are not applicable to PLD-grown LBCO films. X-ray photoelectron spectroscopy (XPS), is a technique in which x-rays are used to excite core electrons, which are ejected from the sample and whose kinetic energy is analyzed in an electron spectrometer. The observed electron binding energies are characteristic of the atoms in the top few nm of a sample, so integrated areas under observed peaks in electron energy can be used to compute surface stoichiometry. Unfortunately, the primary lanthanum L-α peak and primary barium L-α peak overlap, so this technique did not easily resolve barium content in LBCO. Secondary peaks are visible, but quantitative analysis is still complicated by other considerations. The thin, weakly conducting LBCO on an insulating substrate tends to charge during photoelectron emission, adding time-dependent changes to the measured electron energies. Rare earth metals have not been heavily studied by XPS, and reference spectra are usually unavailable. Finally, the fitting of slowly varying background contributions in XPS is critical for the computation of accurate peak areas and stoichiometry; this opens the possibility for large systematic error from the details of the fitting procedure.

Rutherford backscattering spectroscopy (RBS) is a technique independent from XPS, as it relies on the nuclear scattering cross-sections of alpha particles from a test material, rather than electron energy levels. Unfortunately, characteristic RBS energies of lanthanum and barium overlap, and initial tests on our films showed no features associated with Ba. RBS and other beam-based stoichiometric techniques with large interaction volumes also cannot distinguish between La in the film and La in the lanthanum aluminate substrate, so successful characterization would require careful comparison of LBCO films to reference samples. It should be noted that while techniques based on direct mass spec-

trometry of the sample could distinguish the small mass difference between barium and lanthanum and hence allow doping measurement, these techniques are destructive. Because T_c measurements had indicated a small degree ($\leq 10\%$) of sample-to-sample variation in doping, we sought a non-destructive stoichiometric technique in order to measure barium concentration before (or after) fabrication of films into microscopic devices for resistance fluctuation experiments.

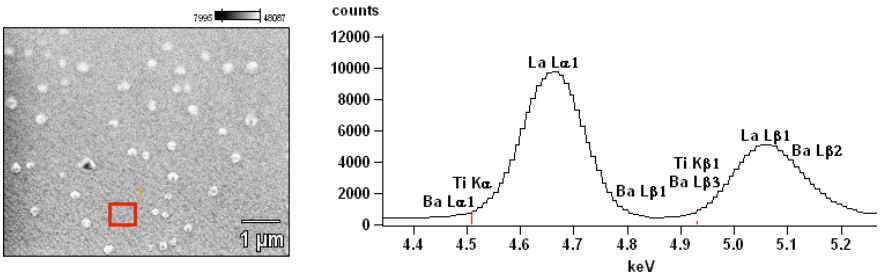

(a)

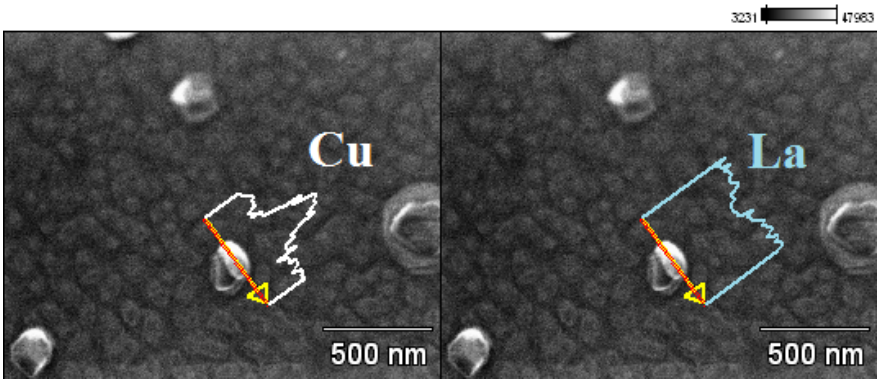

(b)

Figure 4.17: **Energy dispersive x-ray spectroscopy on a LBCO film (x= 0.095 target doping) grown on $SrTiO_3$** (a) SEM image of the film (left) and energy spectrum of emitted x-rays (right). Spectrum was acquired within the red rectangle highlighted in the image. Because this sample was grown on $SrTiO_3$, instead of the usual $LaAlO_3$, the La peak is caused solely by the film itself, which would permit calculation of doping if both La and Ba peaks are visible. Expected peak locations are labelled in the spectrum; the strongest Ba peak overlaps with the tail of the strongest La peak, so quantitative analysis isn't possible. (b) Line scan across a 3D crystallite on the surface of the same LBCO film. Peak x-ray intensities associated with Cu and La are respectively shown in white (on left) and light blue (on right), as a function of position. The La signal changes only slightly between the smooth film in the background and the crystallite, in contrast the Cu signal roughly doubles; the crystallite is a Cu-rich impurity phase.

LBCO films were also studied by energy-dispersive x-ray spectroscopy (EDS), which relies on excitation of a samples' atoms by high-energy electrons that drive emission of characteristic-energy x-rays associated with an atom's core electron energy levels. This microscopic process is the reverse of that occurring in XPS and, like XPS, EDS was unable to resolve La and Ba concentration due to peak overlap, as shown in Fig. 4.17(a). However, because EDS is spatially resolved, it was able to provide qualitative information on the nature of the large crystallites observed in AFM images of some of our LBCO films (see Fig. 4.9 or 4.13, for example). In Fig. 4.17(b), line scans of copper and lanthanum EDS signals are shown across the surface of a crystallite found on a LBCO film deposited on $SrTiO_3$ substrate. The STO substrate is not lattice-matched to LBCO, but ensures that any La, Ba, or Cu EDS signals do not come from the substrate. The crystallite is found to have roughly twice the Cu content of the rest of the film, compared to La.

This stoichiometry could be satisfied by a $LaCuO_3$ phase, which was also found as a slight impurity phase in the XRD study of LBCO powders and pellets (Section 4.1). Therefore, it is believed that $LaCuO_3$ is the primary impurity phase found in our LBCO films, in the form of 3D crystallites on the film surface. In the minority of films whose $2\theta - \omega$ XRD surveys showed unexpected impurity peaks, some of these peaks were close to $LaCuO_3$ diffraction peaks, consistent with the EDS result. Because the impurity phase is not interspersed with the 2D LBCO film, but rather nucleates in three-dimensional structures (which may not even penetrate the underlying LBCO film), it is doubtful that these impurity crystallites will have a strong effect on transport results, such as the resistance fluctuation spectra.

It is not necessarily true that *all* crystallites or surface particles in the LBCO films are $LaCuO_3$ impurities. Many reports on cuprate film growth have suggested the presence of three-dimensional growth modes. The formation of LBCO into three-dimensional clusters is seen, for example, in our films grown at low laser energies (Fig. 4.9(a)), which still have XRD patterns dominated by the expected La-214 phase. We also observe large

sample-to-sample variations in the number density of particulates at optimal growth conditions. The formation of molten droplets during laser ablation, which is sensitive to the somewhat-variable polishing of the PLD targets, could explain this variation. In contrast, if the typical crystallite were thermodynamically favored impurity phase (as $LaCuO_3$ was in the LBCO powder study), then it would likely form at a consistent rate for all samples. We believe that the large particulates found in some LBCO films are a mixture of LBCO outcroppings that are still c-axis oriented, and a crystalline $LaCuO_3$ impurity phase.

4.4 Hall effect as a measurement of doping

Hall effect measurements, performed at fields up to 9 T in the PPMS system, were an additional explicit confirmation of the dopant difference between films grown from different targets. The Hall coefficient is measured as $R_H = V_H t/(IB)$ for a transverse voltage V_H and film thickness t with applied current and field I and B. As depicted in Fig (a), the transverse voltage is induced by the motion of the charge carriers subject to the Lorentz force, and therefore give a Hall coefficient $R_H = 1/(nq)$, proportional to carrier density n and the sign and magnitude q of the carrier's charge.

The simplest possible Hall device is shaped like a cross, allowing a single voltage to be measured perpendicular to an applied current. In comparison, the more complex device geometry fabricated from LBCO, shown in Fig (b), provides additional information. The flow of current along two perpendicular directions through the L-shaped device allows explicit confirmation that the Hall coefficient depends only on carrier density, not in-plane orientation of the current flow or Lorentz force. The four voltage contacts on each perpendicular section of the device enable the comparison of the Hall coefficient measured at each cross-shaped intersection. The additional voltage contacts also allow simultaneous measurement of the longitudinal magnetoresistance $R_{xx}(B)$ along with the Hall coefficient.

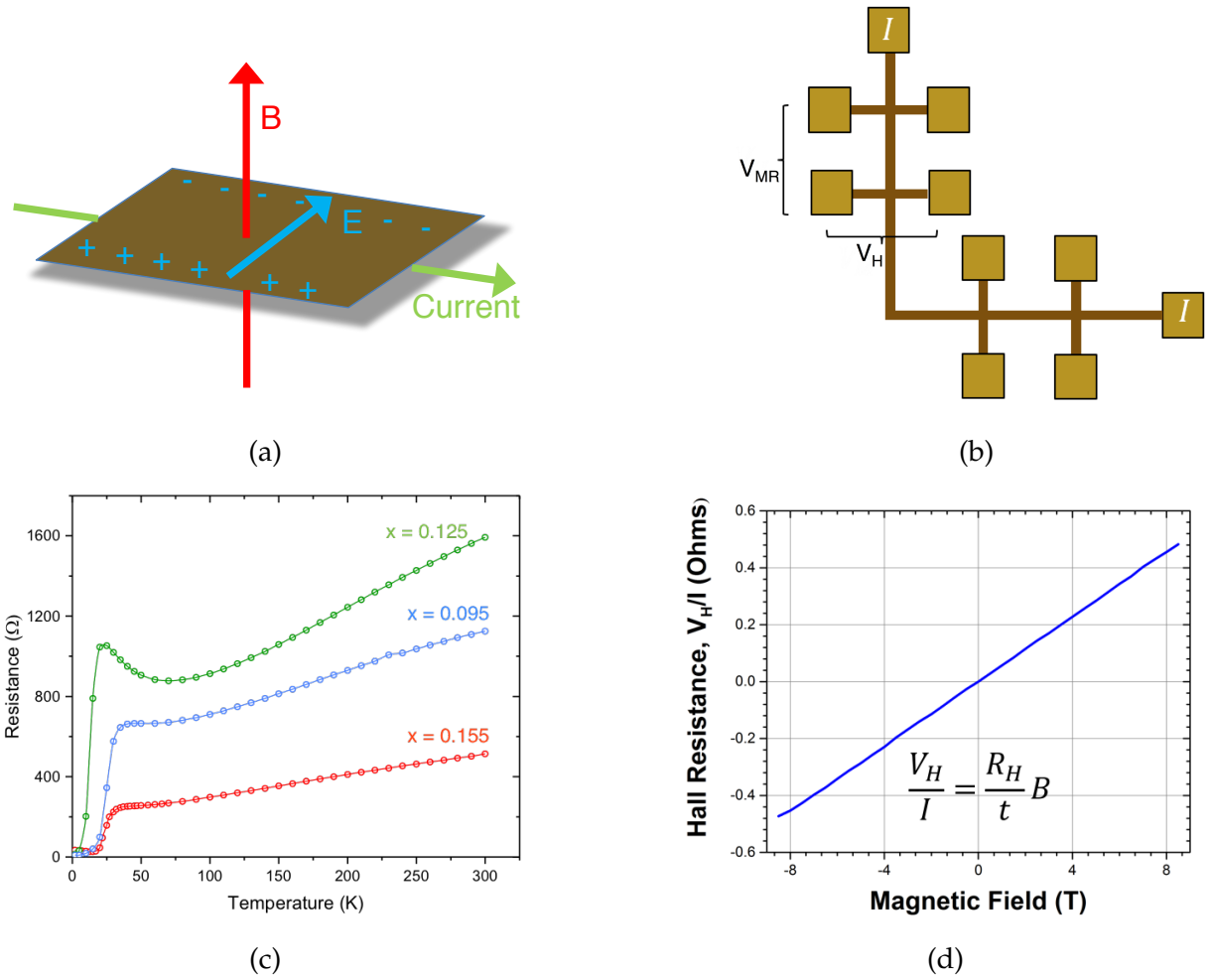

Figure 4.18: **Hall effect for measurement of carrier density.** (a) Illustration of the Hall effect: when current I flows through a lamellar conductor in perpendicular magnetic field B, the Lorentz force on the moving charge carriers pushes them towards the edge of the conductor, creating a transverse electric field E (voltage V_{H}) perpendicular to both I and B. (b) Schematic of the Hall devices fabricated in LBCO films, which also allowed simultaneous measurement of LBCO's longitudinal magnetoresistance (voltage V_{MR}). (c) Resistive superconducting transitions (zero-field longitudinal resistance) for three representative samples discussed here. The curves are labelled with the doping x of the deposition source used to grow each film, which is not necessarily the doping of the film itself. (d) As expected for the Hall effect, the transverse resistance is linear in the magnetic field B. The positive slope of this line confirms that the hole-doped compound LBCO has mostly positive charge carriers.

The superconducting transitions of three LBCO Hall devices, one deposited from each doping of target, are shown in Fig (c), with T_cs consistent with other T_c measurements in our PLD-grown films. At constant current, the measured transverse voltage V_{H} is ob-

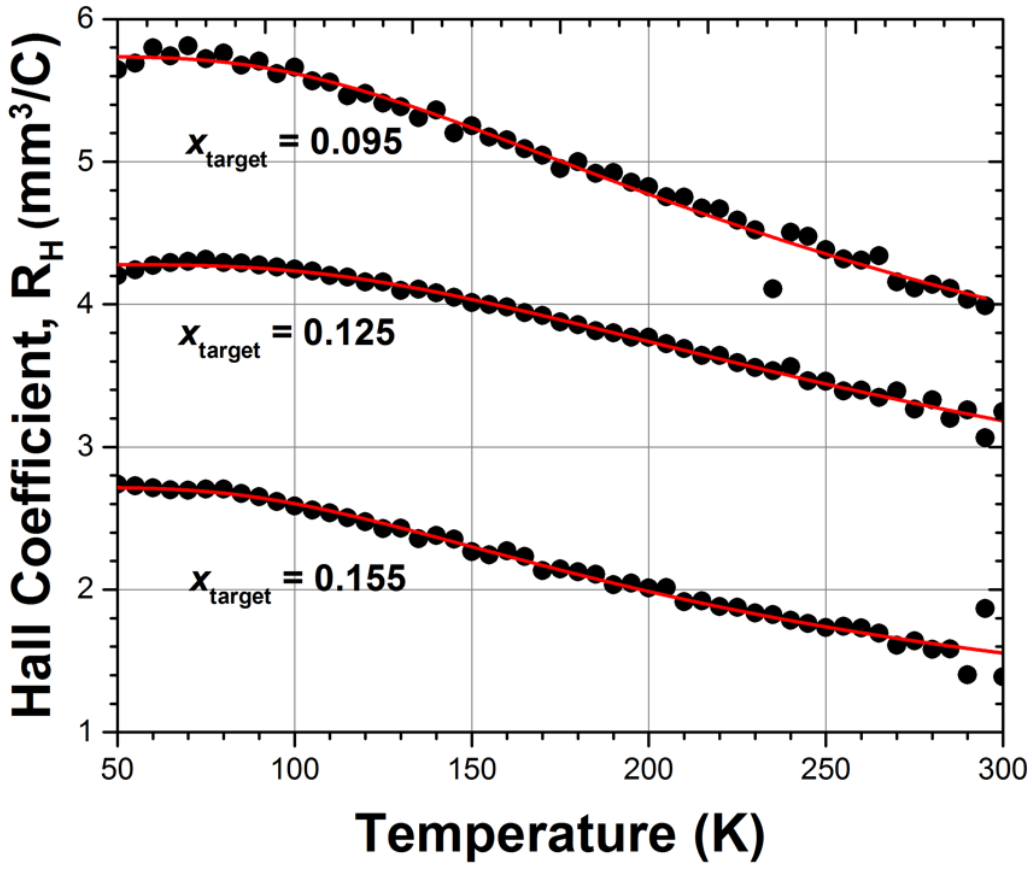

Figure 4.19: **Hall coefficient of thin film LBCO grown from three PLD targets of different nominal dopings.** Black points are data, red curve is fit to a simple model of constant chemical dopings plus some thermally activated doping. Films grown from low-doping targets have higher Hall coefficient, which is to be expected since Hall coefficient is inversely proportional to carrier density.

served to be linear with applied magnetic field B (Fig (d)), confirming that it is caused by the Hall effect. The positive slope of this linear behavior implies positive charge carriers, consistent with the hole-doping of LBCO. In this experiment we observed that Hall coefficients did not vary significantly with location on the device, or with in-plane current orientation. Additionally, the measured Hall coefficients were independent of applied current, so the results should not be affected by ohmic heating of the devices.

In LBCO devices, we find a Hall coefficient whose magnitude varies with temperature and doping as shown in Fig. 4.19. The shape of the R_H-versus-T curve is consistent with other measurements of the temperature-dependent Hall effect in cuprates [104]. Hall

coefficients are higher for samples grown at low dopings. The inverse relationship of R_H to n suggests that such films grown from low-x targets do indeed have lower dopings. In other words, the doping of our films are influenced by the doping of the source PLD targets. The clearly distinct Hall coefficients suggest that the T_c's between 15 and 25 K in our films are not caused by extreme dopant inhomogeneity, but rather are consequences of specific homogeneous dopings subject to barium loss relative to the deposition source.

We can attempt to determine more quantitatively the doping x from the Hall coefficients R_H; to do so, we must account for the non-trivial temperature dependence of R_H. One plausible model for $R_H(T, x)$ is described in S. Ono et al.'s work on LSCO Hall devices, where carrier density is described as a chemically doped contribution, equivalent to x, plus a thermally activated contribution described by a single band gap. Then the Hall coefficient can be described by the equation

$$R_H\left(T, x\right) = \frac{V_{\mathrm{Cu}}}{e}\left(\frac{1}{x + n_1 e^{-\Delta_{CT}/2k_BT}}\right), \tag{4.1}$$

where V_{Cu} is the volume per copper atom, e is the charge of the electron hole, and n_1 and Δ_{CT} are fit parameters. The gap Δ_{CT} is unrelated to the superconducting gap.

Coefficients from our LBCO Hall devices were fit to equation 4.1, with the fit results shown as solid red curves in Fig. 4.19. Clearly, the LBCO data is accurately modeled by chemical doping with thermal activation of carriers. For films grown from x =0.095, 0.125, and 0.155 targets, the fit respectively finds x =0.103, 0.138, and 0.217 in the measured devices. The value of x from the fit in equation 4.1 tends to overestimate the carrier density relative to the nominal doping of the deposition source, and the fit is an even greater overestimate relative to the barium-deficient films. This discrepancy is probably caused by the fact that, in cuprates, the shape of the Fermi surface is strongly doping dependent, which creates nonlinearities in the actual carrier density as a function of doping. Therefore, although the relationship between Ba-content and carrier density is

monotonic, it is not the identity function. While the Hall effect provides a useful qualitative description of doping in our LBCO films, it cannot be used to quantitatively extract the actual barium concentration after film deposition.

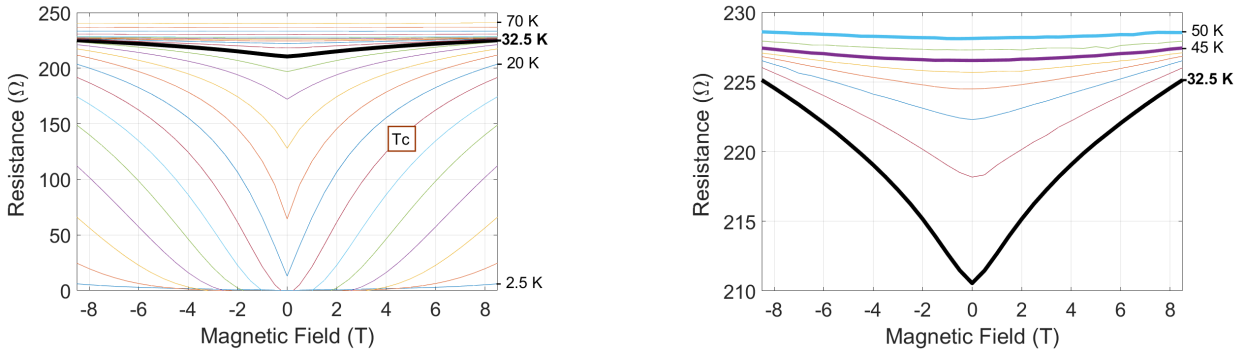

(a) (b)

Figure 4.20: **Magnetoresistance in $La_{1.862}Ba_{0.138}CuO_4$ device.** (a) Temperatures above and below $T_c = 17$ K. (b) Plot focused on temperatures above T_c. Resistance was measured at several temperatues during a bipolar field sweep. LBCO has the typical superconducting behavior that T_c is suppressed at higher field, so resistance increases with field at $T < T_c$. Surprisingly this behavior persists continuously above T_c, and even above 32.5 K (bold line), the highest possible T_c of LBCO. This large above-T_c magnetoresistance effect was not explored in much detail, but could potentially be explained by the presence of Cooper pairing (and a possible pair density wave state) at $T > T_c$ and $x \sim 1/8$.

In addition to Hall coefficients, the Hall device experiment also measured magnetoresistance, the field-dependent voltage along the direction of current flow, divided by the applied current. For one $x = 0.138$ device, with doping determined from T_c and the Hall effect, the measured magnetoresistance for several temperatues is plotted for the entire -9 T to 9 T field range. As is typical for a superconductor, higher fields suppress T_c and therefore increase resistance at low temperatures. However, this sensitivity of the resistance to magnetic field is also observed to persist well above T_c, and even above ~ 32 K, the highest possible T_c for unstrained LBCO. The variation in resistance R with field B at $T < T_c$ is caused by the suppression of Cooper pairing, and in this case, the measured $R(B)$ curves appear to vary continuously with T. The large magnetoresistive effect we observe in LBCO at T *above* T_c could then be qualitatively explained as magnetic field

possibly breaking incoherent Cooper pair fluctuations that contribute to conductivity at $T > T_c$ and low B. This is quite speculative, and isn't explored further in this dissertation. Additional experiments would be required to fully determine if LBCO near $x = 1/8$ has anomalously high magnetoresistance due to such an incoherent superconductivity, or pre-formed pair scenario. However, the LBCO films' large magnetoresistive effect — and an explanation based on fluctuating or frustrated superconductivity — is similar to other reports in single-crystal LBCO [105, 106].

4.5 High-resolution x-ray diffraction to measure doping

An alternative technique for measuring the doping x in $La_{2-x}Ba_xCuO_4$ thin films was developed based on high-resolution x-ray diffraction, inspired by early work on thin LBCO films by Hisashi Sato [107]. Sato's LBCO films were grown by electron beam co-evaporation, a technique similar to molecular-beam epitaxy. Prior to this thesis, the Sato work was possibly the only published example of thin-film LBCO. Rather than seeking to replicate the bulk phase diagram of LBCO, as we have done with our PLD-grown films, Sato deposited LBCO on lattice-mismatched substrates and observed the strain-dependent phase diagram of Fig. 4.21(a). On $SrTiO_3$, LBCO experiences tensile epitaxial strain, and has low T_c's with a wider region of $T_c = 0$ near $x = 1/8$. On $LaSrAlO_4$, LBCO experiences compressive strain and has high T_c's with no $x = 1/8$ anomaly.

The bulk lattice parameters of LBCO, measured by x-ray diffraction, vary slightly with doping as shown for polycrystalline samples [86] in Fig. 4.21(b); this is common for substitutionally doped materials. Sato observed that in epitaxial LBCO thin films, the in-plane lattice parameter is equal to the substrate lattice parameter, regardless of doping. However, the c-axis lattice parameter still varies monotonically with doping, with a slope that depends on the substrate used. His lattice data is summarized in Fig. 4.21(c). Since Sato demonstrated that LBCO's T_c is highly dependent on epitaxial strain, and since we

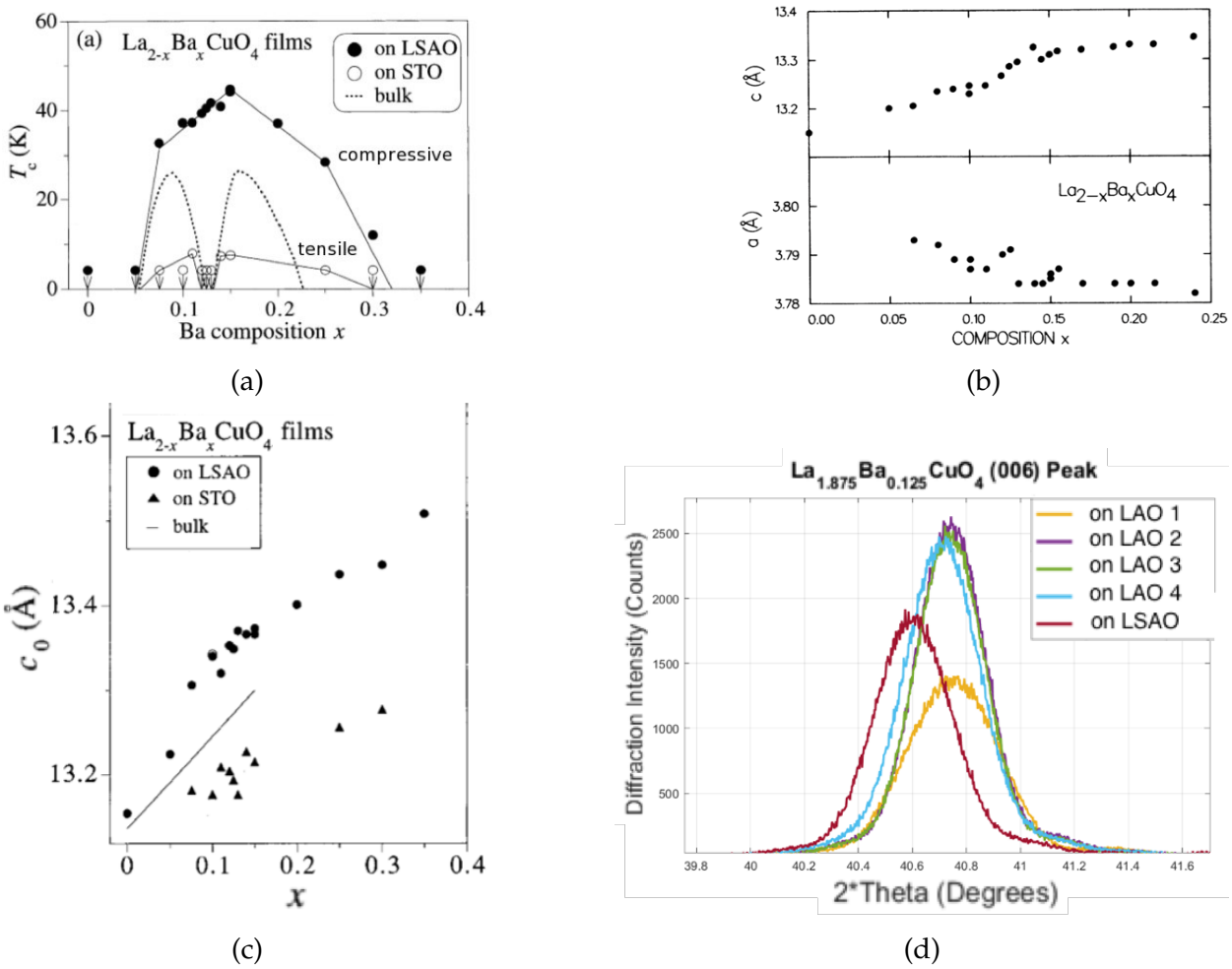

Figure 4.21: **Measurements of LBCO's doping-dependent lattice parameters by x-ray diffraction.** (a) Phase diagram of epitaxially strained LBCO films, measured by Sato et al. [107]. (b) In polycrstalline, bulk LBCO, both the in-plane lattice parameter a and the out-of-plane parameter c vary monotonically with doping x. From [86]. (c) In Sato's strained films, a is fixed, but c is still monotonically increasing, with a substrate-dependent slope. (d) $2\theta - \omega$ x-ray diffraction scans of the (006) peak for several $La_{1.875}Ba_0.125CuO_4$ films deposited in similar conditions. All films were codeposited by PLD from $x = 0.125$ and $x = 0.155$ targets, such that the film doping after barium loss was predicted to be $x = 0.125$ exactly. One sample (red curve) was intentionally strained by depositing on $LaSrAlO_4$ substrate, all others are on $LaAlO_3$. Peak shifts, whether caused by sample-to-sample doping variation or intentional strain, are small (much less than peak width).

observe that our films have T_c similar to bulk, we anticipate that they are not strained relative to bulk LBCO. Our PLD-grown LBCO films should have the same monotonic variation of the lattice parameter c with doping as observed in bulk LBCO. If an x-ray ex-

periment determines c with sufficient precision, then we can use c to deduce the doping x using the curve in Fig. 4.21(b).

Measuring the out-of-plane lattice parameter c with this degree of precision is not necessarily straightforward. Note that our range of interest for doping, roughly $x = 0.07$ to 0.15, is small compared to the datasets in Fig. 4.21; we are seeking to track changes in c to the few-picometer level. To illustrate this difficulty, a few $2\theta - \omega$ x-ray diffraction scans of the LBCO (006) are shown in Fig. 4.21(d) for several films of identical nominal doping. One of these samples was intentionally strained by growing it on $LaSrAlO_4$, the same mismatched substrate used by Sato. The peak shift induced by this strain is smaller than the peak breadth (which is primarily caused by finite detector width and the thinness of the film).

The high-resolution x-ray diffraction measurements used to determine c (and hence doping) were performed in conditions similar to the survey $2\theta - \omega$ scans described in Section **??**. In addition, in order to improve angular accuracy, a 0.1° collimation slit was added to the x-ray source, and only a single "pixel" of the multi-pixel line detector was used. Particular care was taken with initial alignment of the sample stage relative to substrate diffraction peaks, in order to minimize systematic misalignment errors. Further optimization of the measurement may be possible in a dedicated high-precision diffraction system, but was not possible with the shared equipment used here. Measured c-axis diffraction peaks were fit in commercial software (JADE) to a Pearson VII function (modified Lorentzian peak).

Recall that the Bragg condition $n\lambda = 2d\sin\theta_n$ produces a *series* of peaks at Miller indices $(00n)$ for a given lattice spacing d. n is a natural number and $\lambda = 1.54056\mathring{A}$ is precisely known for Cu K-α radiation, permitting $c = d$ to be calculated from θ_n, the angle reported by the Pearson VII fit to each peak. This allows for a distinct measurement of the lattice spacing c for each n. In principle, these somewhat-independent measurements of c in a single sample should agree. However, in practice we must consider how to best

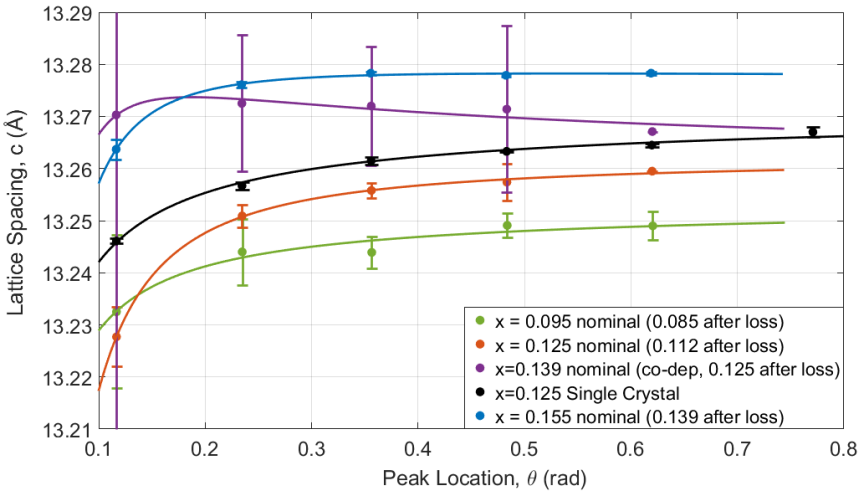

(a)

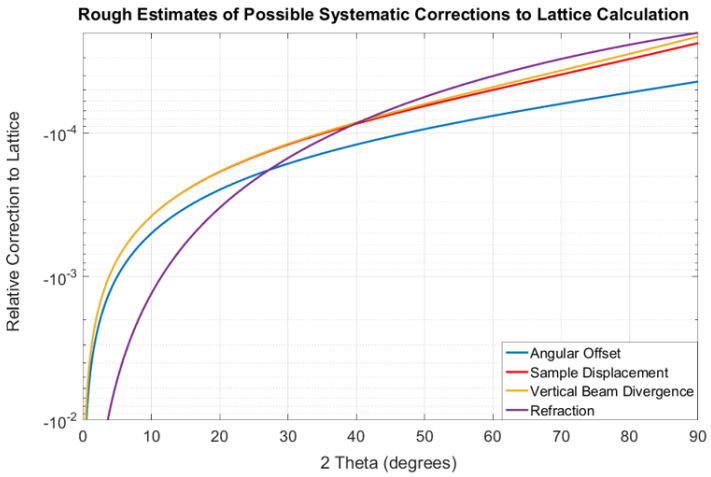

(b)

Figure 4.22: **Lattice parameter c varies somewhat with peak index/angle.** (a) Measured lattice parameter c from diffraction, for PLD-grown films of various doping. Depending on which peak is used in the Bragg condition calculation, the value of c varies for a single sample (data points with error bars). This variation may be fit by a model (solid curve) of systematic error in the diffraction measurement. Lattice parameter does appear to vary monotonically with doping, as expected. Single crystal reference sample was obtained from Genda Gu (Brookhaven National Lab). (b) Estimation of relative correction to lattice parameter for several types of systematic diffraction error, using realistic input parameters for our diffraction instrument. All errors are more significant at lower angles. Except refraction, all may have either positive or negative sign. In this work, the systematic variation of c with θ was fit to a combination of sample displacement and refraction.

combine the different results. Simply averaging the values for $c(n)$ seemed too simple, because as shown in Fig. 4.22(a), the variation in c with n appeared to be somewhat

systematic, rather than random. Measurements of c at the low-angle (002) peak appeared to consistently underestimate the lattice spacing compared to estimates from higher-angle peaks; the same is true to a lesser extent for the (004) peak.

Several x-ray texts explore what might cause this type of systematic error at low angles [108, 109, 110]. Candidate causes include angular offset of the source or detector, displacement of the sample, divergence of the beam, and refraction of the x-ray radiation within the sample. Unfortunately, most of these systematic errors have nearly indistinguishable functional variation with θ, as shown in Fig. 4.22(b). Therefore, while fitting $c(n)$ or $c(\theta)$ to one of these error functions is probably more accurate than averaging $c(n)$ over all n, this fit will not uniquely describe what the actual source of error was. For this work, I chose to fit to an displacement + refraction error function

$$\frac{\Delta c}{c} = \frac{-D\cos^2\theta}{R\sin\theta} + \frac{-(1-n_{\text{ref}})}{\sin^2\theta}, \tag{4.2}$$

where D is the displacement from the diffractometer axis (displacement along film normal), R is the radius of the diffractometer (source-to-sample distance), and n_{ref} is the index of refraction; for x-rays, $1 - n_{\text{ref}} \sim 10^{-5}$ typically. This fit was chosen because it seemed a plausible cause of error in our diffraction system, and because the fit had the potential to explain non-monotonic variation in $c(n)$, which was observed measurements of some samples (e.g. the nominal $x = 0.139$ film in Fig. 4.22(a)). Whether this systematic error analysis is used, or $c(n)$ is simply averaged over n, the reported values vary only by $0.01\mathring{A}$, at most. The discussion of systematic diffraction error is included here because it appears to describe the data, but even without its inclusion the high-resolution diffraction technique is precise enough to measure doping.

In Fig. 4.22(a), the plot legend lists samples in order of increasing doping. Without exception, higher-doping samples have higher measured lattice spacing c, as expected for LBCO's monotonic variation of c with x described in Fig. 4.21(b)-(c). For each of the

samples shown in Fig. 4.22(a), the bulk data in Fig. 4.21(b) may be used to deduce x from c. For nearly all of the samples studied, this value of x, deduced from high-resolution x-ray diffraction, usually agrees to within a few percent with the value of x suggested by T_c. In other words, the high-resolution x-ray diffraction measurement described here appears to accurately measure the doping of an LBCO film in a non-destructive way, with few-percent precision sufficient to predict T_c and other behavior.

Chapter 5

Noise Spectroscopy of Microscopic LBCO Wires

5.1 Basic properties of the observed resistance fluctuations

After growth of an LBCO film, it is microfabricated into a 2-4 μm wide and 10-15 μm long wire whose resistance noise properties are measured at various temperatures and bias currents. If voltage is measured over a period of time, noise is clearly observable in LBCO devices biased by finite DC current (Fig. 5.1). One preliminary LBCO $x \sim 0.11$ microwire sample showed an extremely large increase in its low-frequency resistance noise below 45 K, which suggests a critical noise-onset temperature comparable to the charge-ordering temperature expected from the LBCO phase diagram. At higher current bias, a sharp increase in the observed noise still occurred near 45 K, but the change in the amount of noise was lesser. Most of the other LBCO wires discussed below behave instead like that of Fig. 5.1(c), with noise that evolves gradually with temperature and has power-law (quadratic) current scaling.

The $x = 0.11$ LBCO wire with anomalously large resistance fluctuations (Fig. 5.1(a)-(b)) may be caused by an inhomogeneous sample with a strongly pinned striped state. As current is increased, charge stripes may preferentially orient parallel to the higher electric field, effectively pinning the stripe direction and reducing relative resistance noise. This could explain the relative weakening of the noise as current is increased and is similar to the current-hysteretic effects described in simulations [42, 61] of charge-ordered cuprates and at least one experiment on untwinned YBCO [54]. However, this non-linear behavior with current was only observed in this one early sample, which was grown from an

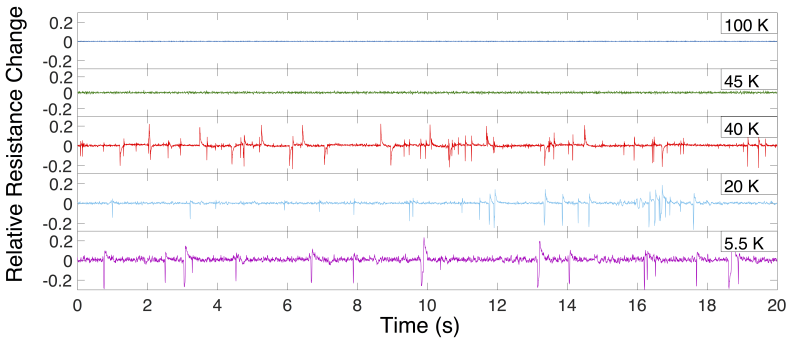

(a)

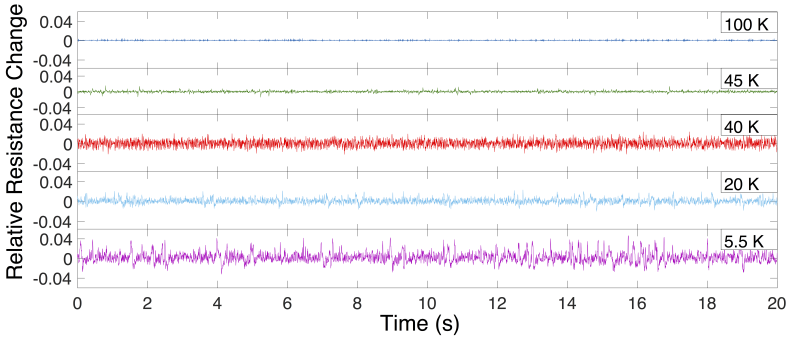

(b)

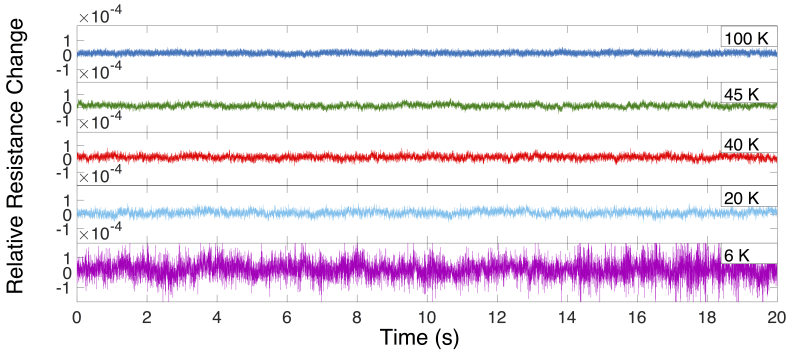

(c)

Figure 5.1: **Example traces of time-dependent voltage fluctuations in LBCO microwires** (a) One early LBCO wire with an estimated doping $x \sim 0.11$ showed a very sudden increase in noise upon cooling from 45 K to 40 K at low bias ($\sim$2 µA here); further cooling increases the relative size of observed voltage fluctuation events (b) The same $x \sim 0.11$ sample at higher bias ($\sim$14 µA). Cooling still increases noise, but now the increase in noise near 40 K is less extreme. (c) Noise of a $x \sim 0.14$ sample at much higher bias ($\sim$328 µA). Note the significantly smaller scale of the voltage noise and the more gradual variation in noise with temperature. It is still generally true that LBCO becomes noisier at low temperatures.

early solid-state-reacted PLD target, and therefore had significantly higher inhomogeneity than typical homogeneous samples grown from the metalorganic-synthesized targets. Reduced sample quality was evident in this samples $R(T)$ transition, which begins at $T_c \sim 15$ K and only drops to half of the above T_c resistance. In such an inhomogeneous sample, pinning of stripes to the current direction may be easier as there is already strong stripe pinning to disorder. The anomalously large size of the resistance fluctuations, $\sim 10\%$ of the DC resistance, may also be described by sample inhomogeneity. The resistance anisotropy of the strongly pinned stripes, along with the spatial variations in the sample's resistivity, may cause extremely inhomogeneous current paths where current is "focused" into a few hotspots where charge order fluctuations have a disproportionate effect on the time-varying voltage. This would explain why the characteristic noise of the $x = 0.11$ sample was large fluctuation events that resemble the filtered telegraph noise of a two-level fluctuator, even though the sample is significantly larger than the characteristic size of a stripe domain. This large fluctuation behavior with possible current pinning is suggestive of a stripe state, but later samples usually appeared to be in a "many fluctuator" state, and did not have such obvious noise events amenable to qualitative interpretation. For noise data like that of the $x \sim 0.14$ sample in Fig. 5.1(c), careful quantitative analysis is required.

The *power spectral density* - the mean squared magnitude of the Fourier transform of the time varying voltage signal can be computed from the raw noise data, and some representative examples are shown in Fig. 5.2. The overall magnitude of the noise varies with temperature and bias current, but is generally close to $1/f$ frequency scaling throughout. Non-$1/f$ behavior is observed most commonly at low current biases in low-noise samples, such as the blue PSD curve in Fig. 5.2(a). Compared to other devices, this LBCO $x \sim 0.12$ wire had a relatively low resistance, $\sim 500\,\Omega$ at room temperature, and is therefore less noisy. Resistance fluctuations are likely still present at low DC current, but are difficult to resolve above the $1/f^2$ amplifier noise visible at low frequencies, and white

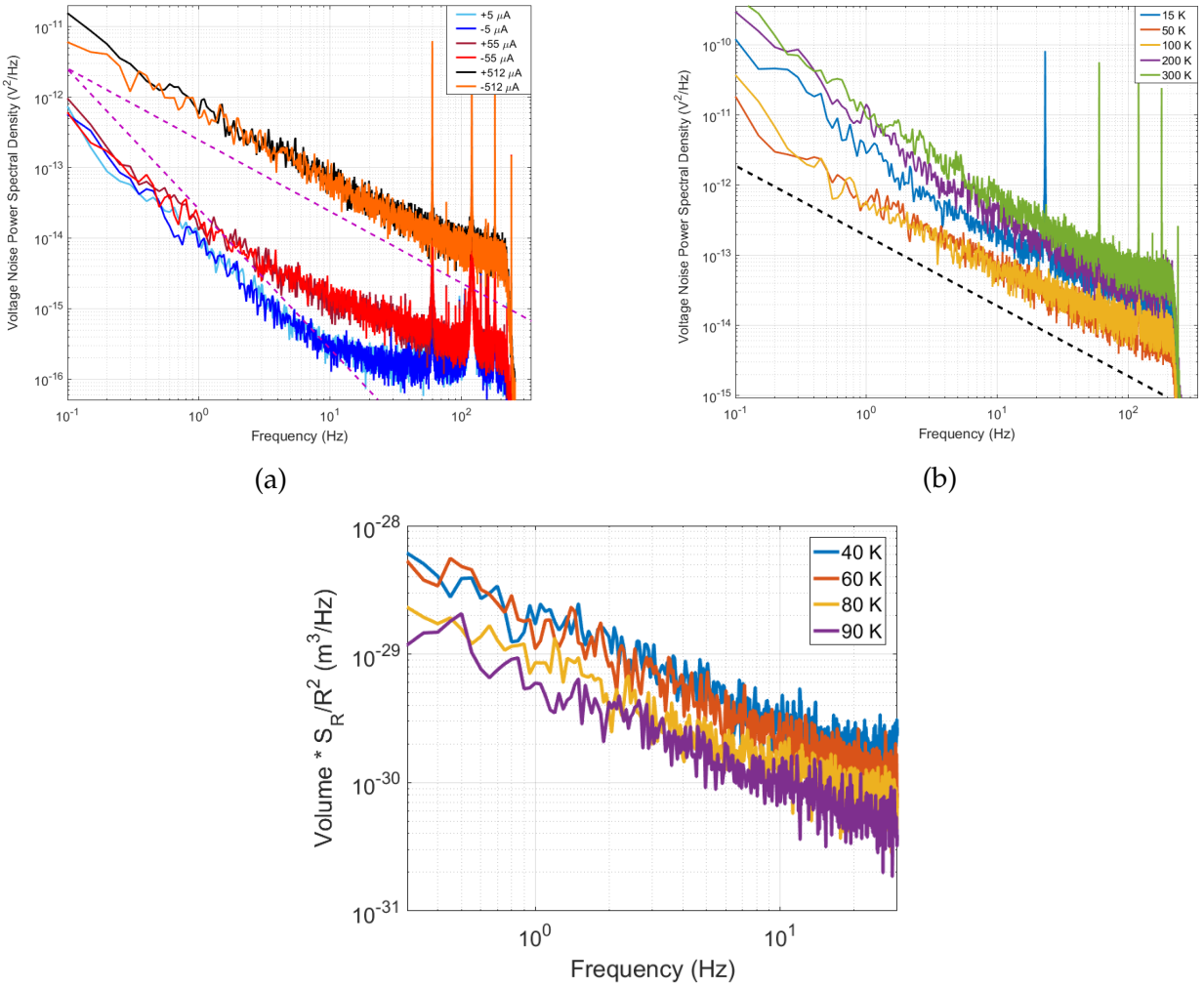

Figure 5.2: **Example power spectra of fluctuations in LBCO microwires.** (a) A few noise spectra from a LBCO $x \sim 0.12$ device measured at 40K. Dashed lines indicate $1/f$ and $1/f^2$ behavior. As current is increased, noise goes from a combination of $1/f^2$ (amp noise) and Johnson noise at low currents, to clear $1/f$ behavior. Polarity of the DC current has no effect on the noise. (b) Spectra from the same $x \sim 0.12$ sample at high current bias (512 µA), for a few measurement temperatures. Noise (at sufficient bias) is $1/f$ at all temperatures, and is somewhat temperature dependent. Typical samples are noisiest at both the lowest ($\sim$ 5-10 K) and the highest ($\sim$ 300 K) measured temperatures, with a noise minimum somewhere in between ($\sim$ 100 K typ.). (c) $1/f$ noise spectra in the $x \sim 0.14$ sample, at 46 µA bias, for a few temperatures near the expected charge ordering transition temperature. Temperature evolution is relatively gradual, no sudden "jump" in the noise at a particular critical temperature.

Johnson-Nyquist noise visible at high frequencies. As current is increased, it becomes visible above the background noise level, and at the highest currents, $1/f$ behavior dom-

inates.

At currents high enough to resolve $1/f$ noise, temperature evolution of the noise can be studied. In particular, we would like to see if LBCO wires generate additional resistance noise in the charge-stripe state. Representative spectra for a few temperatures is shown for the $x \sim 0.12$ sample in Fig. 5.2(b). Most samples have high resistance-fluctuation noise near room temperature, which decreases upon cooling as single-electron fluctuator states begin to "freeze out." At some point below 100 K, noise will generally begin to increase again, or will at least increase in comparison to the background temperature evolution extrapolated from high temperatures. At $T < T_c$, noise may increase significantly due to the entry of vortices into the thin LBCO film. The $x \sim 0.12$ sample had a resistive transition between about 15 K and 5 K, and is partially superconducting at 10 K. The 10 K noise spectrum in Fig. 5.2(b) (blue curve) shows enhanced noise which may originate from the discretized flow of vortices through the device at high currents. This particular spectrum may deviate slightly from $1/f$ scaling; in general, noise spectra in the vortex state had a variety of spectral shapes.

Additional spectra for a $x \sim 0.14$ sample are shown (Fig. 5.2(c)) near temperatures where a charge-ordering transition was expected. A subtle increase in the noise occurs as temperature is lowered, in particular from 80 K to 60 K, but the noise does not change as drastically as, for example, the sudden increase at 40 K for the sample shown in Fig. 5.1(a). The comparatively soft onset of possible charge-ordering noise in the $x \sim 0.14$ device may partially be a symptom of its doping. For example, in neutron scattering experiments [31] on LBCO with doping near 0.155, the peak intensities associated with the stripe-ordered state was found to increase slowly below 55 K. It may possible that at high dopings, the low-temperature stripe state is bounded by more of a crossover than a sharp phase transition. However, in our LBCO wires, noise variations near the charge-ordering transition were consistently observed to be slowly-varying, even at low dopings where scattering experiments have shown sharper transitions.

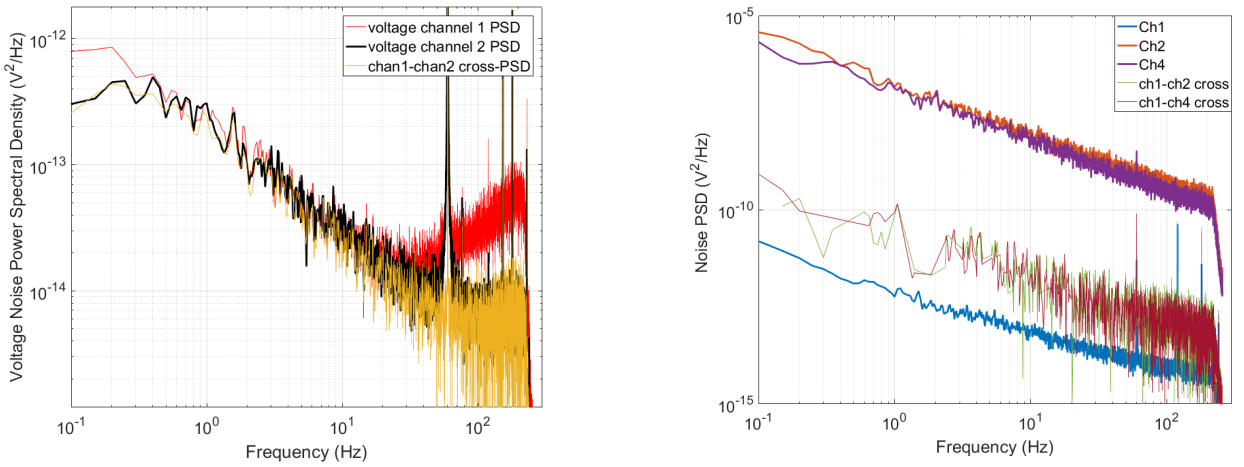

(a) (b)

Figure 5.3: **Comparison of single-channel PSDs to cross-correlated power spectra.** (a) Correlation of two parallel voltage channels in the $x \sim 0.14$ device at 60 K with 86 µA current. Channel 1 has anomalous high-frequency noise, that was later found to be caused by a faulty amplifier power supply. Cross-correlation of the two channels effectively removes this excess noise because it was present on only one channel. (b) Correlation of dissimilar signals in a $x \sim 0.12$ device at 40 K and 512 µA bias. Voltage channel 1 is a true 4-terminal measurement and should be dominated by fluctuations in the narrow LBCO wire, while channels 2 and 4 are two-terminal measurements including a highly fluctuating contact resistance. Cross-correlation between channel 1 and channel 2/4 gives a PSD that is close to, but higher than the single-channel PSD of the device, which is unphysical. Numerous negative points in the cross-PSD curves are omitted. Large uncorrelated noise sources can still "contaminate" the cross-PSD for insufficiently averaged datasets. The PSDs of 15 ten-second time traces were used to create these spectra.

As discussed in section 3.5, redundant amplifier channels and cross correlation may be used as a statistical technique to reject uncorrelated noise sources, such as noise voltage in the amplifier itself. Some illustrative examples of cross-correlation techniques applied to noise in the LBCO wires are shown in Fig. 5.3. Cross-correlation tends to be most effective for two signals which are statistically similar, but are each slightly corrupted by a small amount of uncorrelated noise. Such an example of two mostly-correlated signals is shown in Fig. 5.3(a). One of the two AC amplifier channels set to measure the same length of $x \sim 0.14$ wire experienced anomalous noise at higher frequencies due to a malfunction in the power supply of the DC amplifier connected to the same voltage-sensing leads. Cross-correlation was able to exclude this excess single-channel noise and reproduce the

noise of the LBCO wire alone. For this measurement at high bias current, noise of the AC preamps was negligible compared to that caused by resistance fluctuations.

However, cross-correlation is not universally applicable or useful. in particular, it can produce misleading results when one of the two signals has a source of uncorrelated noise that is significantly larger than the shared source of correlated noise. After fabrication of the $x \sim 0.12$ LBCO microwire device, it was observed that some of the device's on-chip leads had become open circuits; preventing the connection of two independent 4-terminal resistance channels. Instead, fluctuations were recorded in one four-terminal resistance channel (Ch 1) and a couple of pseudo-two-terminal resistance channels (Ch 2 and Ch 4). For the pseudo-two-terminal signals, current and voltage connections were shared the same contact pad on the LBCO chip, but were otherwise distinct. Ch 2 and Ch 4 therefore may be influenced by any fluctuating interfacial resistance between the gold contact pad and underlying LBCO, and any fluctuating thermoelectric voltages associated with this interface. As shown in Fig. 5.3(b), the two-terminal channels had significantly higher noise than the true four-terminal channel, so this "contact noise" was significant.

Cross-correlation between Ch 1 and Ch 2, or Ch 1 and Ch 4, *qualitatively* suggests that the large noise source shared by Ch 2 and Ch 4 was not present in the Ch 1 signal. Specifically, many points in the cross-correlated spectra were negative, suggesting random relative phase between the Fourier transforms of the 4-terminal and 2-terminal signals. Additionally, the cross-power spectra (red and green curves) are close to the lower-noise single-channel PSD of the four-terminal signal. However, for many frequencies, the calculated cross-PSD is actually higher than Ch 1's single-channel-PSD, so the cross-PSD cannot be interpreted physically as "only the correlated part of the Ch 1 noise." Channel 1 is probably uncorrelated to the large fluctuation source common to channel 2 and 4, but the cross-PSD is still influenced strongly by the uncorrelated noise source because it is so much larger than the correlated noise. If we naively interpreted the cross-PSD as the device's true resistance fluctuation signal, we would get inaccurate results influenced

primarily by noisy thermoelectric or contact resistance effects unrelated to the stripe state.

This occurs because our spectra are averaged over only a small number of repeated experiments, typically 15-20 spectra each computed for a 10 s time trace; with sufficient averaging of repeatedly measured spectra, cross-correlated signals should eventually converge to the true correlated spectra, even if large uncorrelated sources are present. However, for the small amount of averaging performed here, any spurious correlation that occurs for any particular finite data set may dominate the cross-PSD. In general for two partially correlated random signals with typical amplitudes A and B, such that $B \gg A$ due to an additional uncorrelated noise source, cross-correlation will only give an accurate representation of the true correlated signal if the number of averages N satisfies $\sqrt{N} \geq B/A$. For the example in Fig. 5.3(b), this would necessitate averaging thousands of spectra, significantly more than the 15 repeated time traces used to compute our spectra.

Qualitatively, the examples of cross-correlation shown above suggest we are able to resolve a correlated $1/f$ noise source in LBCO microwires, and that this signal is not usually, for example, washed out by noisy amplifiers. Our detection threshold for resistance noise is probably sufficient to observe any dynamics associated with a striped state. It was decided however, not to use cross-correlation for further quantitative studies of noise in LBCO films due to possibly misleading results like that discussed in Fig. 5.3(b). Despite the design intention to have duplicate voltage channels in all LBCO devices, most of the wires fabricated here did not have adequately "equivalent" pairs of channels, if they had multiple 4-terminal resistance channels at all. The 8-terminal microwires fabricated as in section 3.14 often did not yield 8 robust conducting contacts; noise measurement were performed on any superconducting sample with at least 4 intact contacts for which four-terminal resistance could be measured. The low yield of individual device leads is likely caused by a combination of the relatively destructive ion-milling process used to etch the wires, and the small device geometries near the resolution limit of our photolithography process. Occasionally voltage sensing leads would break due to overexposed photoresist

being etched away during ion-milling, exposing the device lead to the etch beam. For further analysis, the strategy in most devices was to choose the single-channel PSD believed to best represent the device resistance. This was typically a 4-terminal resistance channel with clear $1/f$ behavior and the expected quadratic scaling with bias current.

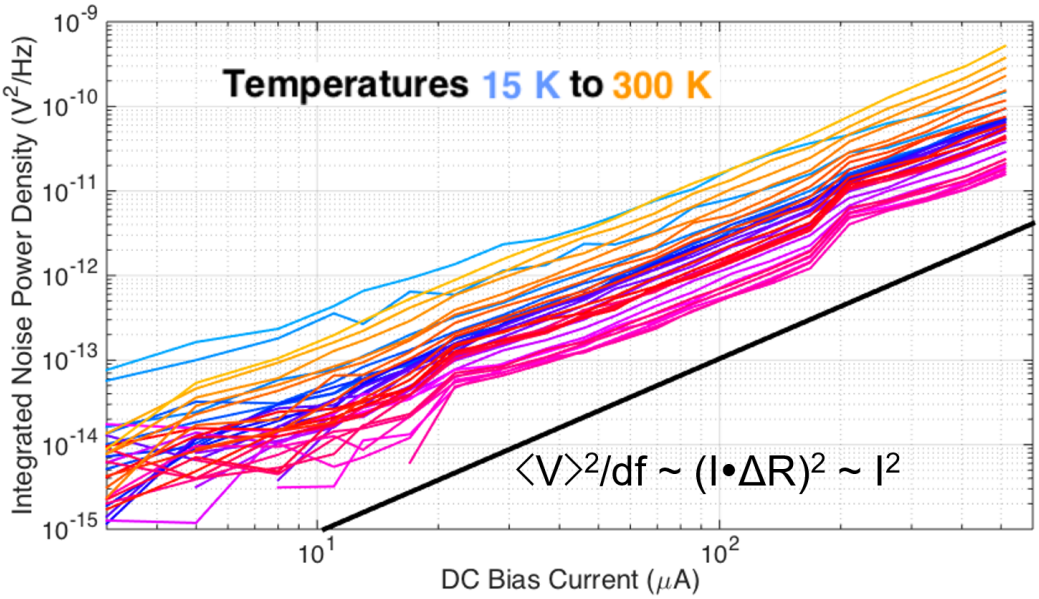

Figure 5.4: **Noise power scales quadratically with current.** Integrated low-f noise power as a function of current in an LBCO wire at $x = 0.14$. Temperatures vary on a color scale from light blue (15 K, below T_c), through blue, violet, red, and orange (300 K). For each temperature, the Johnson + amplifier noise measured at zero current has been subtracted. The solid black line indicates the expected quadratic scaling, which has a slope of 2 on a log-log plot. The noise is observed to scale quadratically at all currents, suggesting that the observed noise is caused by fluctuating resistance.

As described above (section 2.2), resistance noise should have quadratic scaling with the DC bias current. To study noise variations with current and temperature, we will consider an integral of the power spectral density over a low frequency range, 0.3 Hz to 9.6 Hz and track the variation of this integrated PSD over the parameter range of interest. Reviewing the spectra shown previously in Figs. 5.2 and 5.3, it becomes apparent that over this frequency range, typical spectra are close to $1/f$ and have no anomalous peaks for essentially all currents and temperatures.

For a sample at $x \sim 0.14$, the scaling of this noise integral with current is described in

Fig. 5.4. Temperatures are labeled according to a smoothly varying color scale spanning 15 K (blue), which is below T_c to 300 K (orange). The measured noise is found to vary approximately quadratically with current for the entire range of temperatures. To reveal the quadratic current scaling at low DC biases, it is essential that background noise from sources other than resistance fluctuations be subtracted, especially if the noise PSD being considered originates from a single channel and is not cross-correlated. Therefore, for each sample and each measurement temperature, noise spectra were recorded with zero DC current to quantify the contribution of Johnson noise and amplifier noise. These two contributions should be constant with respect to current. The integral of this measured current-independent background noise was subtracted from the finite-current data as a form of offset removal for plots such as Fig. 5.4. Because the preamp noise may be comparable to resistance fluctuation noise at low currents, this careful background subtraction was required for accurate characterizations of the resistance noise.

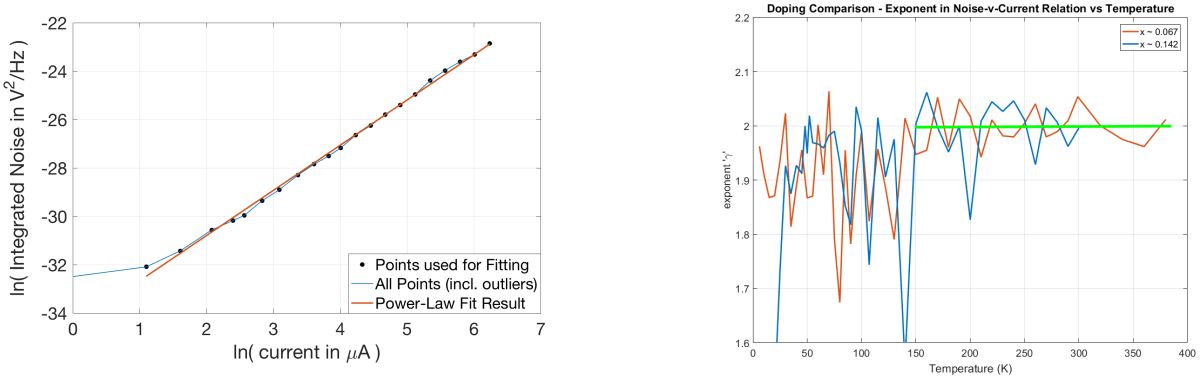

(a) (b)

Figure 5.5: **Power-law fitting of the variation of noise with current.** (a) Example fit of the current-dependent integrated noise to a power law. Sample had doping $x \sim 0.07$ and was measured at 50 K. (b) The exponent γ from the power-law fit of noise-vs-current, as a function of temperature. For two dopings x 0.07 and x 0.14 it appears that, below about 150 K, the exponent may be consistently less than $\gamma = 2$ (green line).

For later comparative plots of noise-vs-temperature at different dopings, the scaling with current will be collapsed by plotting the integrated noise as a function of current

I, fitting this data to a power law $\int S_V \propto CI^\gamma$, and considering the coefficient C of this power law as a function of temperature and doping. An example of such a power law fit to the current-dependent noise is shown in Fig. 5.5(a). For the example depicted, the best-fit power law is extremely close to the data, except at the lowest bias current. In samples where this power-law fitting was performed manually, outliers were also excluded from the fit at this stage. Anomalous values for the integrated PSD may occur at low currents if the zero-current background noise was not measured with sufficient accuracy, or at high currents if the current drives ohmic heating or if the voltage noise is clipped by the maximum output voltage of the amplifier chain.

Additionally, some PSDs were affected by an unidentified source of intermittent "burst" noise, characterized by the appearance of sudden voltage spikes after several minutes of lower-noise output. Noise spectra computed from signals including burst noise often deviated from $1/f$ behavior. The anomalous burst noise was usually correlated between redundant amplifier channels, so it is possible that it is related to a real physical process occurring in the device. However, repeated sweeps of the bias current usually did not reproduce the burst noise and, after multiple sweeps, the minimum noise values observed at each current usually did coincide with quadratic current scaling. It is believed that even if the burst noise does have a physical origin, there is an independent low level of $1/f$ noise fluctuations scaling quadratically with current. For purposes of our analysis, we associated this $1/f$ noise with resistance fluctuations in the LBCO wires, and rejected as outliers the anomalously high PSDs affected by burst noise. These points could be easily identified in plots like Fig. 5.5(a) by their deviation from otherwise-quadratic scaling with current.

As discussed previously in Fig. 5.1, noise near the charge-ordering transition in an early inhomogeneous LBCO wire gave the indication of possible stripe pinning along the direction of applied electric fields. Based on the power-law fitting described in Fig. 5.5, we can now make additional commentary on the possibility of current-induced pin-

ning. In at least two samples, the exponent γ from the fit to the $\int S_V \propto CI^\gamma$ appears to lie very close to $\gamma = 2$ at high temperatures, as shown in Fig. 5.5(b). However, at temperatures below about 150 K, the average value of γ seems to decrease suggesting sub-quadratic scaling of the noise with current. Our measurements lack the precision required to describe this exponent in any more detail, but $\gamma < 2$ could be caused by partial pinning of stripes along the direction of applied current. The idea that resistance noise increases quadratically with applied current relies on the assumption that increasing current does not change the nature of the resistance fluctuators themselves, only their visibility via Ohm's law. However, if dynamic stripes are pinned or frozen by high currents, then that assumption would no longer be true. If reproducible, the observation that low-temperature resistance noise in LBCO scales with current as $\int S_V \propto CI^\gamma$ with $\gamma < 2$ could be a strong indication that the resistance fluctuations in LBCO microwires are truly stripe-like in character.

5.2 LBCO's noisy phase diagram

The phase diagram of LBCO may be compared to the resistance fluctuations measured in thin film devices if we consider the low-frequency integrated PSD, described in the previous section, as a function of temperature and doping. In one microwire at $x \sim 0.14$, this noise integral was particularly well behaved over the entire range of measurement parameters. The $x \sim 0.14$ sample's integrated PSD is displayed as a function of temperature for all measurement currents in Fig. 5.6. The high noise at room temperature decays as the sample is cooled, with roughly exponential behavior. Relative to this background temperature dependence of the normal state noise, an additional noise source turns on near 200 K for all bias currents high enough to resolve resistance fluctuations. This temperature may coincide with the pseudogap crossover at this doping and the kink near T^* in the temperature-dependent noise is nearly identical to the noise feature observed in

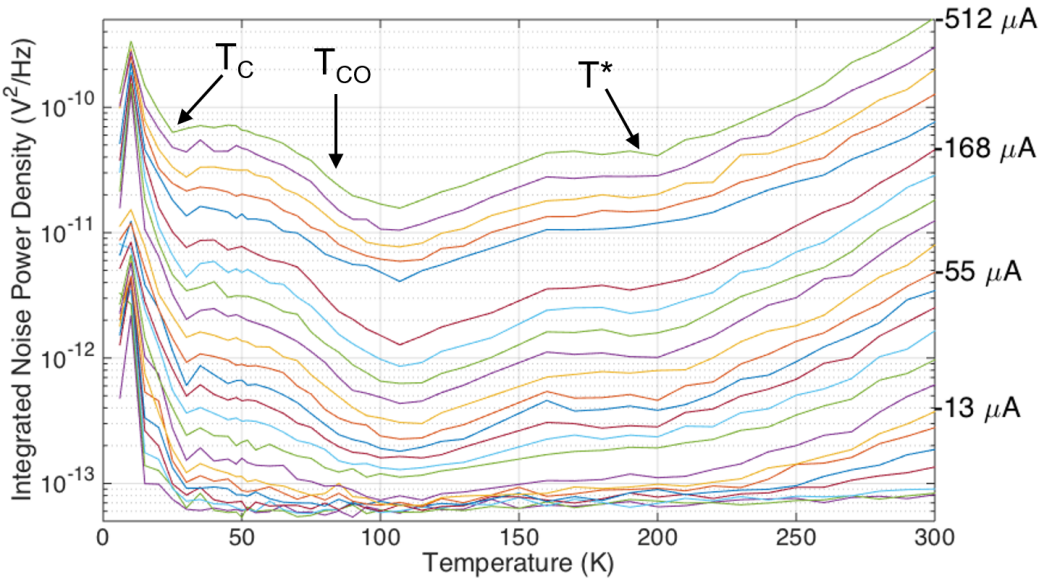

Figure 5.6: **Integrated noise power vs temperature for $x\sim$ 0.14 LBCO.** Combined power spectral density over the range 0.3 to 9.6 Hz as a function of temperature. High bias currents result in larger noise, and are closer to the top of the plot. Currents are approximately logarithmically spaced as labelled on the right. The normal-state resistance noise decays approximately exponentially as the sample is cooled from room temperature. Compared to this background noise decay with cooling, three additional noise sources appear to turn on at temperatures relavant to the LBCO phase diagram: T^* (pseudogap crossover), T_{CO} (charge ordering onset), and T_c (superconducting transition).

the previous resistance fluctuation studies on $YBa_2Cu_3O_{7-7}$ [58].

Further cooling the $x \sim 0.14$ sample leads to an even larger noise increase near 80 K, which is somewhat comparable to the typical charge-ordering transition temperature expected for high-doping LBCO. The noise increase near T_{CO} is not sudden, but instead occurs over a range of 30-40 K. If this noise feature is caused by charge stripes, then the slow onset of ordering would be consistent with scattering experiments that have seen more muddled stripe-ordering transitions at higher dopings [31]. Finally at T_c, noise increases sharply. The large noise in the superconducting state is observed to decrease somewhat as temperature is lowered below T_c, typically has non-quadratic current scaling, and is typically observed in LBCO devices <50 nm thick. In at least one thicker LBCO device (not shown), noise was observed to decrease at T_c rather than increase. The combination of these properties of the voltage fluctuations below T_c suggest they are likely caused by

vortex motion in the superconducting LBCO device and are distinct from the resistance fluctuations at and below T_{CO}.

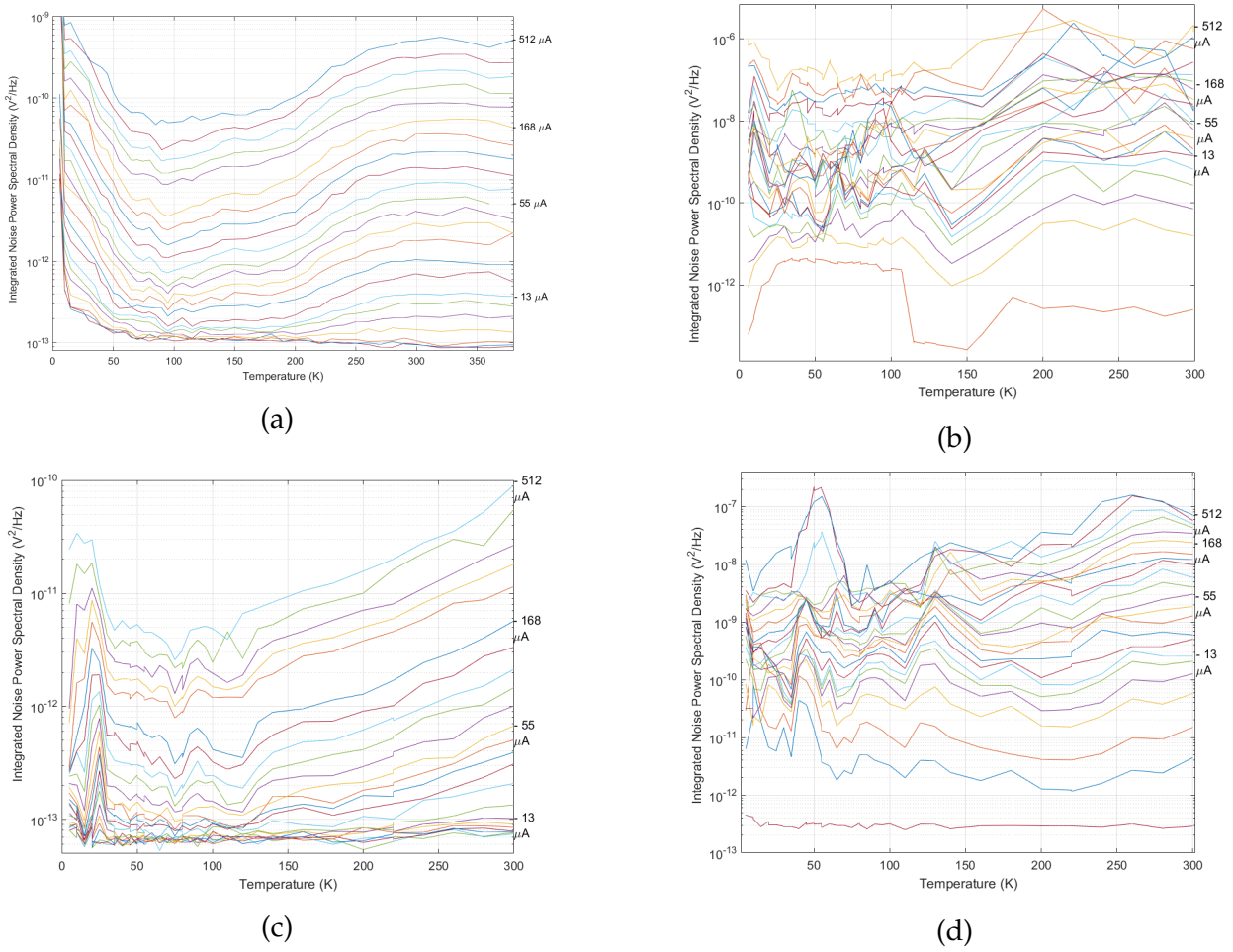

Figure 5.7: **Integrated noise power vs temperature for additional dopings.** (a) $x \sim 0.07$ single-channel PSD. (b) $x \sim 0.11$ cross-PSD of two 3-terminal resistance channels likely affected by contact noise. (c) $x \sim 0.13$ single-channel PSD for a device oriented on the crystalline substrate such that current flows along the *a*-*b* directions of the LBCO lattice. (d) $x \sim 0.13$ single-channel PSD for a device on the same chip as (d) oriented with current flowing at a 45° angle to the *a*-*b* directions of LBCO. Further discussion in text.

The visualization of integrated noise demonstrated in Fig. 5.6 can also be applied to LBCO devices at other dopings. Unfortunately, the presence of crossovers or critical temperatures is less obvious in the noise vs temperature plots of the additional devices shown in Fig. 5.7. However a couple of trends appear to be universal. In all devices, noise decreases as the system is cooled from room temperature to about 100 K, and then

increases at low temperature. The beginning of the low-temperature noise increase or any low-T peaks is below 100 K, but above T_c, suggesting that this not simply the effect of the superconducting state alone, but rather an above-T_c state (such as charge order). This sharply increased noise at low temperatures is itself an exceptional observation. In contrast, the typical $1/f$ noise in the conducting materials that inspired the Dutta-Horn model (Chapter 2) almost always decreases as temperature is lowered.

Additional features in the temperature variation of the noise can be described for specific devices. In Fig. 5.7(a) on a microwire at $x \sim 0.07$, measurements extend above room temperature in order to better resolve the possible pseudogap crossover at T^*. As expected in a sample with low doping, the broad knee feature that we associated with the pseudogap in these devices occurs at a high temperature, slightly above 300 K. Comparison between this sample and the $x \sim 0.14$ sample (Fig. 5.6) suggests a T^* boundary that decreases with increased doping, as expected for a cuprate material. The noise does increase further below about 80 K, but in contrast to the $x \sim 0.14$ device, this region of the noise-vs-temperature curves is concave-up, rather than concave-down, which is less suggestive of a noise phase that stabilizes below 80 K and more suggestive of slowly changing dynamics. However, the 80 K increase in the $x \sim 0.07$ is larger than the same increase in the $x \sim 0.14$ sample. Although no stripe phase is expected for dopings below $x \sim 0.095$, this sample at $x \sim 0.07$ may show evidence of the low-T noise phase we had previously equated to charge order. One possibility is that this low-doping sample still has charge order in some regions of the device due to some degree of dopant inhomogeneity creating patches of higher-x LBCO.

In Fig. 5.7(b), noise is shown for a sample at $x \sim 0.11$. The PSD used for this plot was a cross-PSD between two three-terminal resistance signals; this is a less-than-ideal measurement strategy required by the low yield of stable contacts. Three-terminal resistance means, in this case, that one of the two voltage-sensing connections also had flowing current and therefore the resistance signal would include the contact resistance of a

single metal-LBCO interface. The contact voltage included in the first 3-terminal resistance channel was *not* the same contact voltage included in the second channel for cross-correlation. Therefore, noise associated with contact voltages should disappear under cross correlation. However, because the uncorrelated voltage noise at the contact may be much higher than the device noise itself, this could lead to anomalous results as described in Fig. 5.3(b). As an additional complication, the resistance of one of the leads used in this experiment was observed to suddenly increase for measurements above about 150 K, from 30 kΩ to 1 MΩ. This damage to the connection seemed to be irreversible. Again the effect of this large lead resistance should vanish due to cross-correlation, but may not if the effect is too large. Noise may increase near 30 or 25 K for the curves at some currents, but this is close to the sample's T_c of 20 K, and thus may not be distinguishable from the noise of the superconducting state. The data for this device is interpreted as having no identifiable temperature-dependent features, and may be influenced by the non-ideal electrical contacts used in its measurement.

Noise-vs-temperature plots from two devices fabricated from the same $x \sim 0.13$ LBCO film are shown in Fig. 5.7(c)-(d). The device of Fig. 5.7(c) was oriented on the epitaxial film such that current would flow along the twinned a/b direction of the crystalline LBCO (this is the same orientation used for most devices). The device of Fig 5.7(d) was oriented such that current flows along the $\langle 110 \rangle$ direction, diagonal to the a and b lattice directions. This experiment was intended to detect possible anisotropy associated with resistance noise caused by charge order. In the diagonal device, stripe orientation along the "a" lattice direction and "b" lattice direction are both at 45° to the direction of current flow and therefore no resistance difference is expected between the two stripe orientations. As the stripe domain configuration moves, the "straight" microwire should experience resistance noise, while the equivalent noise is suppressed in the diagonal wire. It should be noted that for unknown reasons, the diagonal wire of this experiment had, at 300 K, a four-terminal DC resistance of 5 kΩ, ten times higher than the straight microwire with a

resistance of 500 Ω. The diagonal device did not have a clear superconducting transition, while the a/b-oriented device was observed to have a low T_c; this could be caused in part by a small degree of inhomogeneity in this sample that was intended to be close to the suppressed superconducting state at $x = 0.125$.

The $\langle 100 \rangle$-oriented microwire in Fig. 5.7(c) had several temperature-dependent noise features. A dip in the noise occurs at 120 K, a peak near 90 K, and another dip near 75 K. A clear noise increase, or peak occurs at and below 35 K, which is well above T_c in this device. It isn't obvious which of these numerous features, if any, should be identified with a low-temperature ordered phase, and which are perhaps caused by residual effects of burst noise that was not fully eliminated from the data set. Below about 75 K, this sample strongly resembles the $x \sim 0.14$ sample of Fig. 5.6, which is reasonable considering they are somewhat close in doping. The diagonal device in Fig. 5.7(d) has significantly different behavior, a possible knee feature near T^* may be slightly visible at at 250 K at higher currents, or at 150 K over a wider range of currents. At lower temperatures, a peak in the noise is observed near 50-55 K for all currents, at high currents this peak is significantly wider, and begins at 75 K. The noise in the diagonal wire appears to drop near 35 K, which perhaps significantly is the same temperature at which noise increases in the straight microwire.

Finally, the temperature-dependent noise characteristics of several measured devices have been collapsed with respect to current, and are compared in Fig. 5.8. The collapse of the current dependence of the noise was performed either by taking the coefficient C at each temperature from the power law fitting to the form $\int S_V \propto CI^\gamma$, as discussed in Fig. 5.5, or by consideration of $\int S_V/(I^2)$ for the highest few currents in each device; these techniques should be equivalent. The result is a single curve for each device representing its resistance noise as a function of temperature, allowing easy comparison of devices. Note that the values on such a curve will typically be proportional to the device's DC resistance squared. Because the resistances of the LBCO devices are variable, the average

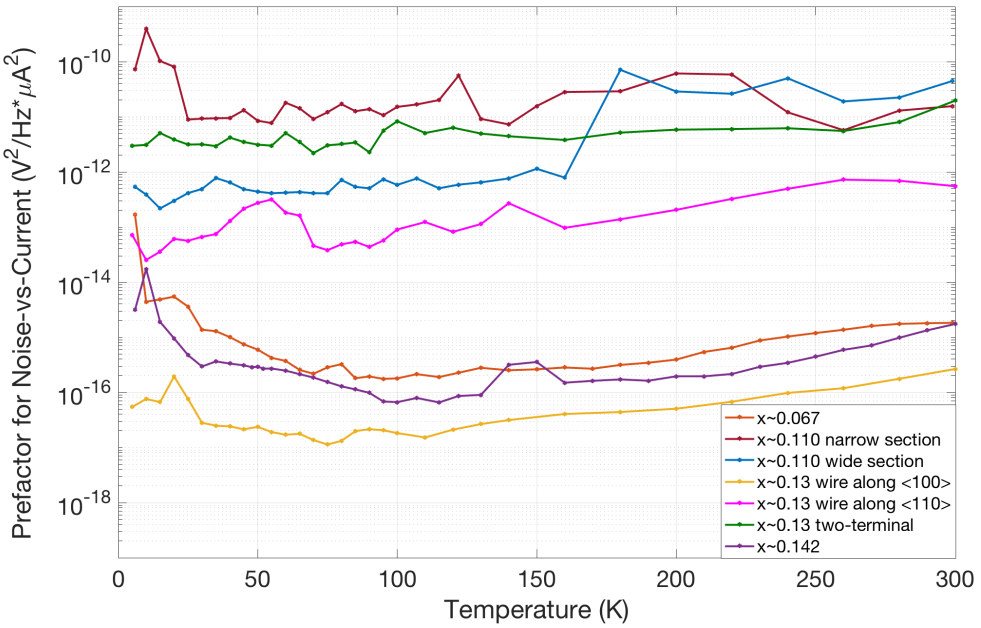

Figure 5.8: **Noise comparison of all measured microwires** The coefficient from the power law fit of noise vs current is plotted as a function of temperature. Different curves indicate different devices, dopings, or noise channels, as labelled.

magnitude of these noise-vs-temperature curves may not provide a meaningful comparison. However, the variations within each curve with respect to temperature should be comparable.

Firstly, high-magnitude, mostly temperature-independent noise was observed for two series-connected sections of the $x \sim 0.11$ device. This can be compared to a two-terminal resistance measurement from the $x \sim 0.13$ device which was also high-noise and relatively flat with temperature. We know that the two-terminal $x \sim 0.13$ noise measurement is dominated by fluctuations in contact resistance and/or thermoelectric voltage, because 4-terminal channels in the same devices give significantly lower noise. The fact that the $x \sim 0.11$ noise looks similar suggests that it too is dominated by contact noise over most of its temperature range, rather than resistance fluctuations of the LBCO wire.

Secondly, the curves of the $x \sim 0.07$ wire , straight $x \sim 0.13$ wire, and $x \sim 0.11$ wire can be compared. Noting that $x \sim 0.07$ *should* have no stripe state, we can consider this curve (red) a measurement of the non-stripe background noise. Compared to this

curve, the $x \sim 0.13$ $\langle 100 \rangle$ and $x \sim 0.14$ microwires appear to have low-temperature noise onsets at slightly higher temperatures, and appear to have noise that increases roughly exponentially as the sample is cooled, while the $x \sim 0.07$ samples may have more slowly increasing noise.

Finally, at $x \sim 0.13$ doping, the $\langle 100 \rangle$-oriented and $\langle 110 \rangle$-oriented microwires may be compared. The straight microwire appears to have a gradual noise increase that begins below ~ 100 K. The diagonal microwire, in contrast, appears to have two nearly step-like increases noise power at 150 K and 70 K. These respectively may correspond to the pseudogap phase and charge ordering. Compared to a background extrapolated from high temperatures, the diagonal wire's noise may actually decrease gradually after the sudden increase at 70 K, possibly suggesting a slowing or freezing of possible stripe dynamics. This result, that the $\langle 110 \rangle$-oriented microwire has higher noise with sharper temperature-dependent features than the $\langle 100 \rangle$-oriented microwire is contrary to the initial expectation that the diagonal wire would have suppressed noise due to symmetry of the two domain orientations. An explanation for the difference between these two devices is not known, but could provide further insight into the effect of charge-stripe phases on resistance fluctuations in LBCO near $x = 1/8$.

Chapter 6

Conclusions and Future Work

6.1 Conclusions

In summary, $La_{2-x}Ba_xCuO_4$ has been successfully deposited by pulsed laser deposition, and the presence of low-temperature resistance fluctuations in LBCO microwires has been observed in several devices near $x = 1/8$. Growing the LBCO films was a complex process requiring synthesis of high-quality custom PLD targets by a steric entrapment technique, careful optimization of laser deposition parameters, and post-growth characterizations of film properties, including superconductivity. Doping was a particularly difficult film parameter to study, as the films appeared to lose barium relative to the target composition. LBCO films were microfabricated into microscopic wires whose noise properties were studied in a cryogenic system with low-noise electronics. In most samples, resistance fluctuations were observed to scale quadratically, or occasionally subquadratically with current, and were found to increase below about 80 K, especially in devices with doping near $x = 0.125$. One particular sample with $x \sim 0.14$ had three features in its temperature-dependent noise that were easily identified with the pseudogap, charge ordering, and superconductivity. A comparison between two devices from the same $x \sim 0.13$ film suggested interesting differences in the noise for current flowing parallel to the $\langle 100 \rangle$ direction and noise for current parallel to the $\langle 110 \rangle$ direction, with the "diagonal" device having higher-magnitude, sharper noise features.

6.2 Possible future experiments

Future work could extend these studies in numerous directions. Further noise studies in LBCO could benefit from additional samples at a variety of dopings, especially near $x = 0.125$ and slightly below. Many experiments could be done on the in-plane orientation dependence of the resistance fluctuations, as was briefly attempted with our dual-device $x \sim 0.13$ sample. In particular it would be useful to compare two devices that differ *only* by orientation, but have the same T_c and above-T_c resistance. Additional device angles could also be studied, or more sophisticated techniques could be attempted to search for noise anisotropy, e.g. looking for anticorrelations of perpendicular resistance measurements in a cross-shaped geometry, as described in [60]. For practical purposes, revaluation of the cryogenic and electronic noise-measurement systems used here should focus on identifying and eliminating possible sources of burst noise in the measured noise signals. The necessity to repeatedly re-sweep current in many of the above measurements to avoid burst-noise effects increased the already lengthy measurement time by a factor of 3 or 4; finding and removing this problem (if it does not originate from the sample itself) could simplify future measurements.

Finally, some similar experiments on other materials could be considered. We've initiated some efforts to grow Eu-doped LSCO films by laser deposition, but have not yet succeeded in obtaining superconducting films. If thin film superconducting devices with the correct electronic phase are obtainable, this could be extremely useful for noise studies near the $x = 1/8$ anomaly. LESCO has proposed charge-ordering transition temperature well above its superconducting temperature, so resistance fluctuations associated with the stripe state could be measured over a wider temperature range. This would potentially allow for experiments regarding how the stripe state freezes or pins to disorder as temperature is lowered. More subtle temperature-dependence effects, such as any noise changes associated with the proposed pair-density wave state at $x = 1/8$ may also be

measurable in LESCO. Some oxides other than superconductors, such as the nickelate family $La_{2-x}A_xNiO_4$, where A = Ca, Ba, or Sr and $x \sim 0.3$, have charge-ordering transition temperatures > 200 K [111], and may be interesting subjects for resistance noise spectroscopy.

References

[1] J. File and R. G. Mills. Observation of persistent current in a superconducting solenoid. *Physical Review Letters*, 10:93–96, 1963.

[2] W. Meissner and R. Ochsenfeld. Ein neuer effekt bei eintritt der supraleitfähigkeit. *Naturwissenschaften*, 21(44):787–788, 1933.

[3] I. Giaever. Energy gap in superconductors measured by electron tunneling. *Physical Review Letters*, 5:147–148, 1960.

[4] R. E. Glover and M. Tinkham. Transmission of superconducting films at millimeter-microwave and far infrared frequencies. *Physical Review*, 104:844–845, 1956.

[5] W. S. Corak, B. B. Goodman, C. B. Satterthwaite, and A. Wexler. Atomic heats of normal and superconducting vanadium. *Physical Review*, 102:656–661, 1956.

[6] H. K. Onnes. On the sudden rate at which the resistance of mercury disappears. *Communications from the Physical Laboratory at the University of Leiden*, 120b, 122b, 124c, 1911.

[7] J. Bardeen., L. N. Cooper, and J. Schrieffer. Theory of superconductivity. *Physical Review*, 108:1175–1204, 1957.

[8] V. L. Ginzburg and L. D. Landau. *Zhurnal Eksperimental'noi i Teoreticheskoi Fiziki*, 20: 1064, 1950.

[9] Michael TInkham. *Introduction to Superconductivity*. McGraw-Hill, second edition, 1996.

[10] P. Dai, B. C. Chakoumakos, G. F. Sun, K. W. Wong, Y. Xin, and D. F. Lu. Synthesis and neutron powder diffraction study of the superconductor $HgBa_2Ca_2Cu_3O_{8+d}$ by Tl substitution. *Physica C: Superconductivity*, 234:201–206, 1995.

[11] G. Bednorz and K.A. Müller. *Zeitschrift für Physik*, B64:189, 1986.

[12] J. Dominec. High T_c superconductors: Does higher debye temperature mean higher critical temperature? *Physica Status Solidi (b)*, 169(2):K83–K85, 1992.

[13] J. G. Bednorz and K. A. Müller. Perovskite-type oxides—the new approach to high-Tc superconductivity. nobel lecture. *Angewandte Chemie International Edition in English*, 27(5):735–748, 1988. URL `http://dx.doi.org/10.1002/anie.198807351`.

[14] B. Batlogg, R. J. Cava, A. Jayaraman, R. B. van Dover, G. A. Kourouklis, S. Sunshine, D. W. Murphy, L. W. Rupp, H. S. Chen, A. White, K. T. Short, A. M. Mujsce, and E. A. Rietman. Isotope effect in the high-T_c superconductors $Ba_2YCu_3O_7$ and $Ba_2EuCu_3O_7$. *Physical Review Letters*, 58:2333–2336, 1987.

[15] G. Chen and W. A. Goddard. The magnon pairing mechanism of superconductivity in cuprate ceramics. *Science*, 239:899–902, 1988.

[16] M. Le Tacon, G. Ghiringhelli, J. Chaloupka, M. Moretti Sala, V. Hinkov, M. W. Haverkort, M. Minola, M. Bakr, K. J. Zhou, S. Blanco-Canosa, C. Monney, Y. T. Song, G. L. Sun, C. T. Lin, G. M. De Luca, M. Salluzzo, G. Khaliullin, T. Schmitt, L. Braicovich, and B. Keimer. Intense paramagnon excitations in a large family of high-temperature superconductors. *Nature Physics*, 7:725–730, 2011.

[17] J. Hoffman. Cuprate superconductors, 2010. URL `http://hoffman.physics.harvard.edu/materials/Cuprates.php`. Accessed: 2017-02-21.

[18] S. N. Ruddlesden and P. Popper. The compound $Sr_3Ti_2O_7$ and its structure. *Acta Crystallographica*, 11:54–55, 1958.

[19] G. Grissonnanche, O. Cyr-Choinière, F. Laliberté, S. Renéde Cotret, A. Juneau-Fecteau, S. Dufour-Beauséjour, M. È. Delage, D. LeBoeuf, J. Chang, B. J. Ramshaw, D. A. Bonn, W. N. Hardy, R. Liang, S. Adachi, N. E. Hussey, B. Vignolle, C. Proust, M. Sutherland, S. Krämer, J. H. Park, D. Graf, N. Doiron-Leyraud, and L. Taillefer. Direct measurement of the upper critical field in cuprate superconductors. *Nature Communications*, 5:3280, 2014.

[20] Z.-X. Shen, D. S. Dessau, B. O. Wells, D. M. King, W. E. Spicer, A. J. Arko, D. Marshall, L. W. Lombardo, A. Kapitulnik, P. Dickinson, S. Doniach, J. DiCarlo, T. Loeser, and C. H. Park. Anomalously large gap anisotropy in the a-b plane of $B_2Sr_2CaCu_2O_{8+\delta}$. *Physical Review Letters*, 70:1553–1556, 1993.

[21] D. A. Wollman, D. J. Van Harlingen, W. C. Lee, D. M. Ginsberg, and A. J. Leggett. Experimental determination of the superconducting pairing state in ybco from the phase coherence of YBCO-Pb dc SQUIDs. *Physical Review Letters*, 71:2134–2137, 1993.

[22] N. Doiron-Leyraud, C. Proust, D. LeBoeuf, J. Levallois, J.-B. Bonnemaison, R. Liang, D. A. Bonn, W. N. Hardy, and L. Taillefer. Quantum oscillations and the fermi surface in an underdoped high-Tc superconductor. *Nature*, 447(7144):565–568, 2007.

[23] T. Timusk and B. Statt. The pseudogap in high-temperature superconductors: an experimental survey. *Reports on Progress in Physics*, 62:61–122, 1999.

[24] K. Ishida, K. Yoshida, T. Mito, Y. Tokunaga, Y. Kitaoka, K. Asayama, Y. Nakayama, J. Shimoyama, and K. Kishio. Pseudogap behavior in single-crystal $Bi_2Sr_2CaCu_2O_{8+\delta}$ probed by Cu NMR. *Physical Review B*, 58:R5960–R5963, 1998.

[25] V. J. Emery and S. A. Kivelson. Importance of phase fluctuations in superconductors with small superfluid density. *Nature*, 374:434–437, 1995.

[26] Z. A. Xu, N. P. Ong, Y. Wang, T. Kakeshita, and S. Uchida. Vortex-like excitations and the onset of superconducting phase fluctuation in underdoped $La_{2-x}Sr_xCuO_4$. *Nature*, 406(6795):486–488, 2000.

[27] J. Xia, E. Schemm, G. Deutscher, S. A. Kivelson, D. A. Bonn, W. N. Hardy, R. Liang, W. Siemons, G. Koster, M. M. Fejer, and A. Kapitulnik. Polar Kerr-effect measurements of the high-temperature $YBa_2Cu_3O_{6+x}$ superconductor: Evidence for broken symmetry near the pseudogap temperature. *Physical Review Letters*, 100:127002:1–4, 2008.

[28] M. J. Lawler, K. Fujita, Jhinhwan Lee, A. R. Schmidt, Y. Kohsaka, Chung Koo Kim, H. Eisaki, S. Uchida, J. C. Davis, J. P. Sethna, and E.-A. Kim. Intra-unit-cell electronic nematicity of the high-T_c copper-oxide pseudogap states. *Nature*, 466:347–351, 2010.

[29] A. Mesaros, K. Fujita, S. D. Edkins, M. H. Hamidian, H. Eisaki, S.-I. Uchida, J. C. Samus Davis, M. J. Lawler, and E.-A. Kim. Commensurate $4a_0$-period charge density modulations throughout the $Bi_2Sr_2CaCu_2O_{8+x}$ pseudogap regime. 113: 12661–12666, 2016.

[30] W. Tabis, B. Yu, I. Bialo, M. Bluschke, T. Kolodziej, A. Kozlowski, Y. Tang, E. Weschke, B. Vignolle, M. Hepting, H. Gretarsson, R. Sutarto, F. He, M. Le Tacon, N. Barii, G. Yu, and M. Greven. New insight into cuprate charge order from x-ray measurements of $HgBa_2CuO_{4+\delta}$. URL `http://arxiv.org/abs/1702.03348v1`.

[31] M. Hücker, M. v. Zimmermann, G. D. Gu, Z. J. Xu, J. S. Wen, Guangyong Xu, H. J. Kang, A. Zheludev, and J. M. Tranquada. Stripe order in superconducting $la_{2-x}ba_xcuo_4$ ($0.095 \leqslant x \leqslant 0.155$). *Physical Review B*, 83:104506, 2011.

[32] B. G. Levi. Magnetism and superconductivity fight for control in high-T_c superconductors. *Physics Today*, 55(2):14–16, 2002.

[33] J. M. Tranquada, H. Woo, T. G. Perring, H. Goka, G. D. Gu, G. Xu, M. Fujita, and K. Yamada. Quantum magnetic excitations from stripes in copper oxide superconductors. *Nature*, 429:534–538, 2004.

[34] P. Abbamonte, A. Rusydi, S. Smadici, G. D. Gu, G. A. Sawatzky, and D. L. Feng. Spatially modulated 'Mottness' in $La_{2-x}Ba_xCuO_4$. *Nature Physics*, 1:155–158, 2005.

[35] Yasushi Abe, Yoichi Ando, J. Takeya, H. Tanabe, T. Watauchi, I. Tanaka, and H. Kojima. Normal-state magnetotransport in $La_{1.905}Ba_{0.095}CuO_4$ single crystals. *Physical Review B*, 59:14753–14756, 1999.

[36] G. Ghiringhelli, M. Le Tacon, M. Minola, S. Blanco-Canosa, C. Mazzoli, N. B. Brookes, G. M. De Luca, A. Frano, D. G. Hawthorn, F. He, T. Loew, M. Moretti Sala, D. C. Peets, M. Salluzzo, E. Schierle, R. Sutarto, G. A. Sawatzky, E. Weschke, B. Keimer, and L. Braicovich. Long-range incommensurate charge fluctuations in (Y,Nd)$Ba_2Cu_3O_{6+x}$. *Science*, 337(6096):821–825, 2012.

[37] S-W. Cheong, G. Aeppli, T. E. Mason, H. Mook, S. M. Hayden, P. C. Canfield, Z. Fisk, K. N. Clausen, and J. L. Martinez. Incommensurate magnetic fluctuations in $La_{2-x}Sr_xCuO_4$. *Physical Review Letters*, 67:1791–1794, 1991.

[38] S. A. Kivelson, I. P. Bindloss, E. Fradkin, V. Oganesyan, J. M. Tranquada, A. Kapitulnik, and C. Howald. How to detect fluctuating stripes in the high-temperature superconductors. *Reviews of Modern Physics*, 75:1201–1241, 2003.

[39] J. M. Tranquada, B. J. Sternlieb, J. D. Axe, Y. Nakamura, and S. Uchida. Evidence for stripe correlations of spins and holes in copper oxide superconductors. *Nature*, 375(6532):561–563, 1995.

[40] H.-H. Klauss, W. Wagener, M. Hillberg, W. Kopmann, H. Walf, F. J. Litterst, M. Hücker, and B. Büchner. From antiferromagnetic order to static magnetic stripes: The phase diagram of (La,Eu)$_{2-x}Sr_xCuO_4$. *Physical Review Letters*, 85:4590–4593, 2000.

[41] T. Valla, A. V. Fedorov, Jinho Lee, J. C. Davis, and G. D. Gu. The ground state of the pseudogap in cuprate superconductors. *Science*, 314(5807):1914–1916, 2006.

[42] C. Reichhardt, C. J. Olson Reichhardt, and A. R. Bishop. Hysteresis and noise in stripe- and clump-forming systems. *Europhysics Letters*, 72(3):444, 2005.

[43] E. Berg, E. Fradkin, E.-A. Kim, S. A. Kivelson, V. Oganesyan, J. M. Tranquada, and S. C. Zhang. Dynamical layer decoupling in a stripe-ordered high-T_c superconductor. *Physical Review Letters*, 99:127003, 2007.

[44] J. Wen, Q. Jie, Q. Li, M. Hücker, M. v. Zimmermann, Su Jung Han, Zhijun Xu, D. K. Singh, R. M. Konik, Liyuan Zhang, Genda Gu, and J. M. Tranquada. Uniaxial linear resistivity of superconducting $La_{1.905}Ba_{0.095}CuO_4$ induced by an external magnetic field. *Physical Review B*, 85:134513, 2012.

[45] P. Dutta and P. M. Horn. Low-frequency fluctuations in solids: $1/f$ noise. *Reviews of Modern Physics*, 53:497–516, 1981.

[46] J. B. Johnson. Thermal agitation of electricity in conductors. *Physical Review*, 32: 97–109, 1928.

[47] H. Nyquist. Thermal agitation of electric charge in conductors. *Physical Review*, 32: 110–113, 1928.

[48] H. B. Callen and T. A. Welton. Irreversibility and generalized noise. *Physical Review*, 83:34–40, 1951.

[49] A. Khintchine. Korrelationstheorie der stationären stochastischen prozesse. *Mathematische Annalen*, 109(1):604–615, 1934.

[50] J. W. Eberhard and P. M. Horn. Excess (1/f) noise in metals. *Physical Review B*, 18: 6681–6693, 1978.

[51] B. Pellegrini, R. Saletti, P. Terreni, and M. Prudenziati. $1/f^{\gamma}$ noise in thick-film resistors as an effect of tunnel and thermally activated emissions, from measures versus frequency and temperature. *Physical Review B*, 27:1233–1243, 1983.

[52] M. B. Weissman. $1/f$ noise and other slow nonexponential kinetics in condensed matter. *Reviews of Modern Physics*, 60:537–571, 1988.

[53] Low-frequency noise as a tool to study disordered materials. *Annual Review of Materials Science*, 26(1):395–429, 1996.

[54] Y. Ando, K. Segawa, S. Komiya, and A. N. Lavrov. Electrical resistivity anisotropy from self-organized one dimensionality in high-temperature superconductors. *Physical Review Letters*, 88:137005, 2002.

[55] M. van Zalk, A. Brinkman, and H. Hilgenkamp. Conductance anisotropy and linear magnetoresistance in $La_{2x}Sr_x$ CuO_4 thin films. *Journal of Physics: Condensed Matter*, 23(20):205602, 2011.

[56] H.-W. Jiang and A. J. Dahm. Conduction properties of a new two-dimensional sliding charge-density wave. *Physical Review Letters*, 62:1396–1399, 1989.

[57] J. A. Bonetti, D. S. Caplan, D. J. Van Harlingen, and M. B. Weissman. Electronic transport in underdoped $YBa_2Cu_3O_{7-\delta}$ nanowires: Evidence for fluctuating domain structures. *Physical Review Letters*, 93:087002, 2004.

[58] D. S. Caplan, V. Orlyanchik, M. B. Weissman, D. J. Van Harlingen, E. H. Fradkin, M. J. Hinton, and T. R. Lemberger. Anomalous noise in the pseudogap regime of $YBa_2Cu_3O_{7-\delta}$. *Physical Review Letters*, 104:177001, 2010.

[59] J. R. LaGraff and D. A. Payne. Chemical diffusion of oxygen in single-crystal and polycrystalline $YBa_2Cu_3O_{6+x}$ determined by electrical-resistance measurements. *Physical Review B*, 47:3380–3390, 1993.

[60] R. D. Black, W. M. Snow, and M. B. Weissman. Nonscalar $1/f$ conductivity fluctuations in carbon, gold, and chrome films. *Physical Review B*, 25:2955–2958, 1982.

[61] E. W. Carlson, K. A. Dahmen, E. Fradkin, and S. A. Kivelson. Hysteresis and noise from electronic nematicity in high-temperature superconductors. *Physical Review Letters*, 96:097003, 2006.

[62] J.-F. Hamet and B. Mercey. Laser ablation for the growth of materials. *Current Opinion in Solid State and Materials Science*, 3(2):144 – 146, 1998.

[63] J.-H. Kim, S. Lee, and H.-S. Im. The effect of target density and its morphology on TiO2 thin films grown on Si(100) by {PLD}. *Applied Surface Science*, 151(12):6 – 16, 1999.

[64] V. K. Valev, D. Denkova, X. Zheng, A. I. Kuznetsov, C. Reinhardt, B. N. Chichkov, G. Tsutsumanova, E. J. Osley, V. Petkov, B. De Clercq, A. V. Silhanek, Y. Jeyaram, V. Volskiy, P. A. Warburton, G. A. E. Vandenbosch, S. Russev, O. A. Aktsipetrov, M. Ameloot, V. V. Moshchalkov, and T. Verbiest. Plasmon-enhanced sub-wavelength laser ablation: Plasmonic nanojets. *Advanced Materials*, 24(10): OP29–OP35, 2012. ISSN 1521-4095. doi: 10.1002/adma.201103807. URL `http://dx.doi.org/10.1002/adma.201103807`.

[65] Douglas J. Krajnovich, José E. Vázquez, and Richard J. Savoy. Impurity-driven cone formation during laser sputtering of graphite. *Science*, 259(5101):1590–1592, 1993.

[66] S. Larpkiattaworn, C. Chokwatvikul, S. Surinphong, C. Busabok, and P. Termsuksawad. Properties of (Ti, Al)N film prepared by {PVD} cathodic arc. *Suranaree Journal of Science and Technology*, 20(3):221 – 226, 2013.

[67] C.-F. Lo, P. McDonald, D. Draper, and P. Gilman. Influence of tungsten sputtering target density on physical vapor deposition thin film properties. *Journal of Electronic Materials*, 34(12):1468–1473, 2005.

[68] H. V. Fajardo, E. Longo, E. R. Leite, R. Libanori, L. F. D. Probst, and N. L. V. Carreno. Synthesis, characterization and catalytic properties of nanocrystaline Y_2O_3-coated TiO_2 in the ethanol dehydration reaction. *Materials Research*, 15:285 – 290, 2012. ISSN 1516-1439.

[69] Open WetWare. Edta, 2013. URL `http://www.openwetware.org/wiki/EDTA`. Accessed: 2017-02-26.

[70] Wikipedia. Polyvinyl alcohol, 2016. URL `https://en.wikipedia.org/wiki/Polyvinyl_alcohol`. Accessed: 2017-02-26.

[71] M. A. Gülgün, M. H. Nguyen, and W. M. Kriven. Polymerized organic-inorganic synthesis of mixed oxides. *Journal of the American Ceramic Society*, 82(3):556–560, 1999. ISSN 1551-2916.

[72] M. H. Nguyen, S.-J. Lee, and W. M. Kriven. Synthesis of oxide powders by way of a polymeric steric entrapment precursor route. *Journal of Materials Research*, 14(8): 3417–3426, 1999.

[73] M. A. Gülgün, W. M. Kriven, and M. H. Nguyen. Processes for preparing mixed metal oxide powders, November 19 2002. URL `https://www.google.com/patents/US6482387`. US Patent 6,482,387.

[74] A. K. Adak, S. K. Saha, and P. Pramanik. Synthesis and characterization of $MgAl_2O_4$ spinel by PVA evaporation technique. *Journal of Materials Science Letters*, 16(3):234–235, 1997.

[75] Howard M. Smith and A. F. Turner. Vacuum deposited thin films using a ruby laser. *Applied Optics*, 4(1):147–148, 1965.

[76] D. Dijkkamp, T. Venkatesan, X. D. Wu, S. A. Shaheen, N. Jisrawi, Y. H. MinLee, W. L. McLean, and M. Croft. Preparation of YBaCu oxide superconductor thin films using pulsed laser evaporation from high T_c bulk material. *Applied Physics Letters*, 51(8):619–621, 1987.

[77] A. Miotello and R. Kelly. Laser-induced phase explosion: new physical problems when a condensed phase approaches the thermodynamic critical temperature. *Applied Physics A*, 69(1):S67–S73, 1999.

[78] M. S. Hegde. Epitaxial oxide thin films by pulsed laser deposition: Retrospect and prospect. *Journal of Chemical Sciences*, 113(5):445–458, 2001.

[79] Robert Eason. *Pulsed Laser Deposition of Thin Films: Applications-Led Growth of Functional Materials*. John Wiley & Sons, first edition, 2007.

[80] Kai Wang. Laser based fabrication of graphene. In M. Aliofkhazraei, editor, *Advances in Graphene Science*. InTech, 2013. URL `http://www.intechopen.com/books/advances-in-graphene-science/laser-based-fabrication-of-graphene`.

[81] G. J. H. M. Rijnders, G. Koster, D. H. A. Blank, and H. Rogalla. In situ monitoring during pulsed laser deposition of complex oxides using reflection high energy electron diffraction under high oxygen pressure. *Applied Physics Letters*, 70(14):1888–1890, 1997.

[82] B. Dam, J.H. Rector, J. Johansson, DG. DE Groot, and R. Griessen. Non-stoichiometric transfer of complex oxides by pulsed laser deposition at low fluences. *Materials Research Society Proceedings*, 397:175, 1995.

[83] A. Perea, J. Gonzalo, C. Budtz-Jrgensen, G. Epurescu, J. Siegel, C. N. Afonso, and J. Garca-Lpez. Quantification of self-sputtering and implantation during pulsed laser deposition of gold. *Journal of Applied Physics*, 104(8):084912, 2008.

[84] Kai Sturm and Hans-Ulrich Krebs. Quantification of resputtering during pulsed laser deposition. *Journal of Applied Physics*, 90(2):1061–1063, 2001.

[85] M.C. Foote, B.B. Jones, B.D. Hunt, J.B. Barner, R.P. Vasquez, and L.J. Bajuk. Composition variations in pulsed-laser-deposited Y-Ba-Cu-O thin films as a function of deposition parameters. *Physica C: Superconductivity*, 201(1):176 – 182, 1992.

[86] A. R. Moodenbaugh, Youwen Xu, M. Suenaga, T. J. Folkerts, and R. N. Shelton. Superconducting properties of $La_{2-x}Ba_xCuO_4$. *Physical Review B*, 38:4596–4600, 1988.

[87] T. Adachi, T. Noji, and Y. Koike. Crystal growth, transport properties, and crystal structure of the single-crystal $La_{2-x}Ba_xCuO_4(x = 0.11)$. *Physical Review B*, 64: 144524, 2001.

[88] S. A. Hayward, F. D. Morrison, S. A. T. Redfern, E. K. H. Salje, J. F. Scott, K. S. Knight, S. Tarantino, A. M. Glazer, V. Shuvaeva, P. Daniel, M. Zhang, and M. A. Carpenter. Transformation processes in $LaAlO_3$: Neutron diffraction, dielectric, thermal, optical, and raman studies. *Physical Review B*, 72:054110, 2005.

[89] Z. Q. Liu, Z. Huang, W. M. L, K. Gopinadhan, X. Wang, A. Annadi, T. Venkatesan, and Ariando. Atomically flat interface between a single-terminated $LaAlO_3$ substrate and $SrTiO_3$ thin film is insulating. *American Institute of Physics Advances*, 2(1): 012147, 2012.

[90] Department of Pharmacology University of Virgina. Atomic force microscope (AFM), 2017. URL `https://pharm.virginia.edu/facilities/atomic-force-microscope-afm/`. Accessed: 2017-03-02.

[91] Nanoscience Instruments. How an AFM works, 2017. URL `http://www.nanoscience.com/technology/afm-technology/how-afm-works/`. Accessed: 2017-03-02.

[92] La Agencia Estatal Consejo Superior de Investigaciones Cientficas. Deriving an informal interpretation of Bragg's law, 2017. URL `http://www.xtal.iqfr.csic.es/Cristalografia/parte_05_5.html`. Accessed: 2017-03-02.

[93] Paul Barnes, Tony Csoka, and Simon Jacques. What is powder diffraction?, 2006. URL `http://pd.chem.ucl.ac.uk/pdnn/powintro/powdiff.htm`. Accessed: 2017-03-02.

[94] Andrew Richter. X-ray reflectivity, 2017. URL `http://physics.valpo.edu/staff/arichter/XRR.htm`. Accessed: 2017-03-02.

[95] W. Stautner, R. Chen, M. Xu, J. Rochford, and J. Trigger. Occurrence of thermoacoustic phenomena at 0.8 K, 4 K and above. *IOP Conference Series: Materials Science and Engineering*, 101(1):012038, 2015.

[96] Walter Meissner Institute. SQUID magnetometry, 2012. URL `https://www.wmi.badw.de/methods/squid.htm`. Accessed: 2017-03-02.

[97] S. J. Turneaure, E. R. Ulm, and T. R. Lemberger. Numerical modeling of a twocoil apparatus for measuring the magnetic penetration depth in superconducting films and arrays. *Journal of Applied Physics*, 79(8):4221–4227, 1996.

[98] *Voltage Preamplifiers*. Stanford Research Systems, 1 2017. Rev. 2.7.

[99] *Dual-Channel Filters*. Stanford Research Systems, 1 2007. Rev. 2.7.

[100] *Ultra Low Input Bias Current Instrumentation Amplifier*. Burr-Brown Corporation, 5 1995.

[101] *AC and DC Current Source*. Keithley Instruments, Inc., 6 2005. Rev. B.

[102] M. Motta, C. V. Deimling, M. J. Saeki, and P. N. Lisboa-Filho. Chelating agent effects in the synthesis of mesoscopic-size superconducting particles. *Journal of Sol-Gel Science and Technology*, 46(2):201–207, 2008.

[103] V.V. Alexandrov, V.V. Borisovskii, T.A. Fedotova, L.M. Fisher, N.V. Il'in, O.K. Smirnova, I.F. Voloshin, M.A. Baranov, and V.S. Gorbachev. On the Meissner effect in granular superconductors. *Physica C: Superconductivity*, 173(5):458 – 464, 1991.

[104] S. Ono, Seiki Komiya, and Yoichi Ando. Strong charge fluctuations manifested in the high-temperature hall coefficient of high-T_c cuprates. *Physical Review B*, 75: 024515, 2007.

[105] Z. Stegen, Su Jung Han, Jie Wu, A. K. Pramanik, M. Hücker, Genda Gu, Qiang Li, J. H. Park, G. S. Boebinger, and J. M. Tranquada. Evolution of superconducting correlations within magnetic-field-decoupled $La_{2-x}Ba_xCuO_4$ ($x = 0.095$). *Physical Review B*, 87:064509, 2013.

[106] X. Y. Tee, T. Ito, T. Ushiyama, Y. Tomioka, I. Martin, and C. Panagopoulos. Two superconducting transitions in single-crystal $La_{2-x}Ba_xCuO_4$. *Physical Review B*, 95: 054516, 2017.

[107] H. Sato, M. Naito, A. Tsukada, S. Karimoto, and A. Matsuda. Influence of substrates on epitaxial thin films of high-temperature superconductors. *Physica C: Superconductivity*, 362(1):186 – 194, 2001. ISSN 0921-4534.

[108] M.F. De Campos, J. Damasceno, R. Machado, and C. Achete. Uncertainty estimation of lattice parameters measured by x-ray diffraction. 09 2006.

[109] L Sirdeshmukh D.B. Sirdeshmukh and K.G. Subhadra. *Atomistic Properties of Solids*. Springer, Berlin, Heidelberg, first edition, 2011.

[110] H.P. Klug and L.E. Alexander. *X-Ray Diffraction Procedures: For Polycrystalline and Amorphous Materials*. Wiley-Interscience, second edition, 1974.

[111] P. Sippel, S. Krohns, E. Thoms, E. Ruff, S. Riegg, H. Kirchhain, F. Schrettle, A. Reller, P. Lunkenheimer, and A. Loidl. Dielectric signature of charge order in lanthanum nickelates. *The European Physical Journal B*, 85(7):235, 2012.